

DEPARTMENT OF PHYSICS, UNIVERSITY OF JYVÄSKYLÄ

**JET TRANSVERSE MOMENTUM DISTRIBUTIONS
MEASURED BY ALICE**

**BY
TOMAS SNELLMAN**

PHD thesis

Supervisors: Jan Rak, Dong Jo Kim

Jyväskylä, Finland
December, 2018

3 Contents

4	1	Introduction	8
5	1.1	Quantum chromodynamics	9
6	1.1.1	Foundation of QCD	9
7	1.1.2	Asymptotic Freedom	10
8	1.2	heavy-ion physics	14
9	1.2.1	History	14
10	1.3	Features of Heavy-Ion Collisions	16
11	1.3.1	Collision Geometry	16
12	1.3.2	Nuclear Geometry	17
13	1.3.3	Hydrodynamical Modelling	20
14	1.4	Flow	23
15	1.4.1	Anisotropic Flow	24
16	1.5	Hard processes	25
17	1.5.1	pQCD factorization	25
18	1.5.2	Jet hadronisation	28
19	1.5.3	Jet energy loss	32
20	1.5.4	New paradigm of jet Quenching	37
21	1.5.5	Jet shape measurements	39
22	1.6	QGP in Small systems	39
23	1.6.1	Collective phenomena	40
24	1.6.2	Absence of jet quenching	40
25	1.6.3	Centrality determination in small systems	41
26	2	Experimental Details	50
27	2.1	CERN	50
28	2.2	Large Hadron Collider	50
29	2.2.1	LHC experiments	52
30	2.3	ALICE	53
31	2.3.1	Tracking	54
32	2.3.2	TPC	55
33	2.3.3	TPC upgrade	56
34	2.3.4	Particle identification	58
35	2.3.5	Electromagnetic Calorimeter	59
36	2.3.6	Forward detectors	60
37	2.3.7	Muon spectrometer	63

38	2.3.8 Trigger	63
39	3 Event and track selection	65
40	3.1 Event selection	65
41	3.2 Track selection	65
42	3.3 Cluster selection	67
43	4 Analysis method	68
44	4.1 Jet Finding	68
45	4.1.1 Anti k_T algorithm	69
46	4.2 Definition of j_T	70
47	4.3 Unfolding detector effects	71
48	4.3.1 Bayesian unfolding	73
49	4.3.2 Toy Monte Carlo	75
50	4.3.3 Pythia Response matrices	75
51	4.3.4 Unfolding algorithm	77
52	4.3.5 Unfolding closure test	77
53	4.4 Background	80
54	4.4.1 Perpendicular cone background	80
55	4.4.2 Random background	80
56	4.4.3 Auto-correlations	82
57	4.4.4 Background methods	82
58	4.5 Fitting	82
59	5 Systematic errors	85
60	5.1 Background	85
61	5.2 Unfolding	85
62	5.2.1 Effect of number of iterations	86
63	5.2.2 Effect of different prior	88
64	5.2.3 Effect of p_T truncation	88
65	5.3 Tracking	89
66	5.4 EMCal clusters	90
67	5.5 Summary/Combining systematics	90
68	5.6 Additional checks	91
69	5.6.1 Comparison between A and C side	91
70	6 Results	93
71	6.1 Fitting	93
72	6.1.1 RMS values from fitted distributions	93
73	6.2 High multiplicity	93

⁷⁴	7	Discussion	96
⁷⁵	7.1	Dihadron j_T	96
⁷⁶	7.2	Comparing dihadron and jet j_T results	97
⁷⁷	7.2.1	Different R parameters	98
⁷⁸	7.2.2	Leading tracks versus jet	99
⁷⁹	8	Summary	101
⁸⁰	Appendices		102
⁸¹	A	Additional graphs	102

⁸² List of Figures

⁸³	1	QCD phase diagram	12
⁸⁴	2	η/s vs $(T - T_c)/T_c$	13
⁸⁵	3	The definitions of the Reaction Plane and Participant Plane coordinate systems	16
⁸⁶	4	Interaction between partons in central and peripheral collisions. . .	17
⁸⁷	5	An illustration of the multiplicity distribution in ALICE measurement with centrality classes.	18
⁸⁸	6	The results of one Glauber Monte Carlo simulation.	21
⁸⁹	7	Schematic representation of a heavy-ion collision	22
⁹⁰	8	Charged particle spectra	23
⁹¹	9	Illustration of flow in momentum space in central and peripheral collisions.	24
⁹²	10	QCD Leading Order	26
⁹³	11	Hard scattering	27
⁹⁴	12	Jet showering	28
⁹⁵	15	Measurements of the nuclear modification factor R_{AA} in central heavy-ion collisions	33
⁹⁶	16	A comparison between observed $R_{AA}(\Delta\phi, p_T)$ and R_{AA} using v_2 . .	34
⁹⁷	17	Elliptic flow, v_2 from $p_T = 1$ to 60 GeV/c	44
⁹⁸	18	Photon spectrum	45
⁹⁹	20	Calculations of the intial energy density in small collision systems at RHIC and the resulting hydrodynamic evolution.	47
¹⁰⁰	21	Two-particle correlation results in PbPb, pPb, and pp collisions at the LHC [].	47
¹⁰¹	22	RpA in proton-lead collisions	47

108	23	Distribution of the sum of amplitudes in the V0A hodoscopes (Pb-going), as well as the NBD-Glauber fit (explained in the text). Centrality classes are indicated by vertical lines. The inset shows a zoom-in on the most peripheral events. [1]	48
112	24	Top: Scatter plot of number of participating nucleons versus impact parameter; Bottom: Scatter plot of multiplicity versus the number of participating nucleons from the Glauber fit for V0A. The quantities are calculated with a Glauber Monte Carlo of p-Pb (left) and Pb-Pb (right) collisions. [1]	49
117	25	CERN collider complex	51
118	26	ALICE	53
119	27	ITS	54
120	28	TPC	56
121	29	The EMCal detector arc, where the segmentation into 10 full size and 2 1/3-sized (5 and 1 per side) supermodules can be seen.	61
122	30	The exploded EMCal tower view	62
123	31	A simple example of the antil- k_T algorithm in progress. The red tracks in the leftmost figure are identified to have the smallest $k_{T,i}$ in the event and are combined into the red track of the middle figure. As this continues the remaining tracks are added to this or other jets. One tracks was deemed to be isolated enough to be counted as a protojet by itself. Note that the rightmost figure is zoomed out.	70
124	32	Illustration of \vec{j}_T . The jet fragmentation transverse momentum, \vec{j}_T , is defined as the transverse momentum component of the track momentum, \vec{p}_{track} , with respect to the jet momentum, \vec{p}_{jet}	71
125	33	Inclusive j_T with background	72
126	34	Results from unfolding in Toy Monte Carlo	76
127	35	Jet p_T in unfolding closure test	78
128	36	j_T Response matrices in individual $p_{T,\text{jet}}$ bins	78
129	37	Pythia closure test results. Fake tracks include also tracks that do exist in the true dataset, but for one reason or another were not given j_T values. j_T is only calculated for tracks that are associated with jets	79
130	38	Background estimation	81
131	39	Flowchart representation of the perpendicular cone background procedure	81
132	40	j_T background with two different methods	83
133	41	Comparison of the effect of background method on j_T signal.	86
134	42	j_T signal with random bacgkround subtraction fits in different jet p_T bins	86

148	43	Differences between perpendicular cone and random background subtraction in the resulting RMS values.	87
149			
150	44	Resulting signal distributions from SVD unfolding with the perpendicular cone background methods. These are compared to the results from the Bayesian algorithm to estimate the systematic uncertainty.	87
151			
152			
153			
154	45	Differences between Bayesian and SVD unfolding in the resulting RMS values	87
155			
156	46	Unfolding with different number of iterations	88
157			
158	47	Effect of changing prior from true distribution in PYTHIA to the unfolded distribution. <i>Missing figure</i>	88
159			
160	48	Effect of changing minimum jet p_T used in unfolding from 5 to 10 GeV	89
161			
162	49	Relative systematic errors resulting from tracking efficiency uncertainty.	89
163			
164	50	Results from PYTHIA simulations with Cluster energies scaled up and down by 2 %. Additionally jet momenta were scaled by 2 % when determining the jet p_T bin.	90
165			
166	51	Relative systematic errors resulting from cluster energy uncertainty.	91
167			
168	52	Comparison of inclusive j_T distributions between A and C side for minimum bias and EMCAL triggered data.	92
169			
170	53	j_T signal fits in different jet p_T bins	93
171			
172	54	RMS values extracted from the fits for the gaussian (narrow) and inverse gamma (wide) components	94
173			
174	55	RMS values extracted from the fits for the gaussian (narrow) and inverse gamma (wide) components	94
175			
176	56	j_T distributions for high multiplicity p-Pb events. <i>Replace figure</i>	95
177			
178	57	Dihadron j_T results	96
179			
180	58	RMS values of the narrow and wide j_T components in the dihadron correlation analysis. Results from pp collisions at $\sqrt{s} = 7$ TeV (circular symbols) and from p-Pb collisions at $\sqrt{s_{NN}} = 5.02$ TeV (square symbols) are compared to PYTHIA 8 tune 4C simulations at $\sqrt{s} = 7$ TeV (short dashed line) and at $\sqrt{s} = 5.02$ TeV (long dashed line). Different panels correspond to different x_{\parallel} bins with $0.2 < x_{\parallel} < 0.4$ on the left, $0.4 < x_{\parallel} < 0.6$ in the middle, and $0.6 < x_{\parallel} < 1.0$ on the right. The statistical errors are represented by bars and the systematic errors by boxes. [2]	97
181			
182			
183			
184			

185	59	Jet j_T results are compared to results obtained in the dihadron	
186		analysis. Dihadron trigger p_T bins are converted to jet p_T bins	
187		using observed mean $p_{T\text{jet}}$ values in $p_{T\text{trigger}}$ bins. Dihadron results	
188		are for $0.2 < x_{ } < 0.4$	98
189	60	Pythia R parameters j_T	99
190	61	Pythia R parameters RMS	100
191	62	Results of calculating j_T with respect to the jet axis or the leading	
192		hadron. The assumption is that because the leading hadron is an	
193		imperfect estimate of the jet axis, low j_T tracks should on average	
194		be shifted to higher j_T	100

195 1 Introduction

196 REWRITE At sufficiently high energies quarks and gluons are no longer bound to
197 hadrons, but they form a deconfined state known as Quark-Gluon plasma (QGP).
198 The main goal of heavy-ion physics is the study of QGP and its properties. One
199 of the experimental observables that is sensitive to the properties of QGP is the
200 azimuthal distribution of particles in the plane perpendicular to the beam direc-
201 tion.

202 When nuclei collide at non-zero impact parameter (non-central collisions), their
203 overlap region is asymmetric. This initial spatial asymmetry is converted via multi-
204 ple collisions into an anisotropic momentum distribution of the produced particles.
205 For low momentum particles ($p_T \lesssim 3$ GeV/c), this anisotropy is understood to
206 result from hydrodynamically driven flow of the QGP [3–7].

207 One way to characterize this anisotropy is with coefficients from a Fourier se-
208 ries parametrization of the azimuthal angle distribution of emitted hadrons. The
209 second order coefficient, v_2 which is also known as elliptic flow, shows clear depen-
210 dence on centrality. The collision geometry is mainly responsible for the elliptic
211 flow. Higher harmonics don't depend that much on centrality. These higher har-
212 monics carry information about the fluctuations in collisions. The event-by-event
213 fluctuations have an increasing importance in measurements and it has been ob-
214 served that measurements of elliptic flow in central collisions and measurements
215 of higher order harmonics are consistent with the assumption that flow in these
216 cases is mainly due to fluctuations [8].

217 At LHC energies $\sqrt{s_{NN}} = 2.76\text{GeV}$ it has been observed that in general there
218 is little difference to flow at RHIC energies. The v_2 coefficient is about 20% greater
219 at LHC than at RHIC, depending on the centrality bin. The particle identified
220 v_2 for kaons and pions follows the same trend. However it was observed that for
221 proton v_2 the quark number scaling does not work [9]. So far there is no agreement
222 of why this scaling breaks down at LHC or why it works so well at RHIC energies.

223

224 **1.1 Quantum chromodynamics**

225 **1.1.1 Foundation of QCD**

226 There are four known basic interactions in the universe: gravity, electromagnetic,
227 weak and strong interactions. The standard model of particle physics includes
228 three of these, excluding the gravitational interaction. The theory of strong inter-
229 actions is known as Quantum Chromodynamics (QCD).

230 The development of QCD began after the introduction of new powerful particle
231 accelerators that were capable of particle physics research in the 1950s. Before this
232 particles were mainly discovered from cosmic rays. Positrons, neutrons and muons
233 were discovered in the 1930s and charged pions were discovered in 1947 [9]. The
234 neutral pion was discovered in 1950 [10].

235 The Lawrence Berkeley National Laboratory started the Bevalac accelerator in
236 1954, Super Proton Synchrotron (SPS) in CERN began operating in 1959 and the
237 Alternating Gradient Synchrotron (AGS) at Brookhaven started in 1960. With
238 an energy of 33 GeV AGS was the most powerful accelerator of that time. By
239 the beginning of 1960s several new particles had been discovered. These included
240 antiprotons, antineutrons, Δ -particles and the six hyperons (Ξ^0 , Ξ^- , Σ^\pm , Σ^0 and
241 Λ).

242 Facing this avalanche of new particles, physicists started the search for symme-
243 tries within them. Already in 1932 Heisenberg [11] had proposed an isospin model
244 to explain similarities between the proton and the neutron. In 1962 Gell-Mann
245 and Ne'eman presented that particles sharing the same quantum numbers (spin,
246 parity) could be organised using the symmetry of SU(3). [12] Heisenberg's Isospin
247 model followed the symmetry of SU(2). Using the SU(3) model known baryons
248 and mesons could be presented as octets. This also lead to the discovery of the
249 Ω^- particle since this was missing from the SU(3) decouplet that included heavier
250 baryons.

251 The most simple representation of SU(3) was a triplet. Inside this triplet parti-
252 cles would have electric charges $2/3$ or $-1/3$. However, these had not been detected.
253 In 1964 Gell-Mann [13] and Zweig proposed that baryons and mesons would be
254 bound states of these three hypothetical triplet particles that Gell-Mann called
255 quarks. Now we know that these are the u , d and s quarks. This original quark
256 model without colour was violating the Pauli exclusion principle. For example
257 the Ω^- particle is comprised of three s quarks which would have exactly the same
258 quantum states.

259 The first one to present the idea of colour was Greenberg already in 1964 [14].
260 In 1971 Gell-Mann and Fritsch presented their model, which solved the antisym-
261 metry problem. They added a colour quantum number to quarks, which separated
262 quarks of the same species. In the new colour model the baryonic wave function

263 became

$$(qqq) \rightarrow (q_r q_g q_b - q_g q_r q_b + q_b q_r q_g - q_r q_b q_g + q_g q_b q_r - q_b q_g q_r), \quad (1)$$

264 The colour model was also supported by experimental evidence. The decay
265 rate of a neutral pion with the addition of colours is

$$\Lambda(\pi^0 \rightarrow \gamma\gamma) = \frac{\alpha^2}{2\pi} \frac{N_c^2}{3^2} \frac{m_\pi^3}{f_\pi^2}. \quad (2)$$

266 For $N_c = 3$ this gives 7.75 eV and the measured value is (7.86 ± 0.54) eV [15].

267 Another observable that combines the colour information also to the number
268 of quark flavours is the Drell-Ratio R [16]

$$R = \frac{\sigma(e^+ + e^- \rightarrow \text{hadrons})}{\sigma(e^+ + e^- \rightarrow \mu^+ + \mu^-)} = N_c \sum_f Q_f^2. \quad (3)$$

269 This ratio has the numerical value 2 when including the three light quarks u , d
270 and s . When the collision energy reaches the threshold of heavy quark (c and
271 b) production processes this increases to $^{10}/_3$ (for $f = u, d, s, c$) and $^{11}/_3$ (for $f =$
272 u, d, s, c, b). The energy threshold ($\sqrt{s} \approx 350$ GeV) of $t\bar{t}$ production, has not been
273 reached so far by any e^+e^- colliders.

274 The colour model explained why no free quarks had been observed as only
275 colour neutral states are possible. The simplest ways of producing a colour neu-
276 tral object are the combination of three quarks, and the combination of a quark-
277 antiquark pair. These are known as baryons and mesons.

278 After the addition of colour the main ingredients of QCD had been estab-
279 lished. The final quantum field theory of Quantum Chromodynamics formed
280 quickly between 1972 and 1974. Main part of this was the work by Gross, Wilczek,
281 Politzer and George for non-abelian gauge field theories [17–21]. Gross, Wilczek
282 and Politzer received the Nobel Prize in Physics for their work. The role of gluons
283 as a colour octet was presented by Fritzsch, Gell-Mann and Leutwyler in 1973 [22].
284 The theory had now 8 massless gluons to mediate the strong interaction.

285 However, these gluons had not been discovered. Indirect evidence of the ex-
286 istence had been seen as it was observed that only about half of the momentum
287 of protons was transported by the quarks [23]. Direct evidence should be seen in
288 electron-electron collisions as a third, gluonic, jet in addition to two quark jets.
289 Three jet events were first seen in 1979 at the PETRA accelerator at DESY [24–26].

290 1.1.2 Asymptotic Freedom

291 In Quantum Electrodynamics (QED) the electric charge is screened. In the vicinity
292 of a charge, the vacuum becomes polarized. Virtual charged particle-antiparticle

293 pairs around the charge are arranged so that opposing charges face each other.
294 Since the pairs also include an equal amount opposite charge compared to the
295 original charge the average charge seen by an observer at a distance is smaller.
296 When the distance to the charge increases the effective charge decreases until the
297 coupling constant of QED reaches the fine-structure constant $\alpha = \frac{1}{137}$.

298 Contrary to QED, QCD is a non-abelian theory. In other words the generators
299 of the symmetry group of QCD, SU(3), do not commute. This has the practical
300 consequence that gluons interact also with other gluons, whereas in QED the
301 neutral carrier particles, photons, only interact with charged particles. There
302 is screening also in QCD because of the colour charges, but in addition to that
303 there is antiscreening because of the gluon interactions. In QCD the antiscreening
304 effect dominates over screening. Thus for larger distances to the colour charge
305 the coupling constant is larger. This explains why no free colour charges can be
306 observed. When the distance between charges increases the interaction strengthens
307 until it is strong enough to produce a new quark-antiquark pair.

308 On the other hand, at very small distances the coupling constant approaches
309 0. This is called asymptotic freedom. For large energies and small distances
310 the coupling constant is negligible. In 1975 Collins [27] predicted a state where
311 individual quarks and gluons are no longer confined into bound hadronic states.
312 Instead they form a bulk QCD matter that Edward Shuryak called Quark-Gluon
313 plasma in his 1980 review of QCD and the theory of superdense matter [28]. QGP
314 can be seen as a separate state of matter. A schematic view of a phase diagram
315 for QCD matter is shown in Fig. 1.

316 In the early universe at the age of 10^{-6} s after the Big Bang the conditions
317 preferred the existence of QGP instead of hadronic matter. Nowadays bulk QCD
318 matter, its properties and its phase transitions between hadronic matter and the
319 quark-gluon plasma (QGP) can be explored in the laboratory, through collisions
320 of heavy atomic nuclei at ultra-relativistic energies. The study of QCD matter at
321 high temperature is of fundamental and broad interest. The phase transition in
322 QCD is the only phase transition in a quantum field theory that can be probed by
323 any present or foreseeable technology.

324 One important property of the QGP is the shear viscosity to entropy ratio,
325 η/s . It is believed that this ratio has an universal minimum value of $1/4\pi \approx 0.08$,
326 among all substances in nature. This limit would be reached in the strong coupling
327 limit of certain gauge theories [30]. The temperature dependance of the ratio is
328 shown in Fig. 2. The minimum value of η/s is found in the vicinity of the critical
329 temperature, T_c [31]. Finding the η/s values in QGP matter would therefore also
330 provide a way of determining the critical point of QCD matter.

331 The η/s value for the matter created in Au-Au collisions at RHIC ($\sqrt{s_{NN}}$) has
332 been estimated to be 0.09 ± 0.015 [31], which is very close to the lowest value for a

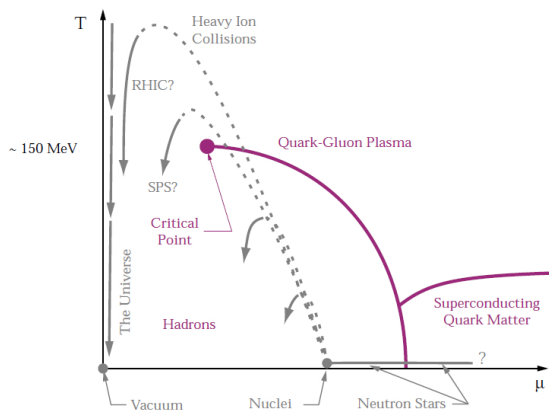


Figure 1: A schematic outline for the phase diagram of QCD matter at ultra-high density and temperature. The quark chemical potential μ that is on the x-axis represents the imbalance between quarks and antiquarks. At zero temperature this corresponds to the number of quarks but at higher temperatures there are also additional pairs of quarks and antiquarks. Along the horizontal axis the temperature is zero, and the density is zero up to the onset transition where it jumps to nuclear density, and then rises with increasing μ . Neutron stars are in this region of the phase diagram, although it is not known whether their cores are dense enough to reach the quark matter phase. Along the vertical axis the temperature rises, taking us through the crossover from a hadronic gas to the quark-gluon plasma. This is the regime explored by high-energy heavy-ion colliders. [29]

333 wide class of thermal quantum field theories [30] for all relativistic quantum field
 334 theories at finite temperature and zero chemical potential. This suggests that the
 335 the matter created goes through a phase where it is close to the critical point of
 336 QCD.

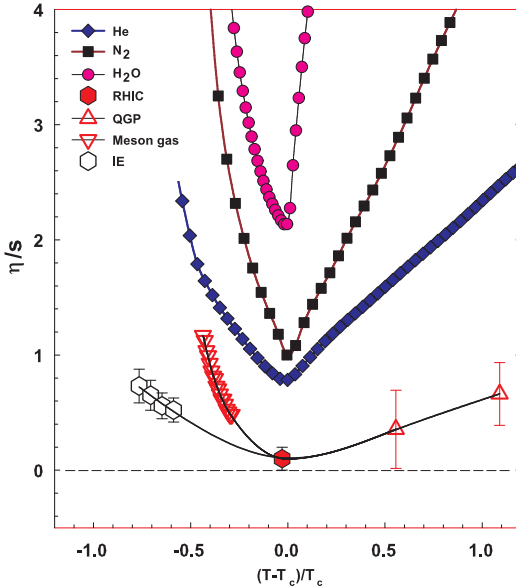


Figure 2: η/s as a function of $(T - T_c)/T_c$ for several substances as indicated. The calculated values for the meson-gas have an associated error of $\sim 50\%$. The lattice QCD value $T_c = 170$ MeV is assumed for nuclear matter. The lines are drawn to guide the eye. [31]

337 1.2 heavy-ion physics

338 The Quark Gluon Plasma (QGP) is experimentally accessible by colliding heavy-
339 ions at high energies. Nowadays research of Heavy-Ion Collisions is mainly per-
340 formed at two particle colliders; The Relativistic heavy-ion Collider (RHIC) at
341 BNL in New York, USA and the Large Hadron Collider (LHC) at CERN in Switzer-
342 land. Energy densities at these colliders should be enough to produce QGP and
343 convincing evidence of the creation has been seen at both colliders.

344 The development of heavy-ion physics is strongly connected to the development
345 of particle colliders. Experimental study of relativistic heavy-ion collisions has been
346 carried out for three decades, beginning with the Bevalac at Lawrence Berkeley
347 National Laboratory (LBNL) [32], and continuing with the AGS at Brookhaven
348 National Laboratory (BNL) [33], CERN SPS [34], RHIC at BNL and LHC at
349 CERN.

350 1.2.1 History

351 The first heavy-ion collisions were performed at the Bevalac experiment at the
352 Lawrence Berkeley National Laboratory [32] and at the Joint Institute for Nu-
353 clear Research in Dubna [35] at energies up to 1GeV per nucleon. In 1986 the
354 Super Proton Synchrotron (SPS) at CERN started to look for QGP signatures in
355 O+Pb collisions. The center-of-mass energy per colliding nucleon pair ($\sqrt{s_{NN}}$)
356 was 19.4 GeV [34]. These experiments did not find any decisive evidence of the
357 existence of QGP. In 1994 a heavier lead (Pb) beam was introduced for new exper-
358 iments at $\sqrt{s_{NN}} \approx 17$ GeV. At the same time the Alternating Gradient Synchrotron
359 (AGS) at BNL, Brookhaven collided ions up to ^{32}S with a fixed target at energies
360 up to 28 GeV [33]. Although the discovery of a new state of matter was reported
361 at CERN, these experiments provided no conclusive evidence of QGP. Now SPS
362 is used with 400 GeV proton beams for fixed-target experiments, such as the SPS
363 heavy-ion and Neutrino Experiment (SHINE) [36], which tries to search for the
364 critical point of strongly interacting matter.

365 The Relativistic heavy-ion Collider (RHIC) at BNL in New York, USA started
366 its operation in 2000. The top center-of-mass energy per nucleon pair at RHIC, 200
367 GeV, was reached in the following years. The results from the experiments at RHIC
368 have provided a lot of convincing evidences that QGP was created [3,4,37,38]. The
369 newest addition to the group of accelerators capable of heavy-ion physics is the
370 Large Hadron Collider (LHC) at CERN, Switzerland. LHC started operating in
371 November 2009 with proton-proton collisions. First Pb-Pb heavy-ion runs started
372 in November 2010 with $\sqrt{s_{NN}} = 2.76$ TeV, over ten times higher than at RHIC.
373 Among the six experiments at LHC, the Large Ion Collider Experiment (ALICE)
374 is dedicated to heavy-ion physics. Also CMS and ATLAS have active heavy-ion

³⁷⁵ programs.

³⁷⁶ add a table of LHC runs related ALICE

³⁷⁷ **1.3 Features of Heavy-Ion Collisions**

³⁷⁸ **1.3.1 Collision Geometry**

³⁷⁹ In contrast to protons atomic nuclei are objects with considerable transverse size.
³⁸⁰ The properties of a heavy-ion collision depend strongly on the impact parameter
³⁸¹ b which is the vector connecting the centers of the two colliding nuclei at their
³⁸² closest approach. One illustration of a heavy-ion collision is shown in Fig. 3.

³⁸³ Impact parameter defines the reaction plane which is the plane spanned by b
³⁸⁴ and the beam direction. Ψ_{RP} gives the angle between the reaction plane and some
³⁸⁵ reference frame angle. Experimentally the reference frame is fixed by the detector
³⁸⁶ setup. Reaction plane angle cannot be directly measured in high energy nuclear
 collisions, but it can be estimated with the event plane method [39].

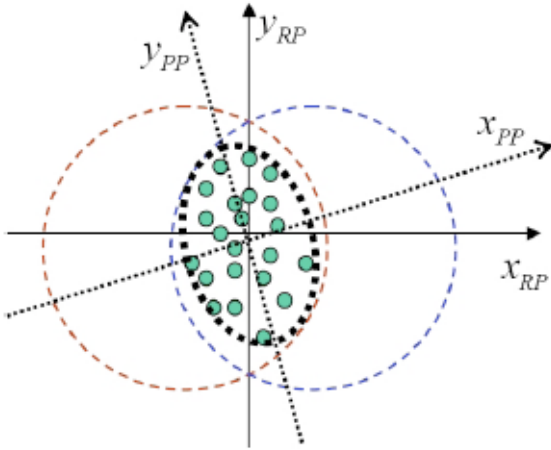


Figure 3: The definitions of the Reaction Plane and Participant Plane coordinate systems [40]. The dashed circles represent the two colliding nuclei and the green dots are partons that take part in the collision. x_{PP} and x_{RP} are the participant and reaction planes. The angle between x_{RP} and x_{PP} is given by Eq. (4). y_{PP} and y_{RP} are lines perpendicular to the participant and reaction planes.

³⁸⁷
³⁸⁸ Participant zone is the area containing the participants. The distribution of
³⁸⁹ nucleons in the nucleus exhibits time-dependent fluctuations. Because the nucleon
³⁹⁰ distribution at the time of the collision defines the participant zone, the axis of
³⁹¹ the participant zone fluctuates and can deviate from the reaction plane. The angle
³⁹² between the participant plane and the reaction plane is defined by [41]

$$\psi_{PP} = \arctan \frac{-2\sigma_{xy}}{\sigma_y^2 - \sigma_x^2 + \sqrt{(\sigma_y^2 - \sigma_x^2)^2 + 4\sigma_{xy}^2}}, \quad (4)$$

393 where the σ -terms are averaged over the energy density.

$$\sigma_y^2 = \langle y^2 \rangle - \langle y \rangle^2, \sigma_x^2 = \langle x^2 \rangle - \langle x \rangle^2, \sigma_{xy} = \langle xy \rangle - \langle x \rangle \langle y \rangle \quad (5)$$

394 The impact parameter is one way to quantize the centrality of a heavy-ion
 395 collision but it is impossible to measure in a collision. It can be estimated from
 396 observed data using theoretical models, but this is always model-dependent and
 397 to compare results from different experiments one needs an universal definition for
 398 centrality. The difference between central and peripheral collisions is illustrated
 399 in Fig. 4. In a central collision the overlap region is larger than in a peripheral
 400 collision. Larger overlap region translates into a larger number of nucleons partici-
 401 pating in the collision, which in turn leads to a larger number of particles produced
 402 in the event.

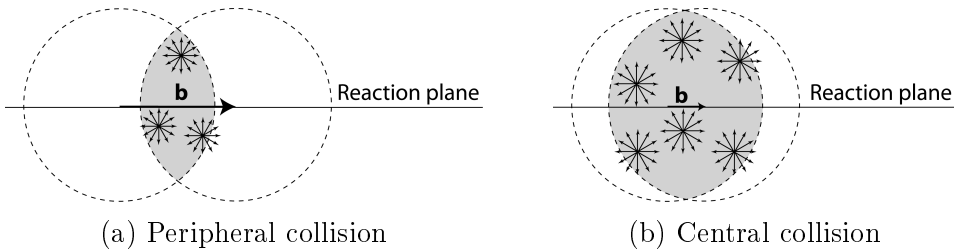


Figure 4: Interaction between partons in central and peripheral collisions. The snowflakes represent elementary parton-parton collisions. When the impact parameter b is large the number of elementary collisions is small. Particle production is small. Smaller impact parameter increases the number of elementary collisions. This increases particle production.

403 Usually centrality is defined by dividing collision events into percentile bins by
 404 the number participants or experimentally by the observed multiplicity. Centrality
 405 bin 0-5% corresponds to the most central collisions with the highest multiplicity
 406 and higher centrality percentages correspond to more peripheral collisions with
 407 lower multiplicities. A multiplicity distribution from ALICE measurements [42]
 408 illustrating the centrality division is shown in Fig. 5. The distribution is fitted
 409 using a phenomenological approach based on a Glauber Monte Carlo [43] plus a
 410 convolution of a model for the particle production and a negative binomial distri-
 411 bution.

412 1.3.2 Nuclear Geometry

413 To model heavy-ion collisions one must first have a description as good as possible
 414 of the colliding objects. Atomic nuclei are complex ensembles of nucleons. The
 415 nuclei used in heavy-ion physics have in the order of 200 nucleons. Mostly used

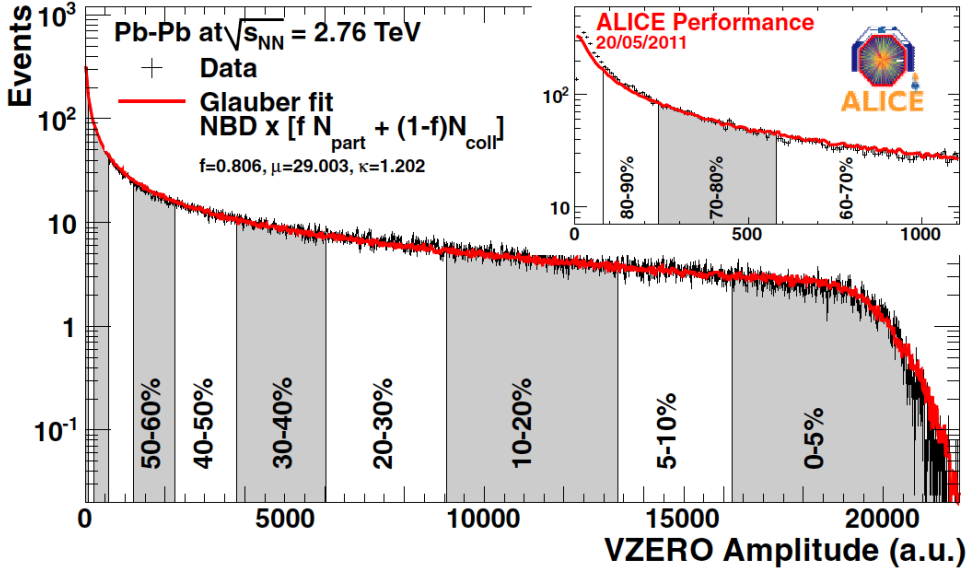


Figure 5: An illustration of the multiplicity distribution in ALICE measurements. The red line shows the fit of the Glauber calculation to the measurement. The data is divided into centrality bins [42]. The size of the bins corresponds to the indicated percentile.

⁴¹⁶ nuclei are ²⁰⁸Pb at LHC and ¹⁹⁷Au at RHIC. The distribution of these nucleons
⁴¹⁷ within a nucleus is not uniform and is subject to fluctuations in time.

⁴¹⁸ Nuclear geometry in heavy-ion collisions is often modelled with the Glauber
⁴¹⁹ Model. The model was originally developed to address the problem of high energy
⁴²⁰ scattering with composite particles. Glauber presented his first collection of papers
⁴²¹ and unpublished work in his 1958 lectures [44]. In the 1970's Glauber's work
⁴²² started to have utility in describing total cross sections. Maximon and Czyz applied
⁴²³ it to proton-nucleus and nucleus-nucleus collisions in 1969 [45].

⁴²⁴ In 1976 [46] Białas, Bleszyński, and Czyz applied Glauber's approach to
⁴²⁵ inelastic nuclear collisions. Their approach introduced the basic functions used in
⁴²⁶ modern language including the thickness function and the nuclear overlap function.
⁴²⁷ Thickness function is the integral of the nuclear density over a line going through
⁴²⁸ the nucleus with minimum distance s from its center

$$T_A(s) = \int_{-\infty}^{\infty} dz \rho(\sqrt{s^2 + z^2}). \quad (6)$$

⁴²⁹ This function gives the thickness of the nucleus, i.e. the amount material seen by
⁴³⁰ a particle passing through it.

⁴³¹ Overlap function is an integral of the thickness functions of two colliding nuclei
⁴³² over the overlap area. This can be seen as the material that takes part in the
⁴³³ collision. It is given as a function of the impact parameter b

$$T_{AB}(b) = \int ds^2 T_A(\bar{s}) T_B(\bar{s} - \bar{b}) \quad (7)$$

⁴³⁴ The average overlap function, $\langle T_{AA} \rangle$, in an A-A collisions is given by [47]

$$\langle T_{AA} \rangle = \frac{\int T_{AA}(b) db}{\int (1 - e^{-\sigma_{pp}^{inel} T_{AA}(b)}) db}. \quad (8)$$

⁴³⁵ Using $\langle T_{AA} \rangle$ one can calculate the mean number of binary collisions

$$\langle N_{coll} \rangle = \sigma_{pp}^{inel} \langle T_{AA} \rangle, \quad (9)$$

⁴³⁶ where the total inelastic cross-section, σ_{pp}^{inel} , gives the probability of two nucleons
⁴³⁷ interacting. The number of binary collisions is related to the hard processes in a
⁴³⁸ heavy-ion collision. Each binary collision has equal probability for direct produc-
⁴³⁹ tion of high-momentum partons. Thus the number of high momentum particles is
⁴⁴⁰ proportional to $\langle N_{coll} \rangle$.

⁴⁴¹ Soft production on the other hand is related to the number of participants.
⁴⁴² It is assumed that in the binary interactions participants get excited and further
⁴⁴³ interactions are not affected by previous interactions because the time scales are
⁴⁴⁴ too short for any reaction to happen in the nucleons. After the interactions ex-
⁴⁴⁵ cited nucleons are transformed into soft particle production. Production does not
⁴⁴⁶ depend on the number of interactions a nucleon has gone through. The average
⁴⁴⁷ number of participants, $\langle N_{part} \rangle$ can also be calculated from the Glauber model

$$\begin{aligned} \langle N_{part}^{AB}(b) \rangle &= \int ds^2 T_A(\bar{s}) \left[1 - \left[1 - \sigma_{NN} \frac{T_B(\bar{s} - \bar{b})}{B} \right]^B \right] \\ &+ \int ds^2 T_B(\bar{s}) \left[1 - \left[1 - \sigma_{NN} \frac{T_A(\bar{s} - \bar{b})}{A} \right]^A \right]. \end{aligned} \quad (10)$$

⁴⁴⁸ Glauber calculations require some knowledge of the properties of the nuclei.
⁴⁴⁹ One requirement is the nucleon density distribution, which can be experimen-
⁴⁵⁰ tally determined by studying the nuclear charge distribution in low-energy elec-
⁴⁵¹ tron scattering experiments [43]. The nucleon density is usually parametrized by
⁴⁵² a Woods-Saxon distribution

$$\rho(r) = \frac{\rho_0}{1 + \exp\left(\frac{r-R}{a}\right)}, \quad (11)$$

where ρ_0 is the nucleon density in center of the nucleus, R is the nuclear radius and a parametrizes the depth of the skin. The density stays relatively constant as a function of r until around R where it drops to almost 0 within a distance given by a .

Another observable required in the calculations is the total inelastic nucleon-nucleon cross-section $\sigma_{\text{inel}}^{\text{NN}}$. This can be measured in proton-proton collisions at different energies.

There are two often used approaches to Glauber calculations. The optical approximation is one way to get simple analytical expressions for the nucleus-nucleus interaction cross-section, the number of interacting nucleons and the number of nucleon-nucleon collisions. In the optical Glauber it is assumed that during the crossing of the nuclei the nucleons move independently and they will be essentially undeflected.

With the increase of computational power at hand the Glauber Monte Carlo (GMC) approach has emerged as a method to get a more realistic description of the collisions. In GMC the nucleons are distributed randomly in three-dimensional coordinate system according to the nuclear density distributions. Also nuclear parameters, like the radius R can be sampled from a distribution. A heavy-ion collision is then treated as a series of independent nucleon-nucleon collisions, where in the simplest model nucleons interact if their distance in the plane orthogonal to the beam axis, d , satisfies

$$d < \sqrt{\sigma_{\text{inel}}^{\text{NN}}} \quad (12)$$

The average number of participants and binary collisions can then be determined by simulating many nucleus-nucleus collisions. The results of one GMC Pb-Pb event with impact parameter $b = 9.8 \text{ fm}$ is shown in Fig. 6

1.3.3 Hydrodynamical Modelling

The relativistic version of hydrodynamics has been used to model the deconfined phase of a heavy-ion collision with success. Heavy-ion collisions produce many hadrons going into all directions. It is expected that tools from statistical physics would be applicable to this complexity [48]. The power of relativistic hydrodynamics lies in its simplicity and generality. Hydrodynamics only requires that there is local thermal equilibrium in the system. In order to reach thermal equilibrium the system must be strongly coupled so that the mean free path is shorter than the length scales of interest [49].

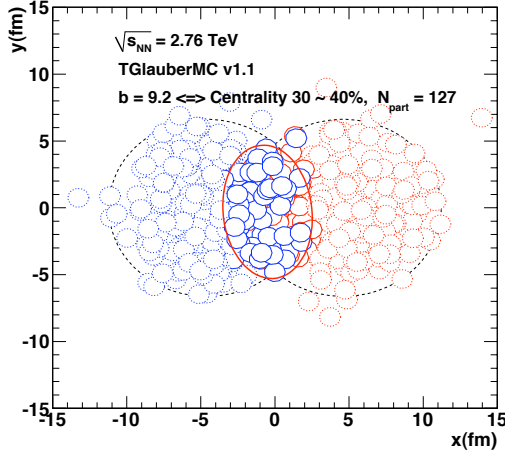


Figure 6: The results of one Glauber Monte Carlo simulation. Big circles with black dotted boundaries represent the two colliding nuclei. The participant zone is highlighted with the solid red line. Small red and blue circles represent nucleons. Circles with thick boundaries are participants i.e. they interact with at least one nucleon from the other nucleus. Small circles with dotted boundaries are spectators which do not take part in the collision.

486 The use of relativistic hydrodynamics in high-energy physics dates back to
 487 Landau [50] and the 1950's, before QCD was discovered. Back then it was used
 488 in proton-proton collisions. Development of hydrodynamics for the use of heavy-
 489 ion physics has been active since the 1980's, including Bjorken's study of boost-
 490 invariant longitudinal expansion and infinite transverse flow [51]. Major steps
 491 were taken later with the inclusion of finite size and and dynamically generated
 492 transverse size [52, 53], a part of which was done at the University of Jyväskylä.
 493 The role of hydrodynamics in heavy-ion physics was strengthened when QGP was
 494 observed to behave like a liquid by RHIC [3].

495 The evolution of a heavy-ion event can be divided into four stages. A schematic
 496 representation of the evolution of the collisions is shown in Fig. 7. Stage 1 follows
 497 immediately the collision. This is known as the pre-equilibrium stage. Hydrody-
 498 namic description is not applicable to this regime because thermal equilibrium is
 499 not yet reached. The length of this stage is not known but it is assumed to last
 500 about $1 \text{ fm}/c$ in proper time τ .

501 The second stage is the regime where thermal equilibrium or at least near-
 502 equilibrium is reached. In this stage hydrodynamics should be applicable if the
 503 temperature is above the deconfinement temperature [49]. This lasts about $5 - 10 \text{ fm}/c$ until the temperature of the system sinks low enough for hadronization to

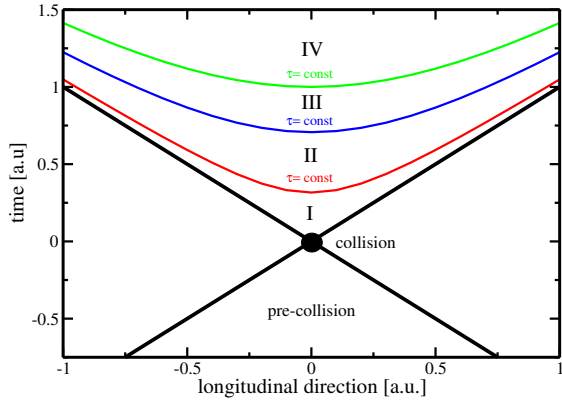


Figure 7: Schematic representation [49] of a heavy-ion collision as the function of time and longitudinal coordinates z . The various stages of the evolution correspond to proper time $\tau = \sqrt{t^2 - z^2}$ which is shown as hyperbolic curves separating the different stages.

505 occur. Now the system loses its deconfined, strongly coupled, state and hydrodynamics
 506 can no longer be used. The third stage is the hadron gas stage where the
 507 hadrons still interact. This ends when hadron scattering becomes rare and they
 508 no longer interact. In the final stage hadrons are free streaming and they fly in
 509 straight lines until they reach the detector.

510 The hydrodynamical approach treats the ensemble of particles as a fluid. It
 511 uses basic equations from hydrodynamics and thermodynamics but with a few
 512 modifications to account for the relativistic energies. The calculation is based
 513 on a collection of differential equations connecting the local thermal variables like
 514 temperature, pressure etc. to local velocities of the fluid. One also needs equations
 515 of state that connect the properties of the matter, e.g. temperature and pressure
 516 to density. Given initial conditions and equations of state the calculation gives the
 517 time-evolution of the system.

518 At first only ideal hydrodynamics was used. Ideal hydrodynamics does not
 519 include viscosity but it is a relatively good approximation and it could predict
 520 phenomena like elliptic flow. For more detailed calculations also viscosity must be
 521 considered and viscosity itself is an interesting property of QGP.

522 1.4 Flow

523 In a heavy-ion collision the bulk particle production is known as flow. The pro-
 524 duction is mainly isotropic but a lot of studies including my thesis focus on the
 525 small anisotropies. After the formation of the QGP, the matter begins to expand
 526 as it is driven outwards by the strong pressure difference between the center of the
 527 collision zone and the vacuum outside the collision volume. The pressure-driven
 528 expansion is transformed into flow of low-momentum particles in the hadroniza-
 529 tion phase. Since the expansion is mainly isotropic the resulting particle flow is
 530 isotropic with small anisotropic corrections that are of the order of 10% at most.
 531 The isotropic part of flow is referred to as radial flow.

532 The transverse momentum spectra dN/dp_T in heavy-ion collisions is shown

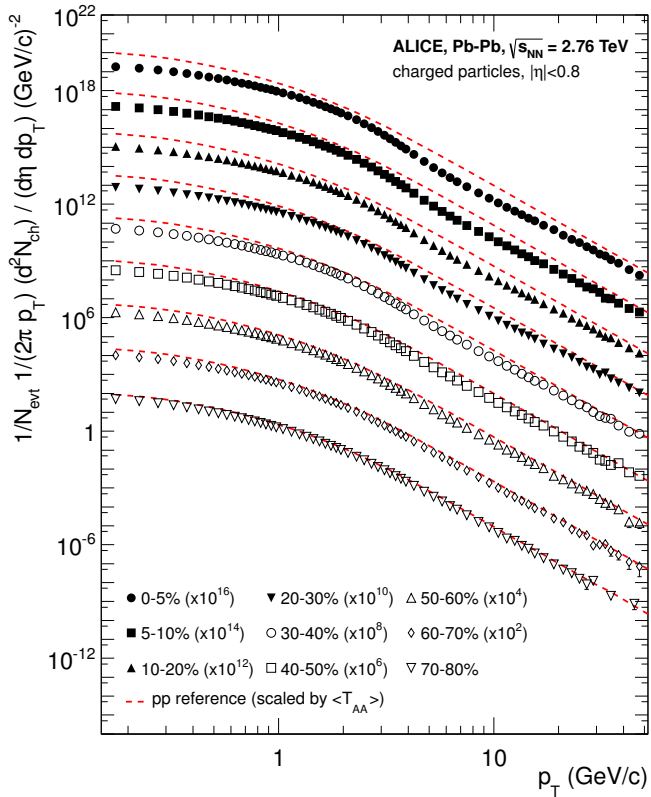


Figure 8: Charged particle spectra measured by ALICE [54] for the 9 centrality classes given in the legend. The distributions are offset by arbitrary factors given in the legend for clarity. The distributions are offset by arbitrary factors given in the legend for clarity. The dashed lines show the proton-proton reference spectra scaled by the nuclear overlap function determined for each centrality class and by the Pb-Pb spectra scaling factors [54].

533 in Fig. 8. The vast majority of produced particles have small p_T . The difference
 534 between the yield of 1 GeV/c and 4 GeV/c particles is already 2-3 orders of mag-
 535 nitude. Any observables that are integrated over p_T are therefore dominated by
 536 the small momentum particles.

537 1.4.1 Anisotropic Flow

538 In a non-central heavy-ion collision the shape of the impact zone is almond-like.
 539 In peripheral collisions the impact parameter is large which means a strongly
 540 asymmetric overlap region. In a central collision the overlap region is almost
 541 symmetric in the transverse plane. In this case the impact parameter is small.
 542 Collisions with different impact parameters are shown in Fig. 4.

543 The pressure gradient is largest in-plane, in the direction of the impact pa-
 544 rameter b , where the distance from high pressure, at the collision center, to low
 545 pressure, outside the overlap zone, is smallest. This leads to stronger collective
 546 flow into in-plane direction, which in turn results in enhanced thermal emission
 547 through a larger effective temperature into this direction, as compared to out-of-
 548 plane [5, 6, 55]. The resulting flow is illustrated in Fig. 9. Flow with two maxima
 549 in the direction of the reaction plane is called elliptic flow. This is the dominant

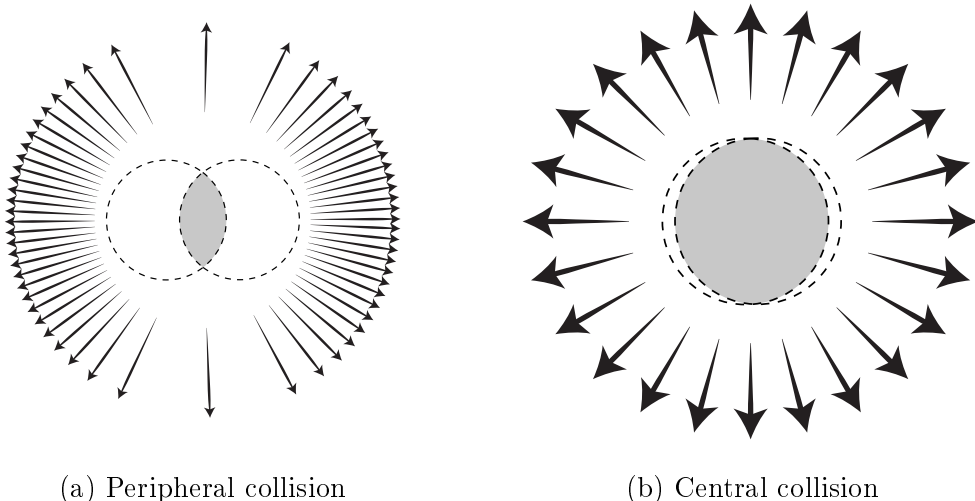


Figure 9: Illustration of flow in momentum space in central and peripheral collisions. The density of the arrows represent the magnitude of flow seen at a large distance from the collision in the corresponding azimuthal direction. In a peripheral collision momentum flow into in-plane direction is strong and flow into out-of-plane direction is weak. In a central collision anisotropy in flow is smaller, but the total yield of particles is larger.

part of anisotropic flow. Also more complex flow patterns can be identified. The most notable of these is the triangular flow, which is mainly due to fluctuations in the initial conditions.

Flow is nowadays usually quantified in the form of a Fourier composition

$$E \frac{d^3N}{dp^3} = \frac{1}{2\pi p_T} \frac{d^2N}{dp_T d\eta} \left(1 + \sum_{n=1}^{\infty} 2v_n(p_T, \eta) \cos(n(\phi - \Psi_n)) \right), \quad (13)$$

where the coefficients v_n give the relative strengths of different anisotropic flow components and the overall normalisation gives the strength of radial flow. Elliptic flow is represented by v_2 and v_3 represents triangular flow. The first coefficient, v_1 , is connected to directed flow. This will however in total be zero because of momentum conservation. It can be nonzero in some rapidity or momentum regions but it must be canceled by other regions.

The first approaches to quantifying the anisotropy of flow did not use the Fourier composition. Instead they approached the problem with a classic event shape analysis using directivity [56] or sphericity [5, 57] to quantify the flow.

The first experimental studies of anisotropy were performed at the AGS [58] in 1993. They noted that the anisotropy of particle production in one region correlates with the reaction plane angle defined in another region.

The first ones to present the Fourier decomposition were Voloshin and Zhang in 1996 [59]. This new approach was useful for detecting different types of anisotropy in flow, since the different Fourier coefficients give different harmonics in flow. They also show the relative magnitude of each harmonic compared to radial flow.

Some parts of the Fourier composition approach were used for Au-Au collisions at $\sqrt{s_{NN}} = 11.4\text{GeV}$ at AGS in 1994 [60]. This analysis still focused on event shapes but they constructed these shapes using Fourier composition from different rapidity windows.

Add a paragraph on the lessons learned from flow studies.

1.5 Hard processes

1.5.1 pQCD factorization

The term Hard Scattering is used in connection with the scattering of two point-like constituents (partons) of colliding nucleons, when the momentum transfer Q^2 is large ($Q \gg \Lambda_{\text{QCD}}$). Figure 11 shows the incoming partons, quarks or gluons, as they exchange a space-like virtual gluon and produce two highly virtual outgoing partons. The outgoing partons will eventually fragment into collimated showers of partons, referred to as jets

Jet fragmentation can be factorised into three components; the parton distribution functions f_a, f_b that give the probability of getting a parton with momentum

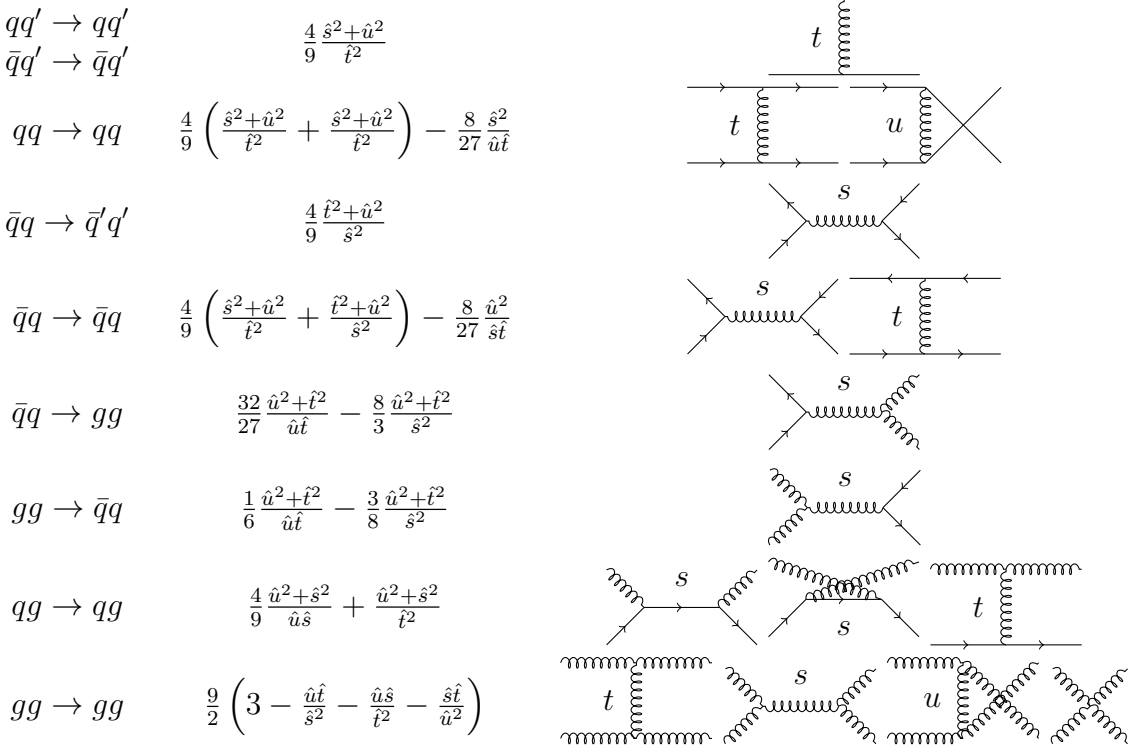


Figure 10: The basic pQCD processes and their quadratic matrix elements

fraction x of the proton, the cross section of the elementary scattering $ab \rightarrow cd$ (Fig. 10) and the fragmentation functions that give the probability of getting hadron h from the parton.

$$\frac{d\sigma_{pp}^h}{dy d^2 p_T} = K \sum_{abcd} \int dx_a dx_b f_a(x_a, Q^2) f_b(x_b, Q^2) \frac{d\sigma}{dt} (ab \rightarrow cd) \frac{D_{h/c}^0}{\pi z_c}, \quad (14)$$

where

$$x_{a,b} = \frac{|p_{a,b}|}{|p_{proton}|}.$$

Parton Distribution Function

Parton Distribution Functions (PDFs) are essential to calculate the scattering cross section. They are extracted from comprehensive global analysis of experimental results from a variety of fixed-target and collider experiments. PDFs $f_a(x)$ give the

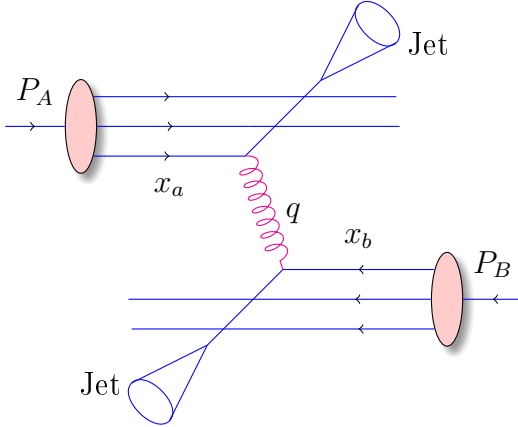


Figure 11: Schematic view of hard scattering process of $p + p \rightarrow 2 \text{ jets}$

593 differential probability for parton a to carry momentum fraction x of the proton
 594 momentum.

595 As the PDFs cannot be calculated from first principles. In practice the PDFs
 596 are measured in Deeply Inelastic Scattering (DIS) experiments and are extrapolated
 597 to the relevant momentum scales at LHC using the Dokshitzer-Gribov-Lipatov-
 598 Altarelli-Parisi (DGLAP) evolution scheme [61–63]

$$\mu_F^2 \frac{\partial f_i(x, \mu_F^2)}{\partial \mu_F^2} = \sum_j \frac{\alpha_s(\mu_F)}{2\pi i} \int_x^1 \frac{dz}{z} P_{ij}(z) f_j\left(\frac{x}{z}, \mu_F^2\right), \quad (15)$$

599 where μ_F is a factorization scale. The splitting functions P_{ij} describe a probability
 600 to radiate parton i from parton j as a function of the momentum fraction z carried
 601 away by the offspring parton.

602 Fragmentation functions

603 The final component in the factorization, fragmentation functions, describe the
 604 distribution of the fractional momenta of particles radiated from the outgoing
 605 parton. Fragmentation function are given with respect to the momentum fraction
 606 z which is defined as the longitudinal momentum fraction of jet momentum p_{jet}
 607 carried away by the jet fragment p_{part}

$$z = \frac{\bar{p}_{\text{part}} \cdot \bar{p}_{\text{jet}}}{p_{\text{jet}}^2} = \frac{p_{\text{part}}}{p_{\text{jet}}} \Big|_{\bar{p}_{\text{part}} \times \bar{p}_{\text{jet}} = 0} \quad (16)$$

608 Fragmentation function $D(z)$ then gives the average multiplicity m of jet frag-
 609 ments having $z > z_0$ [1].

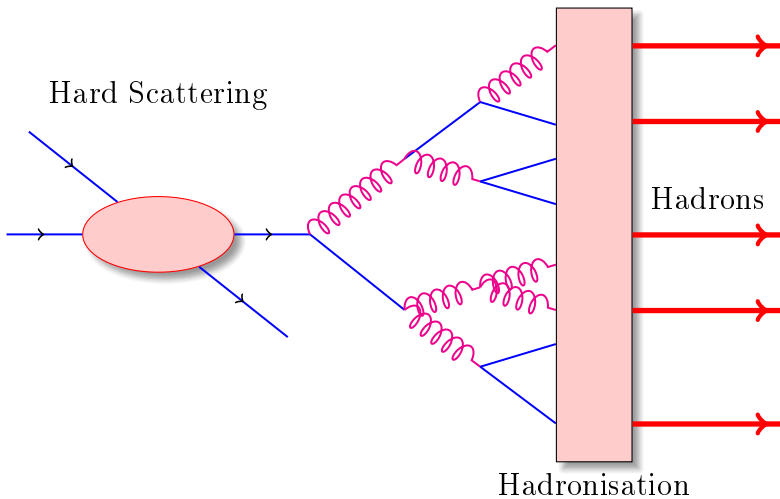


Figure 12: An illustration of jet showering. The highly virtual parton from the hard scattering will produce a shower of softer partons. When the virtuality is low enough the shower will go through a hadronisation process that produces the hadrons, which will be eventually observed in the detector.

$$m(z_0) = \int_{z_0}^1 D(z) dz \Rightarrow m(0) \equiv \langle m \rangle = \int_0^1 D(z) dz \quad (17)$$

610 Because of momentum conservation the sum of all jet fragments must be equal
611 to the jet momentum, i.e.

$$\sum p_{i,\text{part}} = p_{\text{jet}} \Rightarrow \sum z_i = 1 \Rightarrow \int_0^1 z D(z) dz = 1 \quad (18)$$

612 A natural consequence is that the average momentum fraction is the inverse of
613 the average multiplicity

$$\langle z \rangle = \frac{\int_0^1 z D(z) dz}{\int_0^1 D(z) dz} = \frac{1}{\langle m \rangle}. \quad (19)$$

614 1.5.2 Jet hadronisation

615 When the parton shower reaches a scale close to Λ_{QCD} , the perturbative descrip-
616 tion is no longer valid. Thus the hadronisation stage must be described in a
617 non-perturbative manner. One simple scenario that is used in several theory calcu-
618 lations is the so-called local parton-hadron duality [64]. In the local parton-hadron
619 duality hypothesis it is assumed that there exists a low virtuality scale Q_0 in which

the hadronisation happens, that is independent of the scale of the primary hard process. At this scale the partons are transformed into hadrons, assuming that the flow of momentum and quantum numbers for the hadrons can be directly obtained from those of partons introducing only small normalising constants.

624 Lund string model

One common implementation in MC generators is the Lund string fragmentation algorithm [65]. The string model is based on the fact that in QCD linear confinement is expected over large distances [66]. This can be modelled by imagining a colour flux tube being stretched between the outgoing partons. The left side of Fig. 13 illustrates this point for a $q\bar{q}$ -pair. The tube is assumed to have a uniform fixed transverse size of about 1 fm along its length, which leads to a linearly rising potential $V(r) = \kappa r$, where the string constant κ describes the amount of energy per unit length. A value of $\kappa \approx 1 \text{ GeV/fm} \approx 0.2 \text{ GeV}^2$ can be obtained from hadron mass spectroscopy.

The evolution of string fragmentation is illustrated schematically on the right side of Fig. 13. This figure is drawn in a light cone presentation, so the initial quark and antiquark are going to separate directions at the speed of light, which assumes them as massless. The string between them, illustrated in the figure by the red line, stretches until its potential energy becomes high enough that it can break, forming a new quark-antiquark pair. If the original pair was $q\bar{q}$ and the new pair $q'\bar{q}'$, now two new pairs $q\bar{q}'$ and $q'\bar{q}$ have formed. As these particles are also moving away from each other, the strings between them can stretch and break, creating yet more pairs. The process continues until the invariant mass of the system connected by the string becomes small enough and a final state meson is formed.

To mathematically model the string one can use a massless relativistic string with no transverse degrees of freedom. The gluons are represented as energy and momentum carrying kinks on the string with incoherent sums of one colour charge and one anticolour charge. When this string breaks, it is classically required that the created quark and antiquark are produced at a certain distance if they are to have any mass or transverse momentum. However, taking into account quantum mechanics, the pair must be created at one point and then tunnel out to the classically allowed region. Thus the probability to create a new quark-antiquark pair becomes proportional to the tunnelling probability [65].

$$P_{\text{tunnelling}} \propto \exp\left(\frac{-\pi m_\perp^2}{\kappa}\right) = \exp\left(\frac{-\pi m^2}{\kappa}\right)\left(\frac{-\pi p_\perp^2}{\kappa}\right), \quad (20)$$

where the transverse mass m_\perp is defined as $m_\perp^2 = m^2 + p_\perp^2$. The transverse momentum is now defined to be transverse to the string axis. This formula gives

656 flavour-independent Gaussian p_\perp -distribution for the created $q\bar{q}$ pairs.

657 As explained above the string fragmentation would only produce mesons in
658 the final state, but we know that also baryons are created in the process. In the
659 string fragmentation model baryon production is included by adding a probability
660 that a diquark-antidiquark pair is created instead of a quark-antiquark pair when
661 a string breaks.

662 The kinematics of each string breaking are determined iteratively. Since there
663 is no natural ordering, the string breaking can be considered in any order and
664 the answer obtained must be the same. One can start from the q leg and work
665 one's way to the \bar{q} leg, or vice versa. This give a left-right symmetry of the
666 string fragmentation. In the Lund model this is taken into account by defining a
667 symmetric fragmentation function

$$f(z) \propto \frac{1}{z} (1-z)^a \exp\left(-\frac{bm_\perp^2}{z}\right) \quad (21)$$

668 to break the string into a hadron and a remainder system. Here z is the fraction
669 of light-cone momentum p^+ given to the hadron in the string breaking, m_\perp is the
670 transverse mass of the hadron and a and b are tunable parameters of the model.
671 For heavy quarks this has to be modified as

$$f(z) \propto \frac{1}{z^{1+bm_Q^2}} (1-z)^a \exp\left(-\frac{bm_\perp^2}{z}\right) \quad (22)$$

672 The process can be thought as follows: first start from the q -leg of a $q\bar{q}$ system
673 and choose to consider the breaking to new $q'\bar{q}'$ pair closest to this leg. Now the
674 breaking will produce a hadron $q\bar{q}'$ and a remainder system spanning from $q'\bar{q}$.
675 Then the process is continued until the \bar{q} -leg is reached. A small detail here is
676 that in equation (21) it is assumed that the mass of the remainder system is large.
677 Thus some patching up is needed for the last two hadrons coming from a string.
678 The patching up is done such that the place where it happens looks as closely like
679 any other string break as possible.

680 One additional possibility one must consider is that a string can have such a
681 low mass that it cannot break at all. In this case a single hadron is generated out
682 of the string and if necessary energy and momentum are exchanged with other
683 partons in the event.

684 After all the hadrons are produced, the short-lived ones can still decay before
685 the set of final state particles in the simulation is obtained []

686 Cluster model

687 Instead of a string model HERWIG [] uses a cluster model [67] for hadronisation.
688 The advantage of cluster models is that they require a smaller number of param-

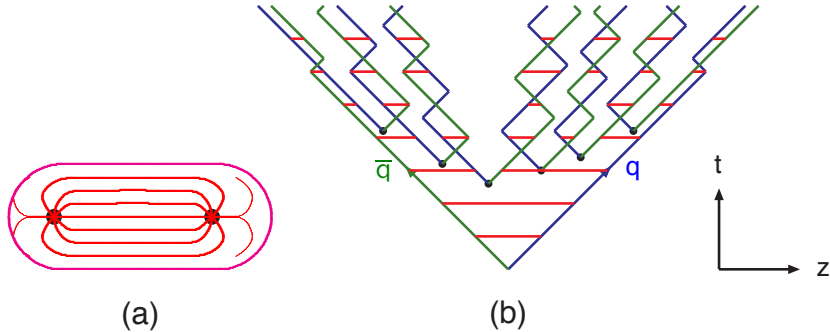


Figure 13: (a) A flux tube spanned between a quark and an antiquark. (b) The motion and breakup of a string system, with the two transverse degrees of freedom suppressed (diagonal lines are (anti)quarks, horizontal ones snapshots of the string field). [66]

eters than string models. The model is based on the preconfinement property of parton showers, i.e. the colour structure of the shower at any evolution scale Q_0 is such that colour singlet combinations of partons can be formed with an asymptotically universal invariant mass distribution. The invariant mass does not depend on the initial hard process scale Q , but only on Q_0 and the QCD scale Λ_{QCD} , when $Q \gg Q_0$.

The cluster model starts from transforming all gluons non-perturbatively into $q\bar{q}$ pairs, which requires that the gluons get a mass, which must be at least twice the lightest quark mass. After the gluons are transformed into quarks, the adjacent colour lines can be clustered together to colour singlet states with mesonic quantum numbers. The momentum of these clusters is defined to be the sum of the momenta of the clustering partons. According to preconfinement, the mass distribution of these clusters is independent of the details of the hard scattering. Additionally the clusters can be regarded as highly excited hadron resonances and decayed into the final state hadrons.

Some of these initial clusters are too heavy to reasonably describe an excited state of a hadron. These must be split before they are allowed to decay. The cluster C is split if its mass fulfils the condition []

$$M_C^p \geq M_{\max}^p + (m_1 + m_2)^p, \quad (23)$$

where $m_{1,2}$ are the masses of the constituents partons of the cluster and M_{\max} and p are the main parameters of the model. These have to be chosen separately for clusters containing light, charmed and bottom quarks. When a cluster is split, a pair of light quarks is generated from the vacuum and two new clusters are made, both containing one quark from the original cluster and one from the newly gen-

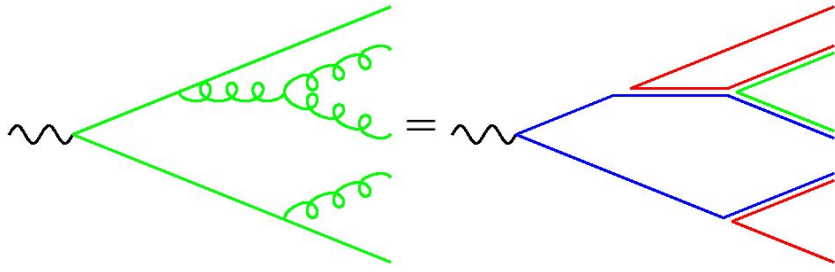


Figure 14: Colour structure of a parton shower to leading order in N_c . [66]

erated pair. The splitting is continued until no clusters with masses M_C fulfilling the equation 23 remains.

When the clusters are light enough, they decay into final state hadrons. If the mass of the cluster is high enough for decaying into a baryon-antibaryon pair, there is a parameter deciding whether the cluster undergoes mesonic or baryonic decay. For a mesonic decay a quark-antiquark pair is created from the vacuum and for the baryonic decay a diquark-antidiquark pair is made. Then the exact decay products are chosen and the cluster decays isotropically in the rest frame of the cluster. If there are partons produced in the perturbative phase involved in the decay, they retain their original direction in the cluster rest frame, up to some Gaussian smearing. If the cluster mass is too low to decay into a pair of mesons, it decays into the lightest possible hadron and some energy and momentum is exchanged with the adjacent clusters. At the end we are left with the final state hadrons, some of which might still decay until the end of the simulation if they are very short-lived. []

1.5.3 Jet energy loss

Discovery of jet quenching via leading hadron suppression

First evidence of jet quenching comes from observing high p_T tracks, i.e. the leading hadrons.

Jet quenching in heavy-ion collisions is usually quantized with the nuclear modification factor R_{AA} , which is defined as

$$R_{AA}(p_T) = \frac{(1/N_{AA}^{evt}) dN^{AA}/dp_T}{\langle N_{coll} \rangle (1/N_{pp}^{evt}) dN^{pp}/dp_T} \quad (24)$$

where dN^{AA}/dp_T and dN^{pp}/dp_T are the yields in heavy-ion and proton-proton collisions, respectively and $\langle N_{coll} \rangle$ is the average number of binary nucleon-nucleon collisions in one heavy-ion event. The number of binary collisions can be calculated from the Glauber model as shown in Sec. 1.3.2. From the point of view of direct

737 production a heavy-ion collision can be estimated relatively well to be only a series
 738 of proton-proton collisions.

739 If the medium has no effect on high p_T particles the nuclear modification factor
 740 should be 1. At RHIC and LHC this has been observed to be as low as 0.2 because
 741 of jet quenching. Measurements of R_{AA} from different sources are shown in Fig. 15

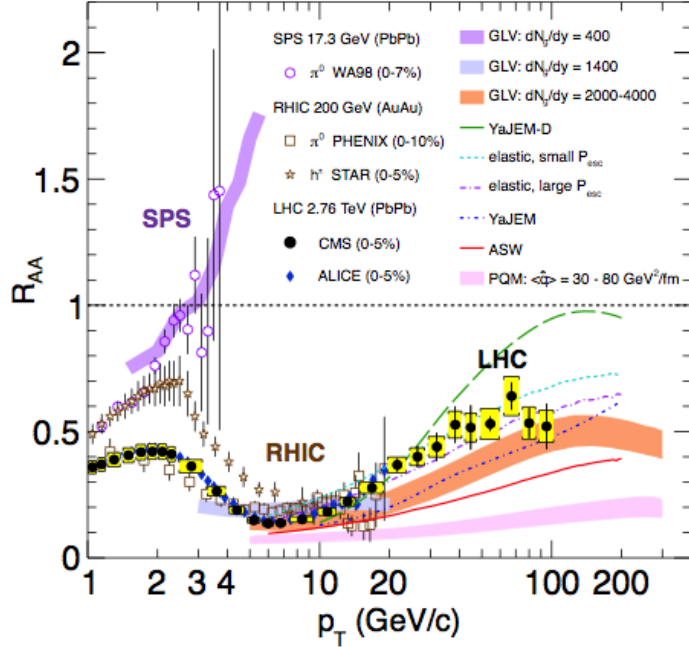


Figure 15: Measurements of the nuclear modification factor R_{AA} in central heavy-ion collisions at three different center-of-mass energies, as a function of p_T , for neutral pions (π^0), charged hadrons (h^\pm), and charged particles [68–72], compared to several theoretical predictions [34, 73–77]. The error bars on the points are the statistical uncertainties, and the yellow boxes around the CMS points are the systematic uncertainties. The bands for several of the theoretical calculations represent their uncertainties [78].

742 The nuclear modification factor can also be used to quantify anisotropy. In
 743 the study of anisotropy R_{AA} in-plane and out-of-plane can be compared. The
 744 distance traveled through medium is largest out-of-plane which leads to stronger
 745 suppression in this direction. The nuclear modification factor as a function of
 746 $\Delta\phi = \phi - \psi_n$ is given by

$$\begin{aligned}
R_{AA}(\Delta\phi, p_T) &= \frac{(1/N_{AA}^{evt}) d^2 N^{AA}/d\Delta\phi dp_T}{\langle N_{coll} \rangle (1/N_{pp}^{evt}) dN^{pp}/dp_T} \approx \frac{dN^{AA}/dp_T (1 + 2 \cdot v_2 \cos(2\Delta\phi))}{\langle N_{coll} \rangle dN^{pp}/dp_T} \\
&= R_{AA}^{incl}(p_T) (1 + 2 \cdot v_2 \cos(2\Delta\phi)). \tag{25}
\end{aligned}$$

The yield of proton-proton collisions is independent of the reaction plane and the yield in heavy-ion collisions is modulated by the second harmonics. In Eq. (25) R_{AA} is approximated only up to the second harmonics. From Eq. (25) it follows that

$$\frac{R_{AA}(0, p_T) - R_{AA}(\pi/2, p_T)}{R_{AA}^{incl}(p_T)} \approx \frac{R_{AA}^{incl}(p_T) (1 + 2 \cdot v_2 - (1 - 2 \cdot v_2))}{R_{AA}^{incl}(p_T)} = 4 \cdot v_2 \tag{26}$$

The observed $R_{AA}(\Delta\phi, p_T)$ from PHENIX measurements in Au-Au collisions at $\sqrt{s} = 200\text{GeV}$ [79] is compared to R_{AA} using v_2 via Eq. (25) in Fig. 16. They agree very well within the statistical errors for all centrality and p_T bins.

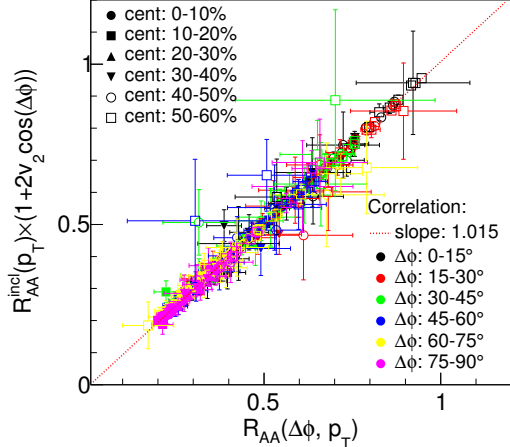


Figure 16: A comparison between observed $R_{AA}(\Delta\phi, p_T)$ and R_{AA} using v_2 from PHENIX measurements of Au-Au collisions at $\sqrt{s} = 200\text{GeV}$. On the X-axis is the measured $R_{AA}(\Delta\phi, p_T)$. On the y-axis is the inclusive R_{AA} multiplied by $1 + 2v_2 \cos(\Delta\phi)$ [79].

At high- p_T , the pQCD processes are dominant, hence the v_n (or $R_{AA}(\Delta\phi, p_T)$) characterize the pathlength-dependence of the energy loss process.

Jet quenching is not the only high p_T phenomenon studied in heavy-ion collisions. Another property is jet fragmentation. The high momentum parton created in the initial collision fragments into a number of partons with smaller p_T . Jet fragmentation occurs also in proton-proton collisions in the vacuum, but it can be modified due to the presence of the medium. In order to study the jet fragmentation function ($D(z)$, where $z = p_T^h/p_T^{part}$) modification due the medium, we use the two-particle correlations. The particle yield can be extracted from the correlation function. The background from the flow processes is correlated and needs to be subtracted to get the particle yield associated only with the jet. The ratio of the jet yields in Au-Au and p-p collision $I_{AA} = Y^{Au+Au}/Y^{p+p}$ characterizes the jet fragmentation modification [80]. I_{AA} probes the interplay between the parton production spectrum, the relative importance of quark-quark, gluon-gluon and quark-gluon final states, and energy loss in the medium.

Theory of jet quenching

High momentum particles are very rare and they are only produced in the initial collisions. After they are created they escape the medium before a thermal equilibrium is reached. Thus they are not part of the pressure-driven collective expansion. Instead high momentum yield is suppressed because of energy loss in the medium. When propagating through the medium these partons lose energy as they pass through the medium. This is referred to as jet quenching. Jet quenching depends on the path lengths through the medium. Thus anisotropy in this region is mainly dependent on the collision geometry and density of medium.

The energy loss of partons in medium is mainly due to QCD bremsstrahlung and to elastic scatterings between the parton and the medium.

The radiative energy loss mechanism is given in terms of the transport coefficient $\langle \hat{q} \rangle$, which describes the average momentum transfer between the medium and parton [82]. The exact definition of this depends on the theoretical formalism used to describe the energy loss mechanism.

Many of the energy loss models exploit the analogy between the QCD interaction of parton propagating through the colored medium and the QED energy loss of electron propagating through material. An electron propagating through matter loses its energy by photon Bremsstrahlung radiation. In the simplest case, each individual scattering center results in a single emission of a photon. This is known as the Bethe-Heitler regime [83]. The energy spectrum of radiated photons dN/dE is, in this case, proportional to $1/E$. However, the Bremsstrahlung photon, can be radiated only when the distance between the scattering centers is larger than the formation length. In the limit, when the scattering centers are closer than the formation length, the Bremsstrahlung process is suppressed. This phenomenon is known as the Landau-Pomeranchuk-Migdal (LPM) [84, 85] suppression. The

795 radiated spectrum in this regime is proportional to $1/\sqrt{E}$.

796 Lower energy photons are further suppressed by the destructive interference
797 leading to the suppression of Bremsstrahlung photons of $E < \gamma\omega_p$, where ω_p is
798 the plasma frequency of the radiator. This is known as Dielectric suppression.
799 The photon energy distribution in this regime is proportional to the energy of the
800 photon. A schematic view of the effect of these three regimes is shown in Fig. 18.

801 The simplest energy loss process is elastic QCD scattering off the medium par-
802 tons. In elastic scatterings the recoil energy of the scattered partons are absorbed
803 by the thermal medium, which reduces the energy of the initial parton. The mean
804 energy loss from elastic scatterings can be estimated by

$$\langle \Delta E \rangle_{\text{el}} = \sigma \rho L \langle E \rangle_{\text{1scatt}} \propto L, \quad (27)$$

805 where σ is the interaction cross section and $\langle E \rangle_{\text{1scatt}}$ is the mean energy transfer
806 of one individual scattering [87]. This assumption holds if the mean energy is
807 independent of the total energy of the parton (E). The transport coefficient of
808 elastic scattering, $\langle \hat{q}_{\text{el}} \rangle = \langle \Delta E \rangle / L$, is defined as the mean energy loss per unit path
809 length.

810 Another energy loss mechanism is medium-induced radiation. In QCD this
811 radiation is mainly due to the elementary splitting processes, $q \rightarrow qg_r$ and $g \rightarrow gg_r$.
812 Assuming that the parton is moving with the speed of light radiation energy loss
813 can be estimated by

$$\langle \Delta E \rangle_{\text{rad}} \propto T^3 L^2, \quad (28)$$

814 where L is the length of the medium and T is its temperature [88]. The differ-
815 ent exponents of L in equations 27 and 28 indicate that radiative energy loss is
816 dominant over elastic energy loss.

817 There are several models that attempt to describe the nature of the energy loss
818 mechanism. The most used models can be divided into four formalisms.

819 In the Gyulassy-Levai-Vitev (GLV) [89] opacity expansion model the radiative
820 energy loss is considered on a few scattering centers N_{scatt} . The radiated gluon
821 is constructed by pQCD calculation as summing up the relevant scattering am-
822 plitudes in terms of the number of scatterings. Another approach into opacity
823 expansion is the ASW model by Armesto, Salgado and Wiedermann [90].

824 Thermal effective theory formulation by Arnold, Moore and Yaffe (AMY) [91]
825 uses dynamical scattering centers. It is based on leading order pQCD hard thermal
826 loop effective field theory. This model assumes that because of the high temper-
827 ature of the plasma the strong coupling constant can be treated as small. The
828 parton propagating through the medium will lose energy from soft scatterings and
829 hard scatterings.

830 The above models calculate the energy loss while the parton propagates through
831 the medium, focusing on the pQCD part. The higher twist (HT) approach by Wang
832 and Guo [92] implements the energy loss mechanism in the energy scale evolution
833 of the fragmentation functions.

834 The last category is formed by the Monte Carlo methods. The PYTHIA event
835 generator [93] is widely used in high-energy particle physics. Two Monte Carlo
836 models based on PYTHIA describing the energy loss mechanism are PYQUEN [94]
837 and Q-Pythia [95]. Other Monte Carlo models include JEWEL [96] and Ya-
838 JEM [97].

839 1.5.4 New paradigm of jet Quenching

840 As described in the previous section there have been many experimental evi-
841 dences of jet energy loss, such as the suppression of inclusive hadron spectra at
842 high transverse momentum [98–102], the modification of back-to-back hadron-
843 hadron [80, 103] and direct photon-jet correlations [104], and the modification of
844 reconstructed jet spectra [105] and jet substructure [106–108], as compared to the
845 expectations from elementary proton-proton collisions.

846 The first indications of jet quenching, such as R_{AA} , looked essentially at the
847 leading hadrons of jets, the hard part, ignoring the soft scale part of jet phenomena.
848 However, experimental methods have since improved; jet reconstruction algorithms
849 have become reliable in the LHC era. Instead of the leading hadron we can study
850 the entire jet shower.

851 -Jet RAA -Jetscape

852 Thus the new paradigm in jet quenching in heavy-ion collisions involves multi-
853 scale problems [109, 110]. The elementary scattering and the subsequent branching
854 process down to non-perturbative scales are dominated by hard scales in the vac-
855 um as well as in the medium. Soft scales, of the order of the temperature of
856 the medium, characterise the interactions of soft partons produced in the shower
857 with the QGP. Soft scales also rule hadronisation, which is expected to take place
858 in vacuum for sufficiently energetic probes, even though some modifications can
859 persist from modifications of color flow [111–113]. Understanding the contribu-
860 tions from the different processes to the jet shower evolution in medium and their
861 scale dependence is crucial to constrain the dynamics of jet energy loss in the
862 expanding medium, the role of colour coherence [114], and fundamental medium
863 properties like temperature dependent transport coefficient [115, 116].

864 Lund diagram

865 The different momentum and angular scales are subject to different physical phe-
866 nomena. Figure 19 shows the relevant medium modification phenomena for differ-

867 ent regions of the phase space at time t , when a jet propagates through a thermal
 868 cloud of temperature T . As in practice jets propagate over a finite path-length
 869 L in QCD matter, Fig. 19 can be taken as a representation of the distribution of
 870 partonic jet fragments at moment $t \approx L$, when the jet escapes the medium.

871 The region marked as DGLAP is dominated by the primary vacuum splittings.
 872 This region is determined by $\theta > \theta_{\text{vac}}$ with

$$\theta_{\text{vac}} \propto 1/\sqrt{pt}. \quad (29)$$

873 Medium-induced parton branching fills the $\log p$ - $\log \theta$ -plane from the bottom
 874 up (in p) and from the inside out (in θ). This is because transverse momentum is
 875 acquired by Brownian motion in the medium, $k_{\perp}^2 \propto \hat{q}t$. Then the formation time
 876 constraint $t \geq p/k_{\perp}^2 \approx p/\hat{q}t$ implies that medium-induced quanta can be formed in
 877 the region $p \leq k_{\text{form}}$ where

$$k_{\text{form}}(t) = \hat{q}t^2$$

878 .

879 The probability of finding a splittee with a momentum p with $p < k_{\text{form}}$ is

$$\frac{dP_{\text{find}}(t)}{d \log p} \propto \alpha_s t/t_{\text{form}}(p) \propto \alpha_s \hat{q}^{nicefrac{1}{2}} p^{-1/2} t \quad (30)$$

880 Not all quanta will stay where they were created. Those modes that have time
 881 to lose a significant fraction of their energy will cascade to a significantly lower
 882 scale p . For LPM-type radiation, the splitting that degrades energy the most is
 883 the hardest splitting.

884 The $\log p$ distribution has the same $\frac{1}{\sqrt{p}}$ dependence as in the LPM region

$$\frac{dn}{d \log p} = \frac{1}{p} \frac{d\epsilon}{d \log p} \approx \alpha_s \frac{\sqrt{\hat{q}t}}{\sqrt{p}} \quad (31)$$

885 Also the quanta originating from the DGLAP region will undergo medium
 886 interactions that will make the quanta radiate and split. The distribution of radi-
 887 ation is the same as from any other mode. Above a certain momentum scale k_{split}
 888 the distribution of originating daughters is

$$\frac{dP_{\text{find}}}{d \log p d \log \theta} \approx \alpha_s \frac{t}{t_{\text{split}}(p)}, \quad (32)$$

889 Note that the ratio t/t_{split} is smaller than 1 for nodes above k_{split} and therefore
 890 the number of daughters is smaller than the number of vacuum splitted quanta.
 891 Below k_{split} the cascade is similar to the medium cascade and the number of quanta
 892 become

$$\frac{dn}{d \log p d \log \theta} \approx \alpha_s \frac{t}{t_{\text{split}}(p)}, \text{ for } p < k_{\text{split}}(p) \quad (33)$$

893 The angular distribution is driven by two mechanisms; Multiple soft scatterings
 894 give rise to transverse Brownian motion, which determines the distribution at small
 895 angles. The typical angle reached in the LPM region is

$$\theta_{\text{BR}}(p) \approx \frac{\sqrt{\hat{q}t}}{p}, \text{ for } k_{\text{form}} > p > k_{\text{split}}, \quad (34)$$

896 while in the medium cascade region of the phase space this becomes

$$\theta_{\text{BR}}(p) \approx \left(\frac{T}{p}\right)^{\frac{3}{4}} \quad (35)$$

897 Large angular scales cannot be reached by Brownian motion, but can arise from
 898 rare large angle scatterings, described by Molière [].

899 1.5.5 Jet shape measurements

900 1.6 QGP in Small systems

901 After the existence of QGP in heavy-ion collisions has been established, attention
 902 has been turned to small systems. Proton-proton (pp) and proton-Lead (pPb)
 903 collisions have been studied at LHC and RHIC has studied a host of different
 904 collision systems; namely proton-Gold (pAu), deuteron-Gold (dAu) and Helium³-
 905 Gold (He³Au) collisions starting in 2000.

906 Already before the era of modern colliders, collective behaviour in proton-
 907 proton collisions was considered by names like Heisenberg, Fermi and Bjorken. [117]
 908 Eventually there were some experimental searches of QGP in pp and $p\bar{p}$ collisions
 909 in E735 at Tevatron [118] and MiniMAX [119]. However no conclusive evidence
 910 was found.

911 In the early years of RHIC these small systems were mostly considered as con-
 912 trol measurement, for example in constraining nuclear modified parton distribution
 913 functions (nPDFs) that determine the initial gluon distributions that determine
 914 the first epoch of heavy-ion collisions [120, 121].

915 In 2010 ultrahigh-multiplicity pp collisions were studied at CMS. The study
 916 found that particles had a weak but clear preference to be emitted along a com-
 917 mon transverse ϕ angle across all rapidities [122]. This seemed like behaviour
 918 were similar to AA collisions, but it was argued that it could as well come from
 919 momentum correlations present in the earliest moments of the collision.

920 In 2012 LHC ran its first pPb data taking period. Around the same time
 921 dAu data was reexamined at RHIC. Now it was revealed that most of the flow

922 signatures attributed to hydrodynamic expansion in AA collisions also existed in
923 smaller systems.

924 -Sub nucleonic structure needed to describe intial conditions in pA, pp

925 1.6.1 Collective phenomena

926 The most rugged analysis of collective behaviour concerns the two (or more) parti-
927 cle correlations, often parametrised via the relative azimuthal angle and pseudora-
928 pidity differences, $\Delta\phi$ and $\Delta\eta$ respectively. Figure 21 shows two-particle correla-
929 tions measurements in PbPb, pPb and pp collisions at the LHC. In PbPb collisions
930 long-range correlations dominate over short-range phenomena. This shows in the
931 two ridges at $\Delta\phi = 0$ and $\Delta\phi = \pi$. At $\Delta\phi \approx \Delta\eta \approx 0$, there is a peak coming from
932 single jet fragmentation. Since the away-side jet can be spread out in $\Delta\eta$, this
933 contribution disappears when compared to the flow contribution at the away side
934 ridge. In pPb, and pp the near side peak is more distinguished and the away-side
935 jet contribution starts to show. Still, one can see long-range correlations that seem
936 like flow-like collective behaviour in both systems.

937 In addition to the two particle correlations, correlations have been observed in
938 the form of v_n coefficients both at LHC and at RHIC. The results have also been
939 described with hydrodynamical models, although the applicability of said models
940 is questionable, because of the large Reynolds numbers in small systems. Figure
941 20 shows results for v_2 in different collisions systems at RHIC as measured by
942 PHENIX. These different systems provide also different initial geometries. dAu
943 collisions naturally have an ellipsoidal form, while a He3 collision has a triangular
944 form and thus produces larger triangular flow, v_3 components.

945 Other observations that produce flow-like results include mass ordered v_2 coeffi-
946 cients and higher order harmonics coming from fluctuations in the initial geometry.
947 Thus all the major collective flow phenomena observed in heavy-ion collisions have
948 been also identified in small systems.

949 One open question is identifying the point the point, where flow-like corre-
950 lations end. The question has proved challenging since low multiplicity events are
951 dominated by non-flow phenomena. This makes observations in low multiplicity
952 events model/method dependant. Different methods assess non-flow contributions
953 differently. Thus some methods fail to observe a signal in cases, where others do
954 and it is unclear whether this is true collective motion or it comes from non-flow
955 contributions.

956 1.6.2 Absence of jet quenching

957 In A+A collisions, an important confirmation of the standard model comes from
958 the energy loss of high p_T partons traversing the medium, referred to as jet quench-

ing [123–125]. In 2003 the jet quenching effect was observed to disappear in d+Au collisions. This was taken as an indication that no QGP was created. Similarly at LHC no jet modification has been observed in pPb collisions. Fig. 22 shows the nuclear modification factor R_{pA} in pPb collisions as measured at the LHC.

The lack of jet modification seems surprising considering the multitude of flow observations supporting the existence of QGP in small systems. One possible explanation is simply the size of medium. In PbPb collision partons traversing through the medium lose energy to the medium. If the medium is very small there is limited time for interaction with the medium.

Calculations indicate that there should be modification in the most central pPb collisions, but selecting these in the analysis is complicated. In PbPb collisions most of the particle production comes from the medium and thus the total multiplicity is a good indicator of centrality. In pPb collisions, however the total multiplicity is smaller and is more strongly influenced by jet phenomena. Events with jets have naturally larger multiplicities and are more likely to be classified as central events.

So far the only observable indicative of jet quenching in pPb collisions is the high $p_T v_2$. In heavy-ion collisions this is not explained by hydrodynamics. Instead it is assumed to come from jet quenching with different path lengths through the medium in different directions. In Fig.22 ATLAS and CMS measurements of v_2 in pPb and PbPb collisions are shown. The pPb results seem to follow a very similar pattern.

Table 1: Summary of observations in small system

Observable	PbPb	pPb	pp
Jet RpA/RAA	Modified	No modification	-
Hadron RpA/RAA	Modified	No modification	-
Heavy flavors			
Jet shape	Broadening	No observations	-
Two-particle correlations	Ridge	Ridge	Ridge
v_2	Observed	Observed	Observed
Mass ordered flow			
Higher ordered harmonics			
High $p_T v_2$	Observed	Maybe	-

1.6.3 Centrality determination in small systems

In lead-lead collisions the total multiplicity of the event is a good indicator of the centrality of the collision. In proton-lead collisions the connection of multiplicity and centrality is less clear. In p-Pb collisions the impact parameter is only

985 loosely correlated to N_{part} or N_{coll} . Hence, although one uses traditionally the
986 term centrality to refer to these measurements, the relevant parameters are N_{part}
987 and N_{coll} [1].

988 The Glauber model [43] is generally used to calculate geometrical quantities of
989 nuclear collisions (A–A or p–A). In this model, the impact parameter b controls the
990 average number of participating nucleons N_{part} and the corresponding number of
991 collisions N_{coll} . It is expected that variations of the amount of matter overlapping
992 in the collision region will change the number of produced particles, and parameters
993 such as N_{part} and N_{coll} have traditionally been used to describe those changes
994 quantitatively, and to relate them to ppcollisions.

995 The problem in p–Pb collisions, is that fluctuations in multiplicity coming from
996 for example hard scatterings are of the same order as the differences in multiplicity
997 between centrality classes. In Pb–Pb collisions these multiplicity fluctuations have
998 little influence on the centrality determination, the range of N_{part} or N_{coll} is large
999 and $P(M|v)$ converges quickly to a Gaussian with a small width relative to the
1000 range of v .

1001 Thus in practice selecting high multiplicity one chooses not only large average
1002 N_{part} , but also positive multiplicity fluctuations leading to deviations from the
1003 binary scaling of hard processes. These fluctuations are partly related to qualita-
1004 tively different types of collisions. High multiplicity nucleon-nucleon collisions
1005 show a significantly higher particle mean transverse momentum. They can be
1006 understood as harder collisions with larger momentum transfer Q^2 or as nucleon-
1007 nucleon collisions where multiple parton-parton interactions (MPI) take place.
1008 This is illustrated in Fig. 24.

1009 Of particular interest are estimators from kinematic regions that are causally
1010 disconnected after the collision. The measurement of a finite correlation between
1011 them unambiguously establishes their connection to the common collision ge-
1012 ometry. Typically these studies are performed with observables from well sep-
1013 arated pseudorapidity (η) intervals, e.g. at zero-degree (spectators, slow-nucleons,
1014 deuteron break-up probability) and multiplicity in the rapidity plateau.

1015 One centrality selection that is argued not to induce a bias on the binary scaling
1016 of hard processes is provided by the energy measurement with the Zero Degree
1017 Calorimeters (ZDC) in ALICE, due to their large η -separation from the central
1018 barrel detectors. They detect the "slow" nucleons produced in the interaction by
1019 nuclear de-excitation processes or knocked out by wounded nucleons.

1020 Additional kinematic biases exist for events containing high- p_{T} particles, which
1021 arise from the fragmentation of partons produced in parton-parton scattering with
1022 large momentum transfer. Their contribution to the overall multiplicity increases
1023 with increasing parton energy and thus can introduce a trivial correlation between
1024 the centrality estimator and the presence of a high- p_{T} particle in the event. For

¹⁰²⁵ very peripheral collisions, the multiplicity range that governs the centrality for the
¹⁰²⁶ bulk of soft collisions can represent an effective veto on hard processes. For the
¹⁰²⁷ nuclear modification factor this would lead to $R_{\text{pPb}} < 1$.

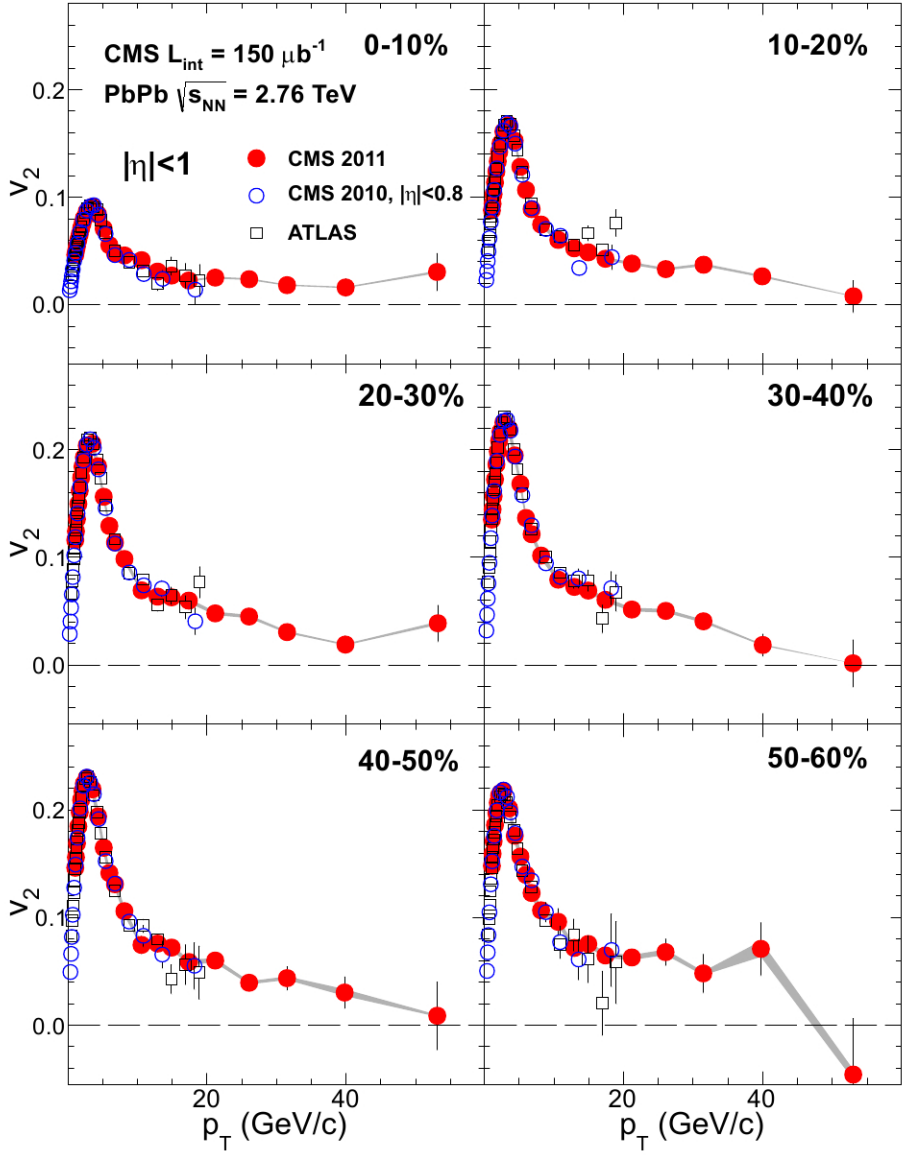


Figure 17: Elliptic flow, v_2 , as a function of the charged particle transverse momentum from 1 to 60 GeV/c with $|\eta| < 1$ for six centrality ranges in Pb-Pb collisions at $\sqrt{s_{NN}} = 2.76 \text{ TeV}$, measured by the CMS experiment. [81].

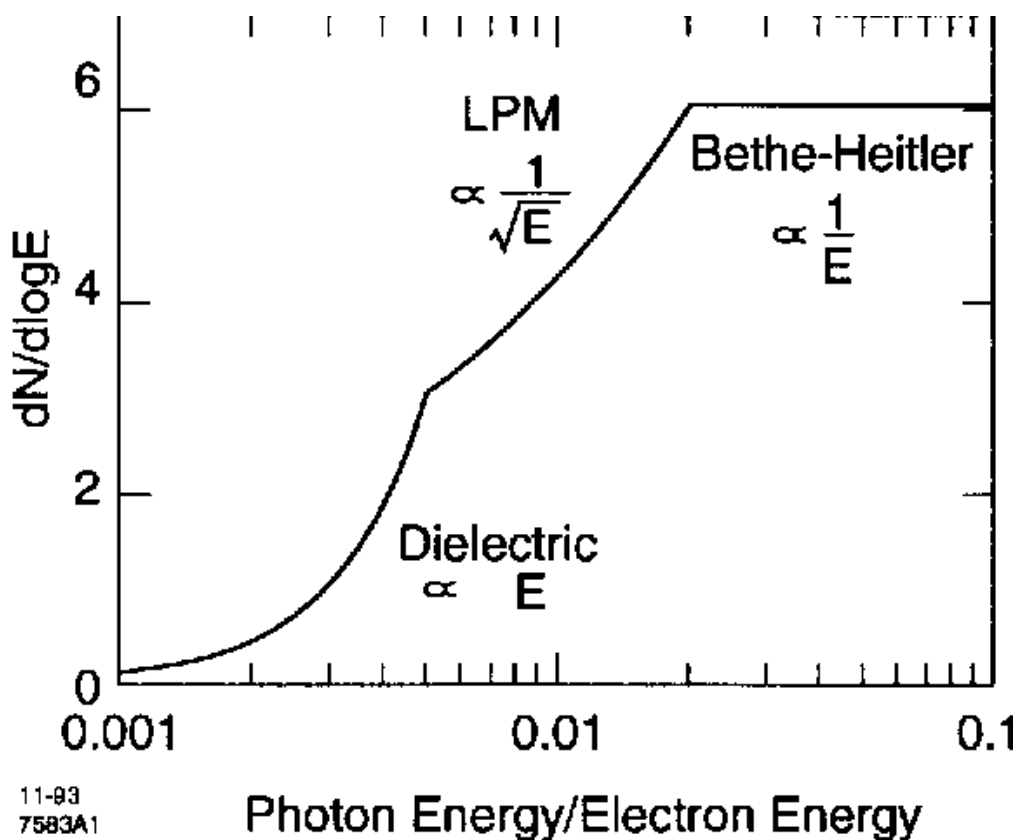


Figure 18: The expected bremsstrahlung spectrum for a electron propagating through material. [86].

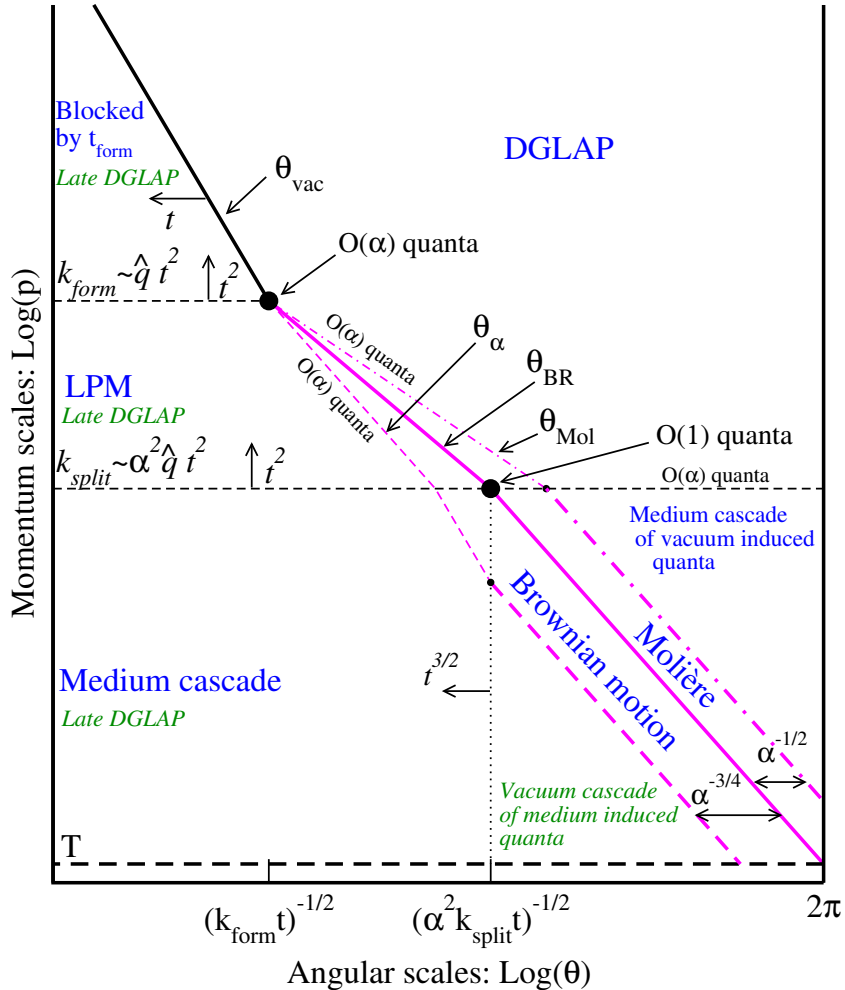


Figure 19: Parametrically accurate picture of how a medium-modified parton cascade fills the phase space. At time t , quanta can be formed up to momentum scale k_{form} and they are formed with $O(1)$ probability per $\log p$ at lower scale k_{split} . Quanta below k_{split} split further and their energy cascades to the thermal scale T in less than an epoch t . Transverse Brownian motion moves quanta up to the angle $\theta_{\text{BR}}(p)$ denoted by the thick purple line. The Molière region at larger θ is dominated by rare large angle scattering. At even larger angle, there are $O(\alpha_s)$ quanta per double logarithmic phase space from DGLAP ‘vacuum’ radiation, and for momenta below k_{split} these cascade within time t to T . After the jet escapes the medium, the jet and the emitted fragments will undergo vacuum radiation. This late time vacuum radiation emitted by the original parton dominates at sufficiently small $\log \theta$ (regions marked “late DGLAP” and bounded by θ_{vac} and θ_α), whereas the late time radiation of the fragments dominates in the region denoted by “Vacuum cascade of the medium induced quanta”. [109].

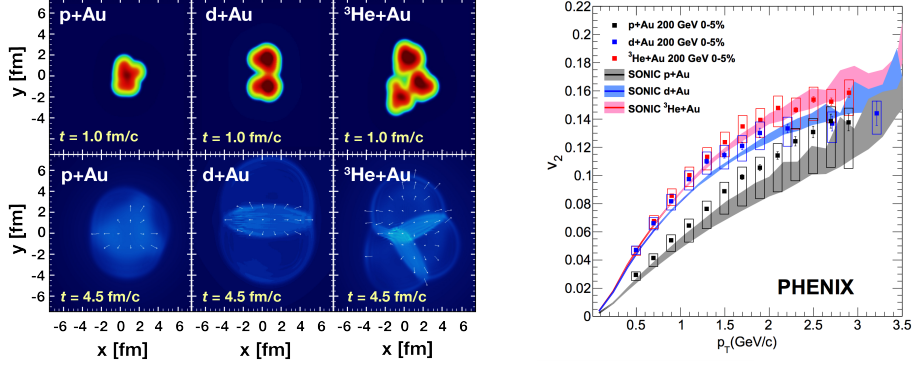


Figure 20: Calculations of the intial energy density in small collision systems at RHIC and the resulting hydrodynamic evolution.

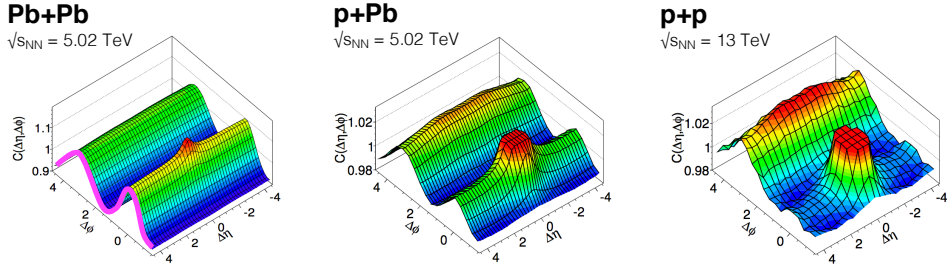


Figure 21: Two-particle correlation results in PbPb, pPb, and pp collisions at the LHC [1].

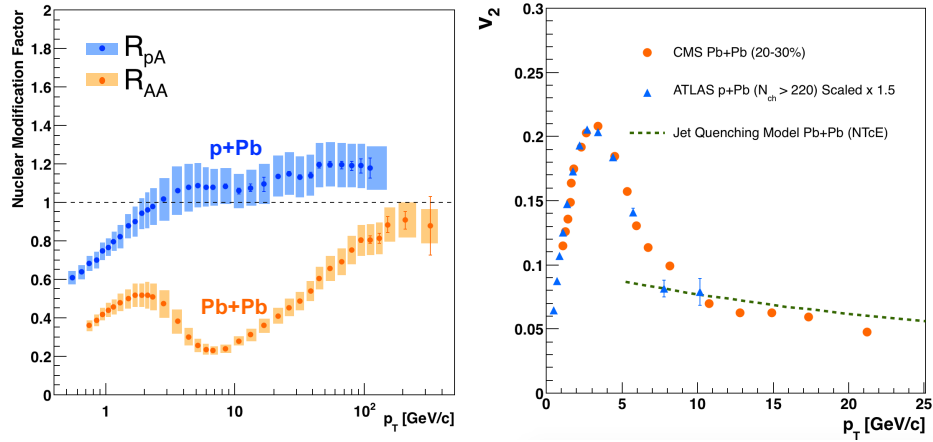


Figure 22: RpA in proton-lead collisions

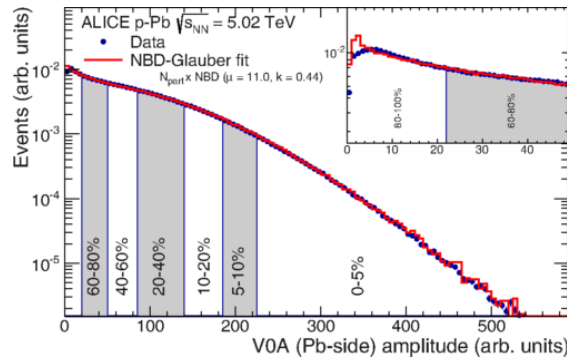


Figure 23: Distribution of the sum of amplitudes in the V0A hodoscopes (Pb-going), as well as the NBD-Glauber fit (explained in the text). Centrality classes are indicated by vertical lines. The inset shows a zoom-in on the most peripheral events. [1]

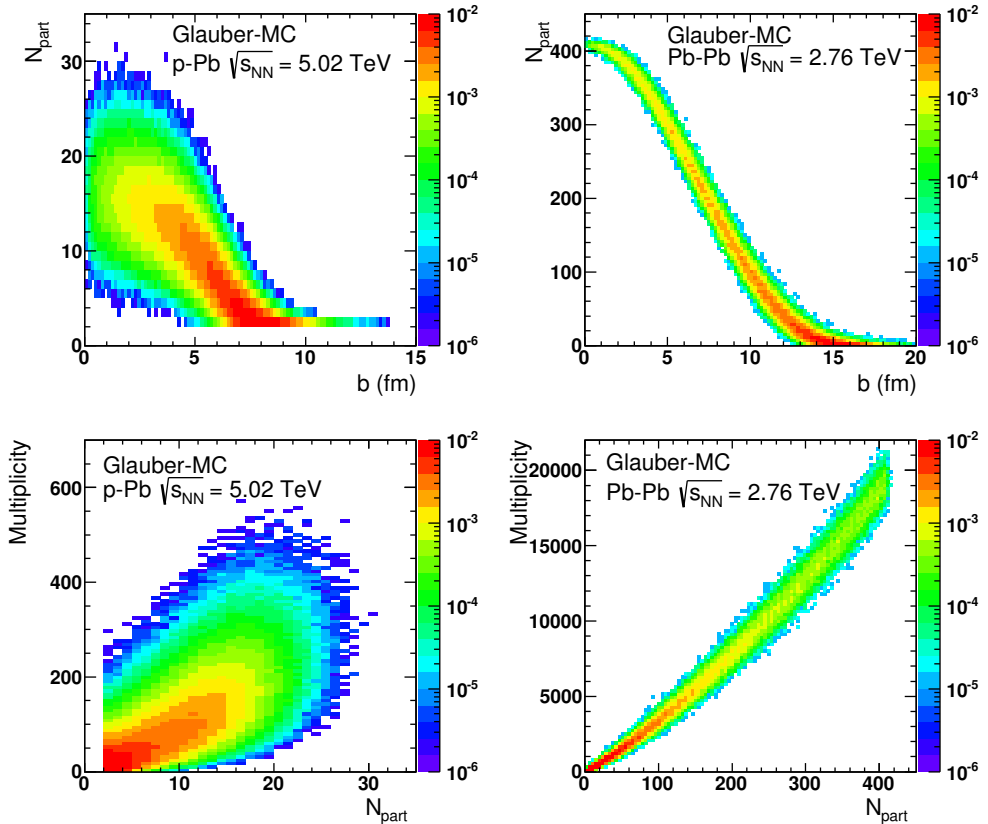


Figure 24: Top: Scatter plot of number of participating nucleons versus impact parameter; Bottom: Scatter plot of multiplicity versus the number of participating nucleons from the Glauber fit for V0A. The quantities are calculated with a Glauber Monte Carlo of p-Pb (left) and Pb-Pb (right) collisions. [1]

1028 2 Experimental Details

1029 2.1 CERN

1030 The European Organization for Nuclear Research (CERN) is the largest particle
1031 physics laboratory in the world. CERN was founded in 1954. In 2019 CERN
1032 consists of 22 member states. Additionally CERN has contacts with a number
1033 of associate member states and various individual institutions. Some 12000 vis-
1034 iting scientists from over 600 institutions in over 70 countries come to CERN for
1035 their research. CERN itself is located near Geneva at the border of France and
1036 Switzerland and itself employs about 2500 people.

1037 The laboratory includes a series of accelerators, which are used to accelerate
1038 the particle beams used. A schematic view of the complex as of 2019 is shown
1039 in Figure 25. In the framework of this thesis the main component is the Large
1040 Hadron Collider (LHC), the largest collider at CERN. LHC will be discussed in
1041 the chapter in more detail. Other accelerators in the series are used to inject the
1042 particle beam into LHC, but they are also used in itself for various experimental
1043 studies.

1044 The second largest accelerator is the super proton synchrotron (SPS). It is final
1045 step before the particle beam is injected into LHC. Commissioned in 1976, it was
1046 the largest accelerator at CERN until the the Large Electron-Positron Collider
1047 (LEP) was finished in 1989. Originally it was used as a proton-antiproton collider
1048 and as such provided the data for the UA1 and UA2 experiments, which resulted in
1049 the discovery of the W and Z bosons. At the moment there are several fixed target
1050 experiments utilising the beam from SPS. These study the structure (COMPASS)
1051 and properties (NA61/SHINE) of hadrons, rare decays of kaons (NA62) and radi-
1052 ation processes in strong electromagnetic fields (NA63). Additionally the AWAKE
1053 and UA9 experiments are used for accelerator research and development.

1054 -PS

1055 2.2 Large Hadron Collider

1056 The Large Hadron Collider (LHC) is the largest accelerator at CERN and the
1057 largest particle collider ever built. The LHC is designed to accelerate protons
1058 up to an energy of 8 TeV and lead ions up to 2.76 TeV per nucleon [127]. The
1059 design luminosity of the LHC is $10^{34} \text{cm}^{-2}\text{s}^{-1}$. In 20xx it achieved a record peak
1060 luminosity of xxx. For lead beams the design luminosity is xxx. All this is achieved
1061 with a ring of 26.7 km, that consists of 1232 superconducting dipole magnets that
1062 keep particles in orbit.

1063 The particles are accelerated through the use of radio-frequency (RF) cavities.
1064 The RF are build such that the electromagnetic waves become resonant and build

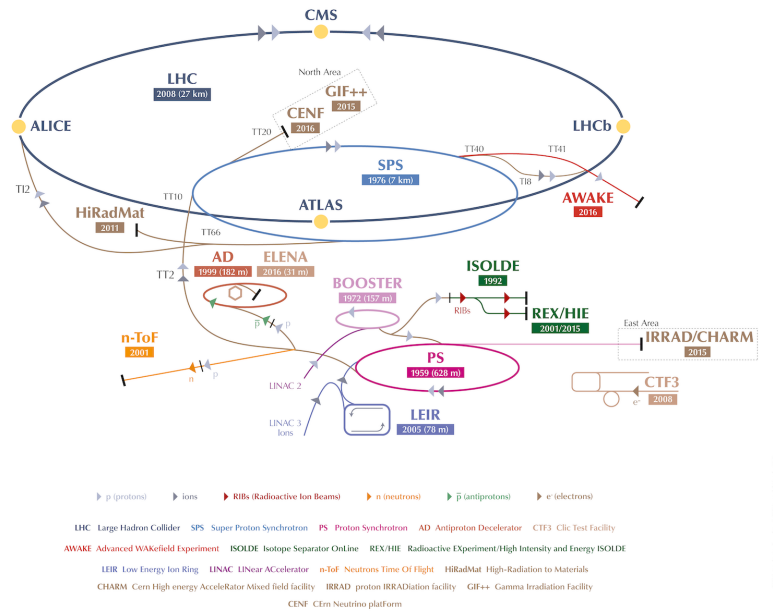


Figure 25: A schematic view of the accelerator complex at CERN. Before particles can be injected into the LHC they require a series of preliminary? acceletarors. Until 2018 protons start their journey in LINAC2 (Linear Accelerator) and continue through the Booster, Proton Synchrotron (PS) and Super Proton Synchrotron (SPS). Between 2019 and 2020 LINAC2 will be replaced by LINAC4 [126]

1065 up inside the cavity. Charges passing through the cavity feel the overall force
1066 and are pushed forward along the accelerator. As they consist of electromagnetic
1067 waves, the field in the RF cavity oscillates. Thus particles must enter the cavity at
1068 the correct phase of oscillation to receive a forward push. When timed correctly,
1069 the particles will feel zero accelerating voltage when they have exactly the correct
1070 energy. Particles with higher energies will be decelerated and particles with lower
1071 energies will be accelerated. This focuses particles in distinct bunches. The RF
1072 oscillation frequency at the LHC is 400.8 MHz. Thus RF "buckets" are separated
1073 by 2.5 ns. However only 10 % are actually filled with particles, so the bunch
1074 spacing in the LHC is 25 ns, at a bunch frequency of 40 MHz.

1075 With 7 TeV proton beams the dipole magnets used to bend the beam must
1076 produce a magnetic field of 8.33 T. This can be only achieved through making
1077 the magnets superconducting, which requires cooling them down with helium to a
1078 temperature of 1.9 K. The 1232 dipole magnets make up roughly 2/3 of the LHC
1079 circumference. The remaining part is made up of RF cavities, various sensors and
1080 higher multipole magnets used to keep the beam focused. The most notable of
1081 these are the 392 quadrupole magnets.

1082 The LHC is divided into octants, where each octant has a distinct function.
1083 Octants 2 and 8 are used to inject beam into the LHC from SPS. The 2 beams
1084 are crossed in octants 1,2,5 and 8. The main experiments are built around these
1085 crossing points. Octants 3 and 7 are used for beam cleansing. This is achieved
1086 through collimators that scatter particles with too high momentum or position
1087 offsets off from the beam. The RF cavities used for acceleration are located in
1088 octant 4 and octant 6 is used for dumping the beam. The beam dump is made
1089 up of two iron septum magnets, one for each beam, that will kick the beam away
1090 from machine components into an absorber when needed.

1091 2.2.1 LHC experiments

1092 As of 2018 there are four main experiments at the LHC; ALICE, ATLAS, CMS
1093 and LHCb and three smaller ones LHCf, TOTEM and MoEDAL. ALICE will be
1094 covered in section 2.3.

1095 ATLAS (A Toroidal LHC ApparatuS) and CMS (Compact Muon Solenoid) are
1096 the two largest experiments at the LHC. They are both multipurpose experiments
1097 designed to be sensitive to many different possible new physics signals. The biggest
1098 discovery made by these so far is the discovery of the Standard Model Higgs boson,
1099 which was simultaneously published by the experiments in 2012 [128, 129].

1100 The LHCb (LHC beauty) experiment [130] is made for studying the bottom
1101 (beauty) quark. Main physics goals include measurement of the parameters of CP
1102 violation with decays of hadron containing the bottom quark. One of the most
1103 important results published by LHCb is the first measurement of $B_s^0 \rightarrow \mu^+\mu^-$

1104 decay, which was found to be in line with the Standard Model.

1105 In addition to the four large experiments there are three smaller experiments
1106 along the LHC ring. LHCf (LHC forward) is located at interaction point 1 with
1107 ATLAS. It aims to simulate cosmic rays by the particles thrown forwards by the
1108 collisions in ATLAS.

1109 TOTEM (TOTal Elastic and diffractive cross section Measurement) is located
1110 near the CMS experiment at point 5. This allows it to measure particles emerging
1111 from CMS with small angles. The main goals is to measure the total, elastic and
1112 inelastic cross-sections in pp collisions [131].

1113 The MoEDAL (Monopole and Exotics Detector At the LHC) experiment is
1114 located at the interaction point 8 together with the LHCb experiment. MoEDAL
1115 tries to measure signatures of hypothetical particles with magnetic charge, mag-
1116 netic monopoles.

1117 2.3 ALICE

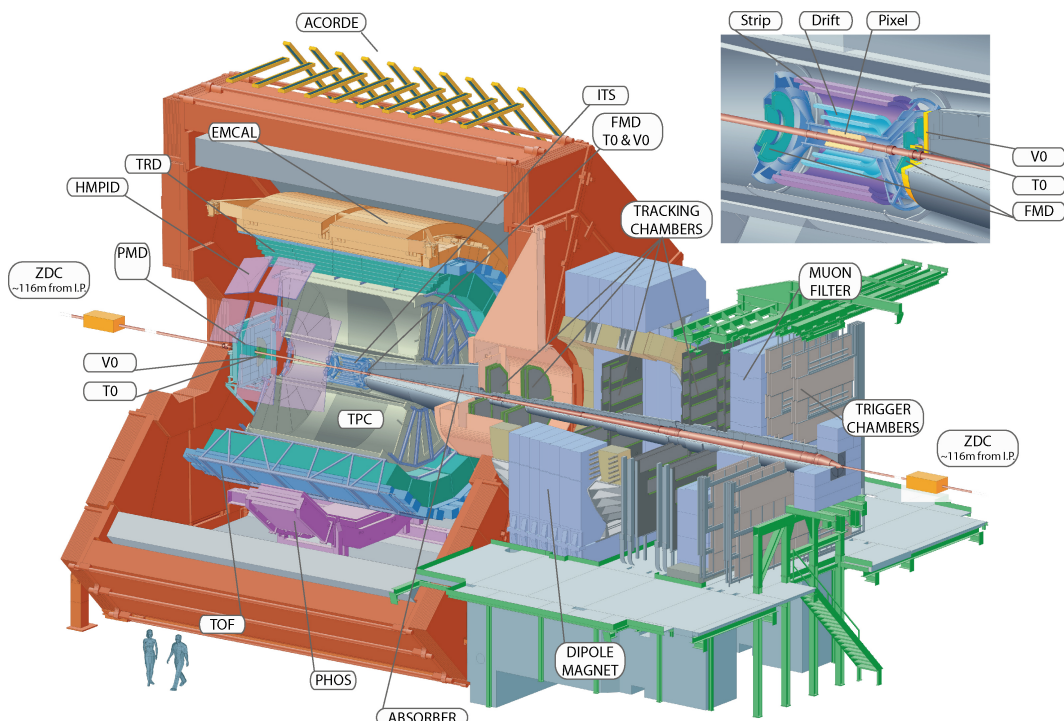


Figure 26: Schematic view of ALICE

1118 ALICE (A Large Ion Collider Experiment) [132] is the dedicated heavy ion
1119 experiment at the LHC. ALICE was designed to cope with the expected very high
1120 multiplicity environment of heavy ion collisions. The design allows measurement

of a large number of low momentum tracks. The different detector subsystems are optimised to provide high momentum resolution and excellent particle identification capabilities over a broad range of momentum.

A schematic view of the ALICE detector in 2018 is presented in Figure 26. This section will go through the composition of ALICE as it has been during run 2 between 2014 and 2018. The detector will go through significant upgrades during Long Shutdown 2 in 2019-2020. As in all the major high energy physics experiments the positioning of the detectors follows a layered structure. Closest to the interaction point are the tracking detectors. The main task of these detectors is to locate the position of the primary interaction vertex accurately and to record the tracks of charged particles. To achieve this they need a very good spatial resolution close to the interaction point. Tracking detectors do not significantly alter the tracks of traversing particles. Thus they can be located in the innermost layers.

Calorimeters are designed to stop any particles hitting them and use the absorption to measure the energy of the particles. Thus they must be located behind the tracking detectors. ALICE has two separate calorimeter systems, the electromagnetic calorimeters measure mainly electrons and photons, while the muon detection system measures muons.

2.3.1 Tracking

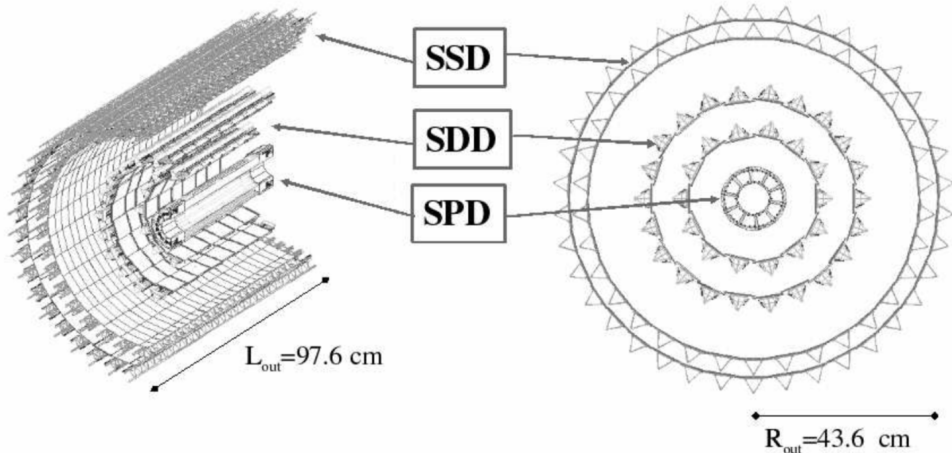


Figure 27: Schematic view of ALICE Inner Tracking System

The main design guideline for the tracking detectors in ALICE was the requirement to have good track separation and high granularity in the high multiplicity environment of heavy ion collisions. Before LHC was built the wildest estimates

1144 put the particle density at 8000 charged particles per unit of rapidity]]. In reality
1145 the particle density turned out to be significantly smaller, about 1600 charged
1146 particles per rapidity unit.]]

1147 The main tracking detector in ALICE is the Time Projection Chamber (TPC) [133],
1148 discussed in more detail in section 2.3.2

1149 Between TPC and the beam pipe there is an array of six layers of silicon
1150 detectors, called the inner tracking system (ITS) [134]. The main tasks of the
1151 ITS are to locate the primary vertex with a resolution better than $100\ \mu m$, to
1152 reconstruct the secondary vertices from decaying particles, to track and identify
1153 particles with momenta below 200 MeV and to compliment the momentum and
1154 angle measurements of TPC. During long shutdown 2 in 2019-2020 the entire ITS
1155 will be replaced [135]. As of 2018 the two innermost layers are made of the silicon
1156 pixel detector (SPD). As it's the closest detector to the interaction point it requires
1157 are very high spatial resolution. Thus the choice of pixel technology is natural. In
1158 heavy ion collisions the particle density is around 50 particles per cm^2 .

1159 The next two layers are the silicon drift detector (SDD), which is made out of
1160 homogeneous neutron transmutation doped silicon. It is ionized when a charged
1161 particle goes through the material. The generated charge then drifts to the col-
1162 lection anodes, where it is measured. The maximum drift time in SDD is about 5
1163 μs . This design gives very good multitrack capabilities and provides two out of the
1164 four dE/dx samples in the ITS.

1165 The two remaining layers in the ITS are the silicon strip detector (SSD). The
1166 strips work in a similar way as silicon pixels, but by itself one layer only provides
1167 good resolution in one direction. Combining two crossing grids of strips provides 2
1168 dimensional detection. Each charged particle will hit two intervening strips. The
1169 position of the hit can be deduced from the place where the strips cross each other.

1170 2.3.2 TPC

1171 Time projection chamber (TPC) is a cylindrical detector filled with $88\ m^3$ of
1172 Ne – CO₂ (90/10 %) gas mixture. The gas is contained in a field cage that provides
1173 an uniform electric field of $400V/cm$ along the z-axis (along the beam direction).
1174 Charged particles traversing through the TPC volume will ionise the gas along
1175 their path. This liberates electors that drift towards the end plates of the cylin-
1176 der.

1177 The field cage is separated into two detection volumes by the central high
1178 voltage electrode. Both sides have a drift length of 2.5 m and inner/outer diameters
1179 of 1.2/5 m. This means the central electrode must provide a maximum potential
1180 of 100 kV to achieve the design field magnitude. The maximum time required for
1181 electrons to drift through the chamber is about $90\ \mu s$.

1182 When electrons reach the end of the main cylinder they enter the readout

chambers. The readout section of both sides consists of 18 outer chambers and 18 inner chambers. Each of them are made of multiwire proportional chambers with cathode pad readout. This design is used in many TPCs before. During Long Shutdown 2 in 2019-2020, the multiwire chambers will be replaced by Gas Electron Multipliers (GEMs, see section 2.3.3).

The relatively slow drift time of $90 \mu\text{s}$ is the limiting factor for the luminosity ALICE can take. The occupancy of the TPC must be kept in a manageable level.

2.3.3 TPC upgrade

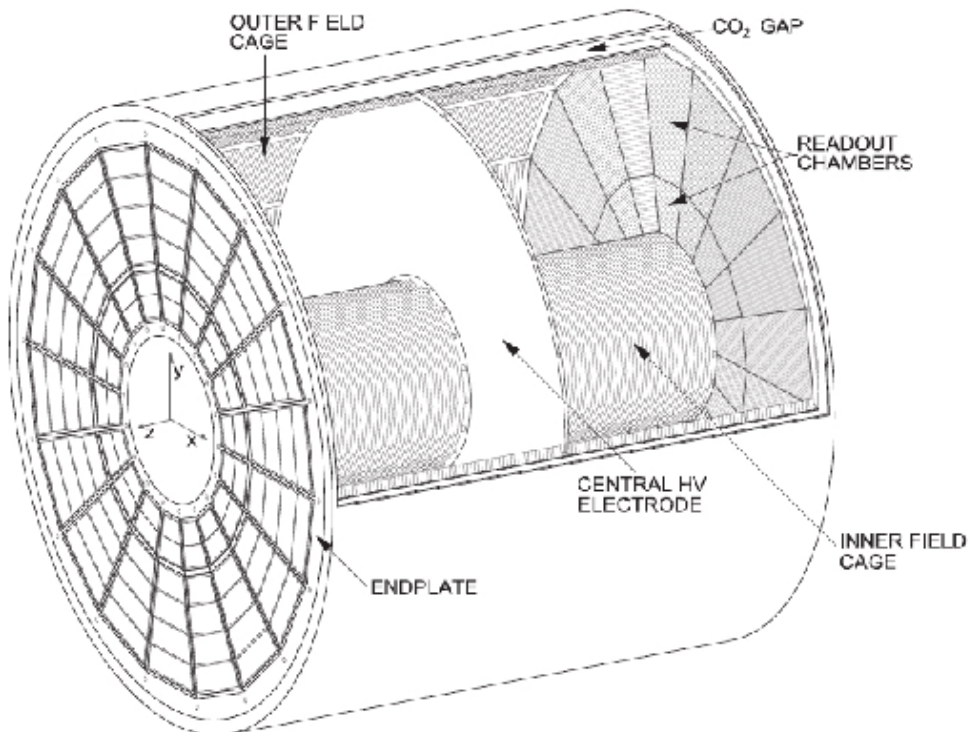


Figure 28: Schematic view of ALICE Time Projection Chamber

During long shutdown 2 in 2019-2020 ALICE will go through significant modifications. The goal is to be able have continuous readout [136] in heavy ion collisions at an interaction rate of 50 kHz. I have made a personal contribution to the quality assurance of the new GEM readout of TPC.

ALICE will add a new Forward Interaction trigger (FIT) to replace the V0 and T0 detectors.

1197 Additionally the current inner tracking system (ITS) will be completely re-
1198 placed. The current layered structure with three different technologies will be
1199 replaced by an all pixel detector with significantly reduced pixel size. Additionally
1200 the first layer will be brought closer to the beam pipe. The new ITS will have
1201 better tracking efficiency and better impact parameter resolution.

1202 The muon detection will be complimented by the Muon Forward Tracker (MFT) [137].
1203 Based on the same technology as the new ITS, MFT will be placed before the
1204 hadron absorber that sits in front of the existing muon spectrometer. MFT should
1205 significantly increase the signal/background ratio in heavy quark measurements.

1206 Many subdetectors will make small improvements to enhance the readout rate.
1207 The central trigger processor will be replaced and ALICE will introduce a new
1208 framework O^2 that combines both online data acquisition and offline analysis.

1209 The detector restricting the readout the most at the moment is the TPC. The
1210 current wire chamber based system limits the readout rate to 3.5 kHz. To achieve
1211 the 50 kHz readout rate goal the wire chambers will be replaced by a Gas Electron
1212 Multiplier (GEM) based system.

1213 TPC has a total of 36 inner and 36 outer readout chambers. Each of these will
1214 consist of 4 layers of GEM foils. The inner chambers will only have one foil for
1215 each layer. The outer chambers are separated into three sections, each with its
1216 own layer of foils. Each gem foil is made up of a 50 μm thick resistive capton layer,
1217 coated on both sides by 5 μm thick layers of copper. Each foils is separated into a
1218 number (20-24) of distinct active areas. The active areas are pierced quite densely,
1219 they have 50-100 holes in the area of a single mm^2 . The density of holes changes
1220 from layer to layer. The two middle layers of foils have a larger (double) pitch
1221 (smaller hole density) while the top and bottom layers have a smaller (normal)
1222 pitch (larger hole density).

1223 The holes have a conical shape which they acquire during a two step chemical
1224 etching process.

1225 The working principle of these foils is based on electrodynamics. **elaborate** There
1226 is a large potential difference (140-400 V) applied to the two sides of the foil, which
1227 results in large field in each hole. This acts both as a lens and an amplifier for
1228 the electrons. The amplification happens inside the holes where the field is the
1229 strongest.

1230 As opposed to wire chambers, which typically have one voltage setting, a GEM-
1231 based detector requires several independent voltage settings: there is a drift voltage
1232 which drives the electrons from the ionisation point to the GEM, an amplification
1233 voltage, and an extraction voltage that brings electrons from the GEM exit to the
1234 readout plane.

1235 The GEMs are designed to minimise ion backflow to allow continuous, ungated
1236 and untriggered readout.

1237 The purpose of the multilayered structure is to reduce the ion backflow []; not
1238 only one layer of GEM foils will be installed, but a 4 layer stack. In the stack there
1239 are 2 standard pitch GEM foils, where the pitch size, i.e. the separation of the
1240 holes inside a foil is around $140 \mu\text{m}$, and 2 large pitch GEM foils, there the hole
1241 spacing is two times larger, $280 \mu\text{m}$. The two outer layers will have standard pitch
1242 and the two middle layers have large pitch. The middle layers with large pitch
1243 serve as extra insulator against the ion backflow. Additionally the setup allows
1244 operating individual GEM foils at lower voltages and still have an increase in the
1245 gain of a few orders of magnitude. [138]

1246 Quality Assurance of the GEM foils

1247 The GEM foils are produced at CERN, where they will undergo a basic QA (QA-B)
1248 procedure, that includes a coarse optical inspection to remove any clear defects
1249 and a short term high voltage measurement. Afterwards the advanced quality
1250 assurance (QA-A) is performed in two centers, one in the Helsinki Institute of
1251 Physics (HIP) and one in the Wigner Research Centre in Budapest. Details of the
1252 QA-A procedure can be found in the thesis of Márton Vargyas [139]. In the QA-A
1253 centers all foils are put through a detailed optical scanning process and a long
1254 term high voltage measurement. I was personally performing the QA production
1255 in Helsinki for the last 6 months of the project.

1256 The optical scan is performed with the help of a scanning robot. The setup
1257 along with most of the software was developed at the Detector Laboratory of the
1258 Helsinki Institute of Physics []. The purpose of the scan is two-fold; to catch
1259 defects that could affect the performance and classify the foils based on their
1260 hole parameters. It is expected that these are connected with the foil's electric
1261 properties []. For example, smaller holes create more intense and focused fields,
1262 which would result in larger amplification of their avalanche electrons, i.e. the
1263 local gain is expected to be larger.

1264 After the optical scanning, the foils are subjected to a long term (5-12 hours)
1265 high voltage leakage current measurement. Each segment of the GEM foil is con-
1266 nected to a high voltage and the leakage current is measured separately for each
1267 segment, by the connected picoamper-meter (pA-meter). The accepted leakage
1268 current in each segment is 0.16nA , foils with larger values are discarded.

1269 2.3.4 Particle identification

1270 One guiding principle in the design of ALICE was to achieve good particle iden-
1271 tification (PID) over a large part of phases space and for several different particle
1272 types. In ALICE there are several detectors taking part in the identification of
1273 particles.

1274 One of the particle identification detectors is the transition radiation detector
1275 (TRD) [140]. Its main task is identifying electors with momenta larger than 1 GeV.
1276 Transition radiation is produced when highly relativistic particles traverse the
1277 boundary between two media having different dielectric constants. The average
1278 energy of the emitted photon is approximately proportional to the Lorentz factor γ
1279 of the particle, which provides an excellent way of discriminating between electrons
1280 and pion. ALICE TRD is made of a composite layer of foam and fibres. The
1281 emitted photons are then measured in six layers of Xe/CO₂ filled time expansion
1282 wire chambers.

1283 The time of flight (TOF) detector [141] uses a very simple physics principle,
1284 i.e. calculating the velocity of the particle using the time of flight between two
1285 points. Combining this with the momentum of particle, obtained from the tracking
1286 detectors, one can calculate the mass of the particle, which identifies particles. The
1287 TOF detector consists of multigap resistive wire chambers. These are stacks of
1288 resistive plates spaced equally. They allow time of flight measurements in large
1289 acceptance with high efficiency and with a resolution better than 100 ps.

1290 The third specific particle identification detector is the high momentum particle
1291 identification (HMPID) detector [142]. The HMPID uses a ring imaging Cherenkov
1292 counter to identify particles with momenta larger than 1 GeV. Particles moving
1293 through a material faster than the speed of light in the material will produce
1294 Cherenkov radiation. The velocity of the particle determines the angle at which
1295 the radiation is emitted. Measuring this angle gives the velocity of the particle.
1296 This can be again used to calculate the mass of the particle, if the momentum is
1297 known. In HMPID the material is a liquid radiator and the photons are measured
1298 with multiwire proportional chambers in conjunction with photocathodes.

1299 In addition to the specific particle identification detectors, the general purpose
1300 tracking detectors can be used for identification through the use of specific energy
1301 loss of charged particles traversing through a medium and the transition radiation
1302 emitted by charged particles when crossing the boundary between two materials.

1303 dE/dx measurements are provided by the last four layers of the ITS detector, i.e.
1304 the SDD and the SSD, thanks to their analog readout. [143] ITS provides particle
1305 identification in the low p_T region, up to 1 GeV, and pions reconstructed in the
1306 standalone mode can be identified down to 100 MeV. Similar to ITS the TPC
1307 detector provides specific energy loss measurements. TPC can identify charged
1308 hadrons up to p_T 1 – 2 GeV as well as light nuclei, He3 and He4.

1309 2.3.5 Electromagnetic Calorimeter

1310 Calorimeters are designed to measure the energy of particles. Electromagnetic
1311 calorimeters specialise in detecting particles that interact primarily through the
1312 electromagnetic interaction, namely photons and electrons. They are required in

1313 many neutral meson and direct photon analyses. In addition the energy information
1314 enhance jet measurements.

1315 ALICE has two electromagnetic calorimeters, the photon spectrometer (PHOS) [144]
1316 and the electromagnetic calorimeter (EMCal) [145]. PHOS is a homogeneous
1317 calorimeter that consists of scintillating PbWO₄ crystals, which generate a bremsstrahlung
1318 shower and produce scintillation light. The energy of the particle determines the
1319 amount of light produced. To improve the charged particle rejection, PHOS in-
1320 cludes a charged particle veto detector (CPV) [?]. PHOS is built to have a very
1321 fine granularity, making it well suited for measuring direct photons and neutral
1322 mesons.

1323 EMcal is segmented into 10 full size super modules (SM), 5 for A side and 5 for
1324 C side, and two 1/3 sized SMs, one for each side. This segmentation can be seen
1325 in Fig. 29. Each SM is divided into 24 strips, each covering full η (24 towers) and
1326 2 towers in η . Each strip is composed of 2×2 tower modules. Thus each full size
1327 super module includes 1152 towers and in total the EMCal is made up of 12288
1328 towers.

1329 The build of individual towers is shown in Fig. 30. Each tower is built up from
1330 76 alternating layers of 1.44 mm Pb and 77 layers of 1.76 mm polystyrene base
1331 injection moulded scintillator. The lead tiles produce the shower and scintillator
1332 tiles the light. Each tower scintillator is equipped with reflectors on all sides
1333 to provide better gain and keep the four towers inside one module isolated. The
1334 scintillation photons produced in the active volume of the tower are collected by 36
1335 longitudinally placed wave length shifting light guide fibers. The light is eventually
1336 directed to the Avalanche Photo Diodes (APD) for readout.

1337 The acceptance of EMCal in the azimuthal angle is $80 \text{ deg} < \phi < 187 \text{ deg}$. Dur-
1338 ing long shutdown 1 in 2013-2015, EMCal was extended with the di-jet calorimeter
1339 (DCal) [146], giving an additional acceptance region of $260 \text{ deg} < \phi < 320 \text{ deg}$.
1340 This provides partial back-to-back coverage. In comparison to PHOS, EMCal has
1341 coarser granularity, but a significantly larger acceptance, making it suitable for jet
1342 physics.

1343 2.3.6 Forward detectors

1344 ALICE includes a few small and specialised detectors of importance. The event
1345 time is determined with very good precision ($< 25 \text{ ns}$) by the T0 detector [147].
1346 T0 consists of two sets of Cherenkov counters that are mounted around the beam
1347 pipe on both sides of the interaction point. T0 gives the luminosity measurement
1348 in ALICE.

1349 Another small detector in the forward direction is the V0 detector [147]. This
1350 consists of two arrays of segmented scintillator counters located at $-3.7 < \eta <$
1351 -1.7 and $2.8 < \eta < 5.1$. V0 is used as a minimum bias trigger and for rejection

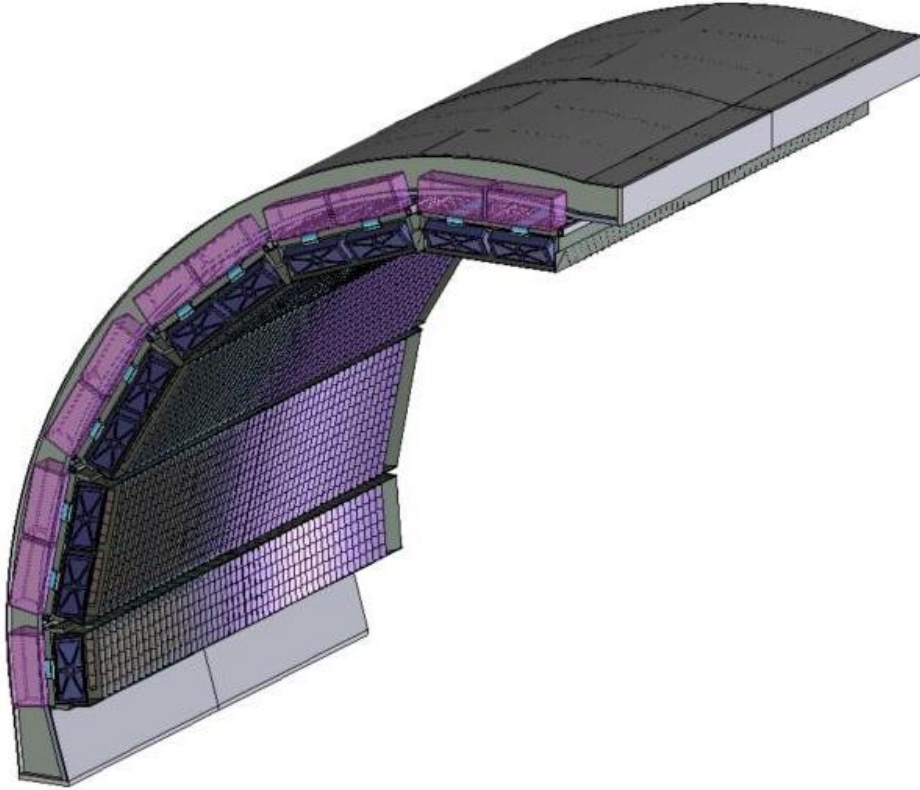


Figure 29: The EMCal detector arc, where the segmentation into 10 full size and 2 $\frac{1}{3}$ -sized (5 and 1 per side) supermodules can be seen.

of beam-gas background. Particle multiplicity in the forward direction can be related to the event centrality. Thus V0 is the main detector used in centrality determination in PbPb collisions.

The multiplicity measurement of V0 is complimented by the forward multiplicity detector (FMD) [147]. FMD includes five rings of silicon strip detectors that make up the FMD. FMD gives acceptance in the range $-3.4 < \eta < -1.7$ and $1.7 < \eta < 5.0$.

During long shutdown 2 in 2019-2020, V0 and T0 will be replaced by the Fast Interaction Trigger (FIT) detector [148]. For historical reasons elements of FIT are also referred to as V0+ and T0+. FIT will allow centrality, event plane, luminosity and interaction time determination in the continuous readout mode, that ALICE will operate in after 2020.

For photon multiplicity measurement ALICE has the photon multiplicity detector (PMD) [149]. PMD uses two planes of gas proportional counters with a cellular honeycomb structure. PMD gives the multiplicity and spatial distribution

THE EMCAL Module Components

Containment: 88 parts

- 1) Back (holes: 144 thru for fibers + springs + mech. support), 1
- 2) Compression (holes: 144 thru for fibers + springs), 1
- 3) Front Plate (holes: 144 thru for fibers + springs + mech. support), 1
- 4) 5) Plungers (10)
- 6) Belleville washers (75)

Tensioning and Insulation:

40 parts

- 7) Stainless steel straps (4)
- 8) Screws (24)
- 9) Flanges (8)
- 10) Light tight stickers (4)

Sandwich:

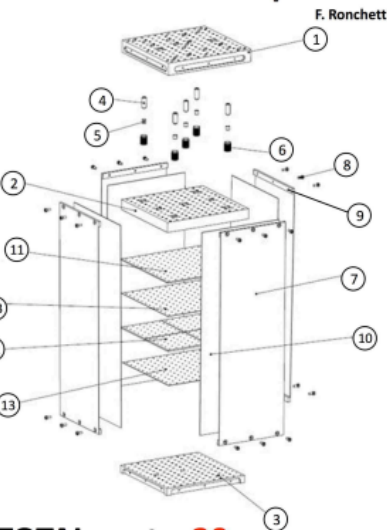
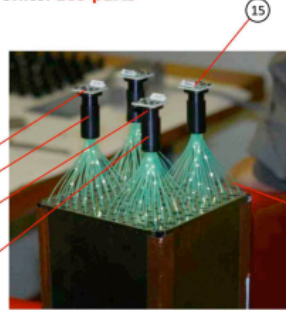
538 parts

- 11) Lead tiles (76)
- 12) Scintillator tiles (308)
- 13) Bond paper sheets (154)

Readout and Electronics:

165 parts

- 14) WLS fibers (144)
- 15) APD (4)
- 16) CSP (4)
- 17) Light guides (4)
- 18) Mount (4)
- 19) Collars (4)
- 20) Diffuser (1)



TOTAL parts: 20

TOTAL components: 831

Plus cabling, GMS and mech. supports

Figure 30: The exploded EMCAL tower view

of photons in the region $2.3 < \eta < 3.7$.

On top of the ALICE magnet there is an array of 60 large scintillators called the ALICE cosmic ray detector (ACORDE) [150]. ACORDE is used as a trigger for cosmic rays for calibration and alignment.

The only hadronic calorimeters in ALICE are the zero degree calorimeters (ZDC) [151], which are located next to the beam pipe in the machine tunnel about 116 m from the interaction point. There are two sets of calorimeters. One is made of tungsten, specialising in measuring neutrons, while the other, made of brass, is specialised in measuring protons. In heavy ion and especially in proton-lead collisions, ZDC gives information about the centrality of the event. ZDC is meant to detect spectators, i.e. parts of the colliding ions that do not take part in the interaction. If there are more spectators, the collisions is likely to be more peripheral.

A new detector installed during the long shutdown 1 is the ALICE diffractive detector (AD) [?]. AD consists of two assemblies, one in each side of the interaction point, both made of two layers of scintillators. These assemblies are situated about 17 m and 19.5 m away from the interaction points. The pseudorapidity coverage is $-6.96 < \eta < -4.92$ and $4.78 < \eta < 6.31$. AD greatly enhances ALICE's capability

1385 for diffractive physics measurements that require a large pseudorapidity gap.

1386 2.3.7 Muon spectrometer

1387 Outside the main magnet, ALICE has a spectrometer dedicated to measuring
1388 muons [152]. In heavy ion physics muons are mainly used to measure the produc-
1389 tion of the heavy quark resonances J/ψ , Ψ' , Υ , Υ' and Υ'' .

1390 The muon spectrometer consists of three parts, the absorber, the muon tracker
1391 and the muon trigger. The absorber is meant to remove the hadronic background
1392 as efficiently as possible. After the absorber there are ten plates of thin cathode
1393 strip tracking stations with high granularity, the muon tracker. After the muon
1394 tracker there is a layer of iron to filter out any remaining particles, other than
1395 muons. The muon trigger is located behind this layer. The trigger consists of four
1396 resistive plate chambers.

1397 2.3.8 Trigger

1398 High energy physics experiments need triggers to select interesting physics. Ex-
1399 periments such as CMS and ATLAS at CERN look for extremely rare events with
1400 up to 40 million events each second. Such amounts can't be recorded real-time as
1401 many detectors require some time for the readout, up to 1 ms/event in ALICE.
1402 Thus one uses triggers, i.e. a set of very fast hardware based decisions on which
1403 events are to be saved. Additionally one needs some confirmation that an event
1404 has even occurred.

1405 For ALICE the target event rates are 1 MHz for ppcollisions, 0.1-2 kHz for
1406 Pb-Pbcollisions and 200 kHz for the 2013 p-Pbcollisions.

1407 At ALICE the main system responsible for the trigger decisions is the AL-
1408 ICE Central Trigger Processor (CTP) [?]. The CTP generates three levels of
1409 hierarchical hardware triggers - Level 0, Level 1 and Level 2, (L0, L1 and L2 re-
1410 spectively) before an event is accepted and transmitted to the Data Acquisition
1411 system (DAQ). Afterwards additional software assessments are performed by the
1412 High Level Trigger (HLT).

1413 Triggers can roughly put into two classes, minimum bias triggers that make sure
1414 no empty events are recorded, and rare triggers that require specific signatures in
1415 ALICE detectors, such as large energy deposits in EMCAL or two muons in the
1416 muon arm acceptance.

1417 Minimum bias trigger

1418 Several of the ALICE detectors are used to make the initial minimum bias trigger
1419 decisions. These include the SPD layers of ITS, V0 and T0. SPD can count the

1420 number of hits in the first two layers of ITS. Minimum bias ppcollisions typically
1421 require at least one hit in either SPD or V0A/V0C

1422 Similarly Pb–Pbtriggers looks at both V0 and SPD hits. The p–Pbdata has
1423 been mainly triggered using V0 information.

1424 EMCal trigger

1425 In addition to the minimum bias triggers, the most relevant trigger for this thesis
1426 is the EMCAL trigger. Much of the EMCAL trigger has been developed at the
1427 University of Jyväskylä. Extensive details of the trigger and the development
1428 work can be found in the thesis of Jiří Král [153]. Personally I have spent time at
1429 CERN helping in the maintenance of the level 0 trigger.

1430 ALICE EMCAL provides two levels of trigger signal, L0 and L1, which allows
1431 triggering on either single shower deposits or integrated energy deposits in larger
1432 ares, i.e. jets [154].

1433 As inputs the trigger gets exclusive sets of 2×2 EMCAL towers, to limit the
1434 number of channels that need to be processed. The L0 trigger then checks for
1435 energy deposits within a rolling window of 2×2 trigger channels (4×4 towers).
1436 Areas of 4×4 towers most probably will contain only a single shower (or two
1437 adjacent showers coming from a single decayed π^0). Thus the trigger can be called
1438 the single shower trigger.

1439 For L0 the trigger decision is done in Trigger Region Units (TRU) that each
1440 cover 4×42 channels (8×48 towers). The amplitude from the sliding window
1441 is compared to a constant threshold. Additionally a peak finding algorithm is
1442 implemented to define correctly the time of the signal maximum. A single bit OR
1443 decision of all individual TRUs is forwarded to the CTP as the EMCAL L0 trigger
1444 decision.

1445 The L0 information is additionally forwarded to the Level 1 trigger, which
1446 recomputes similar 2×2 channel decisions to produce the single shower trigger,
1447 but L1 can perform the calculation also on the borders between trigger units. In
1448 addition the L1 trigger can check for energy deposits inside a larger 16×16 channel
1449 (32×32 towers) window, which is considered to be the jet trigger.

1450 The L1 trigger can compare up to two thresholds for each single shower and
1451 jet trigger. There is a dedicated link in between the V0 detector and EMCAL STU,
1452 which can provide centrality information, used to compute a dynamical threshold
1453 as a function of the V0 multiplicity.

1454 The trigger subsystem provides both the L0 and L1 decisions to the CTP and
1455 DAQ.

3 Event and track selection

The $\sqrt{s_{\text{NN}}} = 5.02$ TeV p–Pb ($1.3 \cdot 10^8$ events, $\mathcal{L}_{\text{int}} = 620 \text{ nb}^{-1}$) collisions were recorded in 2013 by the ALICE detector [155]. The details of the performance of the ALICE detector during LHC Run 1 (2009–2013) are presented in Ref. [156].

3.1 Event selection

This analysis uses both a minimum bias trigger and an EMCal based trigger to select the analysed events. For the 2013 p–Pb collisions minimum bias events are required to have signals in both V0A and V0C. This condition is used later offline to reduce the contamination of the data sample from beam-gas events by using the timing difference of the signal between the two stations [156].

EMCal is also used to provide the jet trigger used in triggered datasets. EMCal can be used to trigger on single shower deposits or energy deposits integrated over a larger area. Latter case is used for jet triggers. The EMCal trigger definition in the 2013 p–Pb collisions requires an energy deposit of either 10 GeV for the low threshold trigger or 20 GeV for the high threshold trigger in a 32×32 patch size.

The EMCal

Triggers, V0 and EMCal are discussed in more detail in sections 2.3.6, 2.3.8 and 2.3.5.

3.2 Track selection

track reconstruction The analysis uses charged tracks that are reconstructed with the Inner Tracking System (ITS) [157] and the Time Projection Chamber (TPC) [158]. These are discussed in sections 2.3.1 and 2.3.2. A detailed overview of track reconstruction in ALICE can be found from [156].

The main reconstruction of tracks starts in TPC. There are 159 tangential pad rows in the TPC readout chambers. The track reconstruction starts from the outermost layer and the clusters are paired with clusters in the next layer inwards, taking into account a proximity cut. When this track finding procedure hits the innermost pad row in TPC, this information is used as an initial seed for the track finding in ITS. Similar procedure of pairing adjacent layers with a proximity cut is repeated in ITS.

After the reconstruction of tracks in ITS is completed, all the tracks are extrapolated to their point of closest approach to the preliminary interaction vertex. Then the second track fitting step begins, this time starting from the interaction point and proceeding outwards. A Kalman filter [159] technique is used to do the new fit using the clusters found in the previous stage. This time the tracks are matched also to the other detectors in the central barrel beyond TPC. When

1492 this step is complete, a final refit from the outermost TPC pad rows towards the
1493 interaction point is performed. The final track parameters come from this refit.

1494 With the final track parameters the primary vertex can be determined with
1495 better accuracy than with only SPD information. The tracks are extrapolated to
1496 the nominal beam line and a weighted average of the points of closest approach
1497 determines the accurate primary vertex position.

1498 The final step of the track reconstruction is the determination of the secondary
1499 vertices. For this, all the tracks whose distance of closest approach (DCA) to
1500 the primary vertex is larger than a defined minimum value (?? mm in p-Pb) are
1501 selected. For these tracks, points of closest approaches are determined for pairs of
1502 tracks. If the tracks are sufficiently close to each other and show characteristics of
1503 short lived particle decays, these points are identified as secondary vertices.

1504 Combining the information from the ITS and the TPC provides a resolution
1505 ranging from 1 to 10 % for charged particles with momenta from 0.15 to 100 GeV/c.
1506 For tracks without the ITS information, the momentum resolution is comparable
1507 to that of ITS+TPC tracks below transverse momentum $p_T = 10$ GeV/c, but for
1508 higher momenta the resolution reaches 20 % at $p_T = 50$ GeV/c [156, 160].

1509 In p-Pb collisions the tracks are selected following the hybrid approach [161]
1510 which ensures a uniform distribution of tracks as a function of azimuthal angle
1511 (φ). The parameters in the approach are summarised in table 2.

1512 The first requirements are on the quality of the track fit in ITS and TPC.
1513 The ITS requirement only removes tracks that are clear outliers. For TPC the
1514 requirement is much more strict. For step 1 it is required that a track has 3 out of
1515 the 6 possible hits in ITS, one of which must be in SPD. In step 2 this is replaced
1516 by an additional vertex constraint, where the primary vertex itself is added as a
1517 point to the track to improve the momentum resolution.

1518 For the TPC, 70 crossed pad rows out of the maximum 159 is required. This
1519 measures the effective track length inside the TPC. This takes into account the
1520 possibility of having pad rows missing in the middle of the track due to charge in
1521 these clusters being below the threshold for some reason. Additionally it is required
1522 that the ratio between crossed rows and findable clusters is at least 0.8. Findable
1523 clusters are defined as the number of geometrically possible clusters which can be
1524 assigned to a track, taking into account dead zones due to chamber boundaries
1525 and limited η -acceptance. For both steps of the hybrid cut is is required that the
1526 fraction of clusters shared with several tracks is less than 40%.

1527 The remaining cuts are meant to make sure that the measured tracks are
1528 really produced in the primary collision. A track might gain a kink due to a
1529 particle scattering decay. After this, it is no longer describing the properties of the
1530 primary collisions. The particle after such a kink, a kink daughter, is rejected in
1531 the cuts. The final cuts are on the distance of closest approach (DCA) of the track

Table 2: Parameters in the hybrid track cut

Track Cut	Step 1	Step 2
χ^2 / ITS cluster	< 36	< 36
χ^2 / ITS cluster	< 4	< 4
Hits in ITS	3	0
ITS hit requirements	1 in SPD	No requirement
Vertex constraint	No	Yes
Number of crossed rows in TPC	70	70
TPC crossed rows over findable clusters	> 0.8	> 0.8
Fraction of shared TPC clusters	< 0.4	< 0.4
Kink daughters	Rejected	Rejected
DCA _{xy}	< 3.2 cm	< 3.2 cm
DCA _z	< 2.4 cm	< 2.4 cm
Other		Rejected by step 1

1532 to primary vertex. To have confidence that the track comes from the primary
 1533 collision, the track must be close enough to the primary vertex. The cuts are
 1534 different for the distance along (DCA_z) and perpendicular to (DCA_{xy}) the beam
 1535 axis.

1536 The momentum resolutions of the two classes of particles are comparable up
 1537 to $p_T \approx 10 \text{ GeV}/c$, but after that, tracks without ITS requirements have a worse
 1538 resolution [156, 160].

1539 3.3 Cluster selection

1540 **Extend cluster reconstruction** Neutral particles used in jet reconstruction are re-
 1541 constructed by the Electromagnetic Calorimeter (EMCal [145]). The EMCal covers
 1542 an area with a range of $|\eta| < 0.7$ in pseudorapidity and 100 deg in azimuth. EMCal
 1543 is complimented with the Dijet Calorimeter (DCal) [146] and Photon Spectrom-
 1544 eter (PHOS) [144] that are situated opposite of the EMCal in azimuth. PHOS
 1545 covers 70 degrees in azimuth and $|\eta| < 0.12$. The DCal is technologically identical
 1546 to EMCal. The DCal coverage spans over 67 degrees in azimuth, but in pseudo-
 1547 rapidity the mid region is occupied by the PHOS. In between PHOS and DCal
 1548 active volumes, there is a gap of 10 cm. DCal is fully back-to-back with EMCal.

1549 The clusters used in the analysis were obtained from EMCal by the v2 clus-
 1550 teriser. Clusters matched to charged tracks are removed from the analysis as well
 1551 as clusters being identified as fake. The parameters used in the clusteriser are
 1552 summarised in table 3

1553 The clusteriser searches for a tower with energy deposit greater than a defined
 1554 seed energy and merges all surrounding (sharing a side) towers with energy deposit

higher than a defined threshold. In the next step all towers sharing a side with already included towers are added, again requiring that the energy deposits exceeds the threshold. The algorithm can identify local minima and halts the clustering in case that the neighbouring tower energy is higher. Already clustered towers are removed from the pool, so one tower can only be clustered once.

Highly energetic calorimeter hits should spread into several towers as the electromagnetic shower evolves. However, some clusters with high energy have their energy located in a single tower. These are believed to come from slow neutron hitting the APD readout of the towers. These are called exotic clusters. The measure of exoticity is denoted as

$$1 - \frac{E_{\text{cross}}}{E_{\text{max}}}, \quad (36)$$

where E_{max} is the energy in the most energetic tower and E_{cross} is the sum of the four towers neighbouring the most energetic one. The closer to 1, the more exotic the cluster is and the more probability that it is fake. Cut of 0.97 has been adopted as default for EMCal analyses, including this one.

A method of matching the cluster position to TPC track extrapolation is used to suppress charged hadron contribution to hits in EMCal. Tracks identified by the tracking detectors are extrapolated close to the EMCal surface, where the closest cluster is found and the track extrapolation is continued until reaching the same depth as the cluster. The remaining distance in between the extrapolated track and the cluster is then used to reject hadronic hits.

Table 3: Parameters used in the EMCal clusteriser

Setting	Value	Description
Clusteriser seed	0.2 MeV	
Clusteriser cutoff	0.05 MeV	
Cells in cluster	> 1	
Track matching radius	0.025	
Fiducial cut	1 tower	
Exotic cut	0.97	
Minimal cluster Energy	0.3 GeV	

4 Analysis method

4.1 Jet Finding

The analysis uses reconstructed jets as estimates of the original parton. Essentially when reconstructing jets, nearby tracks are combined into jets. Collisions between

hadrons are never as clean as electron-electron collisions. Even for a proton-proton collision there are participant partons, that will produce a soft background in addition to the hard scattering products. Jet reconstruction must deal with this soft background. The reconstruction is never perfect, one can have uncorrelated tracks that get included in the jet and some tracks originating from the parton are missed by the reconstruction. There are several methods to perform the reconstruction, all of which require some kind of size parameter, which cuts out jet participants too far from the jet axis. The tracks that are grouped into a jet are referred to as jet constituents.

The analysis is performed by analysing jet constituents. In each collision event, the jets are reconstructed using FastJet [162] with the anti- k_T algorithm [163]. Jets for $R=0.4$ are selected in $|\eta| < 0.25$ to satisfy the fiducial acceptance of the EMCAL. In jet reconstruction both charged tracks with $p_T > 0.15 \text{ GeV}/c$ and neutral clusters with $p_T > 0.30 \text{ GeV}/c$ are considered. In the analysis, results are presented in terms of the jet transverse momentum $p_{T\text{jet}}$.

4.1.1 Anti k_T algorithm

Jets are reconstructed using the anti- k_T algorithm [163]. The algorithm works by trying to undo the splittings through combining protojets. The algorithm creates a list of protojets. At the beginning the list is populated by converting each track in the event into a protojet. Then the algorithm proceeds by combining these protojets. A simplified picture of the process for a limited number of tracks is shown in Fig. 31

The algorithm calculates distance measures for each individual protojet and for each possible pair of protojets. For individual protojets this depends only on the transverse momentum of the track.

$$k_{Ti}^2 = p_{Ti}^{2p} \quad (37)$$

For each pair of protojets the distance measure is calculated as

$$k_{Ti,j}^2 = \min(p_{Ti}^{2p}, p_{Tj}^{2p}) \frac{\Delta R_{i,j}^2}{D^2}, \quad (38)$$

where

$$R_{i,j} = (\phi_i - \phi_j)^2 + (y_i - y_j)^2. \quad (39)$$

If k_{Ti} is the smallest quantity then the protojet is a jet and it is removed from further consideration. If $k_{Ti,j}$ is the smallest quantity the two protojets are merged. This is iterated until no protojets are left.

The choice of the power p in the distance measure depends on the algorithm used

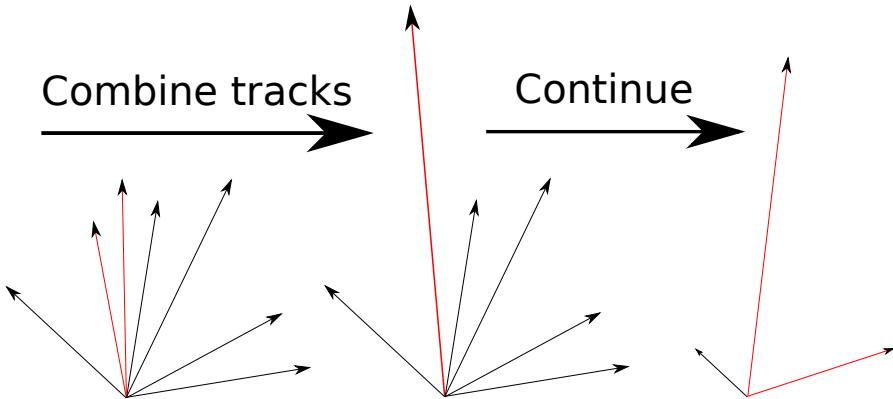


Figure 31: A simple example of the antil- k_{T} algorithm in progress. The red tracks in the leftmost figure are identified to have the smallest $k_{T,i}$ in the event and are combined into the red track of the middle figure. As this continues the remaining tracks are added to this or other jets. One track was deemed to be isolated enough to be counted as a protojet by itself. Note that the rightmost figure is zoomed out.

- ¹⁶¹¹ • $p = 1$: k_{T} algorithm
- ¹⁶¹² • $p = 0$: Cambridge Aachen algorithm
- ¹⁶¹³ • $p = -1$: anti- k_{T} algorithm

¹⁶¹⁴ With the choice $p = -1$ in anti- k_{T} algorithm, the softest splittings are un-
¹⁶¹⁵ done first. One consequence of the power choice in the anti- k_{T} algorithm is that
¹⁶¹⁶ reconstructed jets have a shape close to circular.

¹⁶¹⁷ 4.2 Definition of j_{T}

¹⁶¹⁸ The jet fragmentation transverse momentum, j_{T} , is defined as the component of
¹⁶¹⁹ the constituent particle momentum, \vec{p}_{a} , transverse to the jet momentum, \vec{p}_{jet} . The
¹⁶²⁰ resulting \vec{j}_{T} is illustrated in Fig. 32. The length of the \vec{j}_{T} vector is

$$j_{\text{T}} = \frac{|\vec{p}_{\text{jet}} \times \vec{p}_{\text{track}}|}{|\vec{p}_{\text{jet}}|}. \quad (40)$$

¹⁶²¹ It is commonly interpreted as a transverse kick with respect to the initial hard
¹⁶²² parton momentum that is given to a fragmenting particle during the fragmentation
¹⁶²³ process, which is a measure of the momentum spread of the jet fragments [].

¹⁶²⁴ The reconstructed jet axis is used for j_{T} reference. Any charged track within
¹⁶²⁵ a fixed cone with radius R is taken as a jet constituent, as opposed to using the

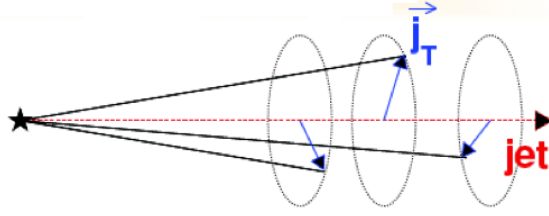


Figure 32: Illustration of \vec{j}_T . The jet fragmentation transverse momentum, \vec{j}_T , is defined as the transverse momentum component of the track momentum, \vec{p}_{track} , with respect to the jet momentum, \vec{p}_{jet} .

1626 constituent list provided by the jet algorithm. Anti- k_T produces jets that are
1627 very circular in shape. Thus this doesn't change the constituent list considerably.
1628 Neutral tracks are used only in jet reconstruction.

1629 j_T results are shown as

$$\frac{1}{j_T} \frac{dN}{dj_T} \quad (41)$$

1630 distributions. The logic behind this is that j_T is inherently a two-dimensional
1631 observable, comprised of j_{Tx} and j_{Ty} components. So the actual physical observable
1632 would be

$$\frac{d^2N}{d j_{Tx} d j_{Ty}} \quad (42)$$

1633 Changing into polar coordinates with $j_{Tr} = j_T$ and θ gives

$$\frac{d^2N}{j_T dj_T d\theta}, \quad (43)$$

1634 where j_T over the azimuth θ should stay constant and it can be integrated over,
1635 which gives

$$\frac{1}{2\pi} \frac{dN}{j_T dj_T}. \quad (44)$$

1636 Results of the raw inclusive j_T distribution in four $p_{T\text{jet}}$ bins with background
1637 are shown in figure 33. Background is further discussed in Sec. 4.4

1638 4.3 Unfolding detector effects

1639 The raw inclusive j_T distributions are corrected for the detector inefficiency using
1640 the unfolding method. The response matrix for the unfolding is obtained from a
1641 PYTHIA [164] simulation.

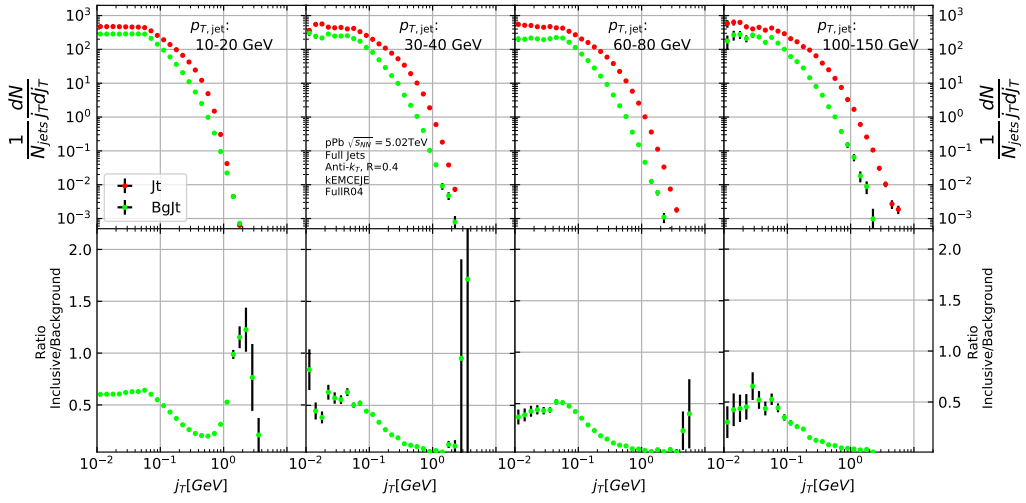


Figure 33: Inclusive j_T with background

1642 Measured distributions are affected by two main factors; Limited acceptance -
 1643 The probability to observe a given event is less than one and limited resolution -
 1644 Quantity x cannot be determined exactly, but there is a measurement error. True
 1645 $f(x)$ and measured $g(y)$ distributions are connected by a convolution integral.
 1646 Including statistical fluctuations this becomes

$$\hat{g}(y) = \int_a^b A(y, x) f(x) dx + \epsilon(y), \quad (45)$$

1647 where A is the detector response obtained by (for example) Monte Carlo simulations
 1648 and $\epsilon(y)$ is the term coming from statistical fluctuations. If x and y are
 1649 discrete variables we have

$$\hat{g}_i = \sum_{j=1}^m A_{ij} f_j + \epsilon_i, \quad (46)$$

1650 Or in matrix form

$$\hat{g} = Af + \epsilon \quad (47)$$

1651 If the only detector effect is limited acceptance, A is a diagonal matrix. In a
 1652 general discrete case the (naive) solution is obtained by the inverse matrix

$$\hat{f} = A^{-1} \hat{g} \quad (48)$$

1653 However this usually leads to oscillating solutions and determining the inverse
 1654 matrix can be difficult.

1655 Two common methods to perform this inversion are Bayesian and SVD unfolding
 1656 methods. Often the solution requires some additional *a priori* information.
 1657 For example the solution should be smooth in most cases.

1658 **4.3.1 Bayesian unfolding**

The bayesian (iterative) method is based on the Bayes formula [].

$$P(C_i|E_j) = \frac{P(E_j|C_i) P_0(C_i)}{\sum_{l=1}^{n_C} P(E_j|C_l) P_0(C_l)},$$

1659 i.e. the probability of Cause ("truth") C_i given Effect ("observed") E_j is proportional to the probability of observing E_j given C_i (response matrix) and the 1660 truth distribution $P_0(C_i)$.
1661

At first P_0 is given some starting distribution, either a uniform distribution or some guess of the final distribution. Taking into account the inefficiency this gives

$$\hat{n}(C_i) = \frac{1}{\epsilon_i} \sum_{j=1}^{n_E} n(E_j) P(C_i|E_j),$$

where

$$P(C_i|E_j) = \frac{P(E_j|C_i) P_0(C_i)}{\sum_{l=1}^{n_C} P(E_j|C_l) P_0(C_l)},$$

1662 and

$$\hat{n}(C_i) = \frac{1}{\epsilon_i} \sum_{j=1}^{n_E} n(E_j) P(C_i|E_j). \quad (49)$$

First $P(C_i|E_j)$ is calculated with the uniform distribution or best guess of the shape of the distribution. This is then used to calculate the new distribution $\hat{P}(C_i)$

$$\hat{N}_{true} = \sum_{i=1}^{n_C} \hat{n}(C_i), \quad \hat{P}(C_i) = P(C_i|n(E)) = \frac{\hat{n}(C_i)}{\hat{N}_{true}}$$

1663 P_0 is then replaced with \hat{P} and the procedure is repeated until an acceptable
1664 solution is found.

1665 The bayesian procedure alongside with the SVD unfolding method are implemented in the RooUnfold package [165], which is used to perform the unfolding in 1666 practice. In RooUnfold the number of iterations is given beforehand. In practice 1667 this requires some trial and error. The number of iterations should be as low as 1668 possible, as the errors increase when going further in the iterations, but the number 1669 of iterations must be high enough so that the correct distribution is extracted.
1670

1671 **Error propagation in the Bayesian procedure**

1672 The measured distribution has some statistical uncertainty, this should be reflected
1673 in the unfolded distribution. Additionally the response matrix may have some
1674 uncertainty if the statistics used in the Monte Carlo simulation were limited.

1675 For errors originating from the measured distribution RooUnfold uses the error
1676 propagation matrix

$$\frac{\partial \hat{n}(C_i)}{\partial n(E_j)} = M_{ij} + \frac{\hat{n}(C_i)}{n_0(C_i)} \frac{\partial n_0(C_i)}{\partial n(E_j)} - \sum_{k=1}^{n_E} \sum_{l=1}^{n_C} \frac{n(E_k) \epsilon_l}{n_0(C_l)} M_{ik} M_{lk} \frac{\partial n_0(C_l)}{\partial n(E_j)}, \quad (50)$$

1677 where $\hat{n}(C_i)$ is the unfolded result from Eq. 49. This depends upon the matrix
1678 $\frac{\partial n_0(C_i)}{\partial n(E_j)}$, which is $\frac{\partial \hat{n}(C_i)}{\partial n(E_j)}$ from the previous iteration. In the first iteration, $\frac{\partial n_0(C_i)}{\partial n(E_j)} = 0$
1679 and $\frac{\partial \hat{n}(C_i)}{\partial n(E_j)} = M_{ij}$.

1680 The error propagation matrix V is used to obtain the covariance matrix on the
1681 unfolded distribution

$$V(\hat{n}(C_k), \hat{n}(C_l)) = \sum_{i,j=1}^{n_E} \frac{\partial \hat{n}(C_k)}{\partial n(E_i)} V(\hat{n}(E_i), \hat{n}(E_j)) \frac{\partial \hat{n}(C_l)}{\partial n(E_j)}, \quad (51)$$

1682 where $V(\hat{n}(E_i), \hat{n}(E_j))$ is the covariance matrix of the measurements. In count-
1683 ing experiments common in particle physics, each bin is independently Poisson
1684 distributed, with

$$V(\hat{n}(E_i), \hat{n}(E_j)) = n(E_i) \delta_{ij} \quad (52)$$

1685 The error propagation matrix for the response matrix is

$$\begin{aligned} \frac{\partial \hat{n}(C_i)}{\partial P(E_j|C_k)} &= \frac{1}{\epsilon_i} \left(\frac{n_0(C_i) n(E_j)}{f_j} - \hat{n}(C_i) \right) \delta_{ik} - \frac{n_0(C_k) n(E_j)}{f_j} M_{ij} + \\ &\quad \frac{\hat{n}(C_i)}{n_0(C_i)} \frac{\partial n_0(C_i)}{\partial P(E_j|C_k)} - \frac{\epsilon_i}{n_0(C_i)} \sum_{l=1}^{n_E} \sum_{r=1}^{n_C} n(E_l) M_{il} M_{rl} \frac{\partial n_0(C_r)}{\partial P(E_j|C_k)}, \end{aligned} \quad (53)$$

1686 where $\frac{\partial n_0(C_i)}{\partial P(E_j|C_k)}$ is the error propagation matrix from the previous iteration,
1687 $\frac{\hat{n}(C_i)}{\partial P(E_j|C_k)}$. From the first iteration, this is zero and the final two terms in Eq. 53
1688 disappear.

1689 The covariance matrix due to these errors is given by

$$V(\hat{n}(C_k), \hat{n}(C_l)) = \sum_{j,s=1}^{n_E} \sum_{i,r=1}^{n_C} \frac{\partial \hat{n}(C_k)}{\partial P(E_j|C_i)} V(P(E_j|C_i), P(E_s|C_r)) \frac{\partial \hat{n}(C_l)}{\partial P(E_s|C_r)}, \quad (54)$$

1690 where $V(P(E_j|C_i), P(E_s|C_r))$ can be taken as multinomial, Poisson or other
1691 distribution.

1692 **4.3.2 Toy Monte Carlo**

1693 **remove?** A toy Monte Carlo simulation was performed to see the performance
1694 in an ideal case. The simulations samples jet p_T values from the observed p_T
1695 distribution. Starting from this p_T the simulations starts creating tracks with

$$p_{\text{track}} = z_{\text{track}} p_{T\text{jet}} \quad (55)$$

1696 where z_{track} is sampled from the observed z distribution. All tracks below 0.15 GeV
1697 are discarded. Sampling is continued until the sum of the track transverse momenta
1698 exceeds the jet transverse momentum. Jet is then defined as the sum of the track
1699 momenta.

1700 Simultaneously a p_T dependant observation efficiency is applied to the tracks
1701 and a separate observed jet is calculated using only the observed tracks. Addi-
1702 tionally a set of fake tracks is added to the observed jet. Tracks are always either
1703 observed or not at the true momentum. No smearing is added to the observed
1704 momentum.

1705 Afterwards the tracks are looped over for j_T calculation. For observed tracks
1706 we calculate j_T with respect to both the true jet axis and the observed jet. 2D
1707 Response matrix is filled with

$$(j_T^{\text{obs}}, p_{T\text{jet}}^{\text{obs}}, j_T^{\text{true}}, p_{T\text{jet}}^{\text{true}}) \quad (56)$$

1708 In practice this is done with a set of 3D histograms, where $p_{T\text{jet},\text{true}}$ determines
1709 the histogram index and the remaining three values the bin in the 3D histogram.

1710 After creating the response matrices, an identical procedure is carried out to
1711 the create testing data. Now instead of filling response matrices, 2D histograms
1712 are filled with $(j_T^{\text{obs}}, p_{T\text{jet}}^{\text{obs}})$ and $(j_T^{\text{true}}, p_{T\text{jet}}^{\text{true}})$

1713 The observed distributions are unfolded using RooUnfold's 2D Bayesian (iter-
1714 ative) algorithm. Results are shown in figure 34. Aside from some discrepancy at
1715 very low j_T the true distribution is retrieved well.

1716 **4.3.3 Pythia Response matrices**

1717 A PYTHIA6 simulation was carried out to determine the response matrices. [Details
1718 of the simulation](#)

1719 Response matrices are filled through correlation between MC detector and
1720 particle level jets and tracks.

1721 The ranges of both j_T and $p_{T\text{jet}}$ extend the ranges in end results. These are
1722 shown in Tab. 4. The ranges are the same in detector and particle level.

1723 When calculating j_T for MC particles the code checks whether a corresponding
1724 detector level track exists and if that track had a j_T value. Additionally the code

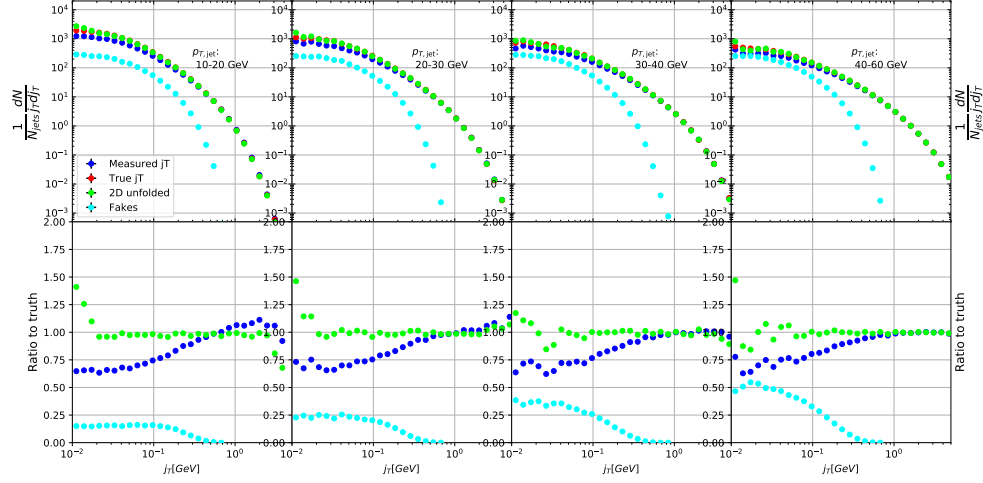


Figure 34: Results from unfolding in Toy Monte Carlo

Table 4: j_T and p_T ranges used in unfolding. The same ranges are used for detector and truth level.

	j_T	$p_{T\text{jet}}$
Min	0.01	5
Max	20	500

1725 checks for detector level tracks that don't have corresponding particle level track
1726 with a j_T value.

1727 There are several possibilities that have to be taken into account:

- 1728 We find a corresponding track with a j_T value, response matrix is filled
1729 normally with $(j_T^{\text{obs}}, p_{T\text{jet}}^{\text{obs}}, j_T^{\text{true}}, p_{T\text{jet}}^{\text{true}})$
- 1730 We don't find a corresponding track. Record $(j_T^{\text{true}}, p_{T\text{jet}}^{\text{true}})$ as a miss
- 1731 We find a corresponding track, but it didn't have j_T value. Most likely
1732 because it was not part of a jet in the detector level set. Similary record
1733 $(j_T^{\text{true}}, p_{T\text{jet}}^{\text{true}})$ as a miss
- 1734 For detector level tracks that have no correspondence in particle level set the
1735 code records $(j_T^{\text{obs}}, p_{T\text{jet}}^{\text{obs}})$ as a fake

1736 In the analysis code the response matrix is made of an array of 3 dimensional
1737 histograms, with $(j_T^{\text{obs}}, p_{T\text{jet}}^{\text{obs}}, j_T^{\text{true}})$ as axes. The histogram index gives the $p_{T\text{jet}}^{\text{true}}$
1738 value.

1739 4.3.4 Unfolding algorithm

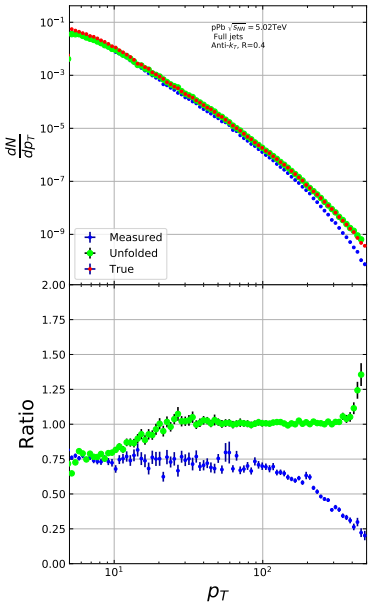
1740 As a primary method unfolding is performed with an iterative (bayesian) algorithm
1741 using the RooUnfold [165] package. The number of iterations used is 4.

1742 4.3.5 Unfolding closure test

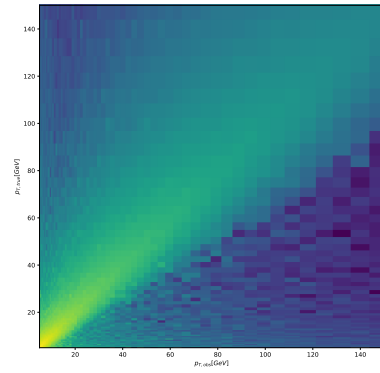
1743 Pythia set is divided in 2 halves. First is used to fill the response matrices, as well
1744 as record missed and fake tracks. Second half is used to test the effectiveness of
1745 the unfolding method. Jet p_T distributions are shown in figure 35a and response
1746 matrix are shown in figure 35b.

1747 Response matrices within single jet p_T bins are shown in figure 36. Results
1748 from the closure test are shown in figure 37. In the lowest jet p_T bins unfolding
1749 fails to recover the true distribution. The lowest jet p_T bins are dominated by
1750 combinatorial jets and thus the true detector response is likely not retrieved.

1751 Above $30 \text{ GeV} < p_{T\text{jet}} < 40 \text{ GeV}$ the distribution is recovered well in the mid
1752 j_T region. At $j_T < 0.1 \text{ GeV}$ there is clear discrepancy. The final results are shown
1753 only for $j_T > 0.1 \text{ GeV}$. Additionally there is some discrepancy at very high j_T .
1754 This is taken into account in the unfolding systematics. (TODO: Show this)



(a) Unfolded jet p_T distribution in PYTHIA closure test



(b) Jet p_T response matrix from unfolding closure test

Figure 35: Jet p_T in unfolding closure test

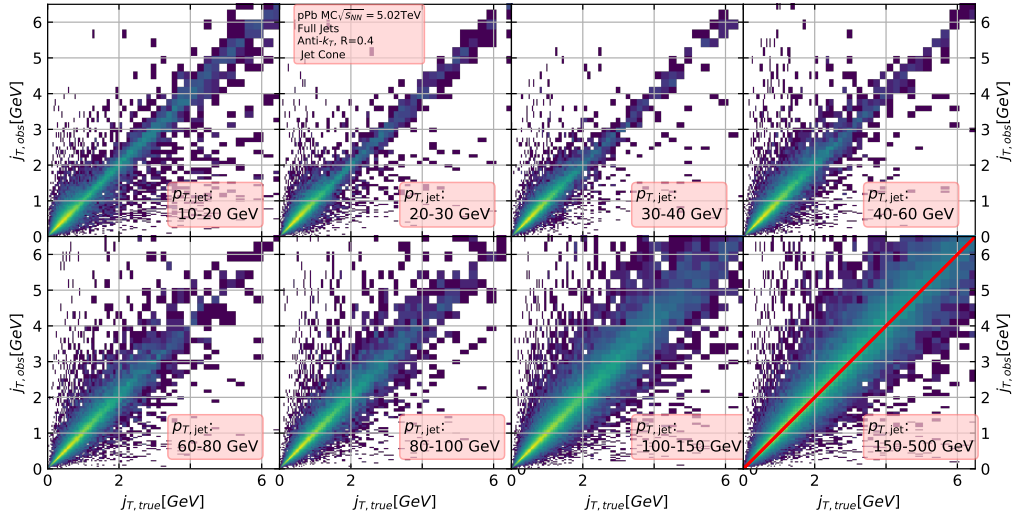


Figure 36: j_T Response matrices in individual $p_{T,jet}$ bins

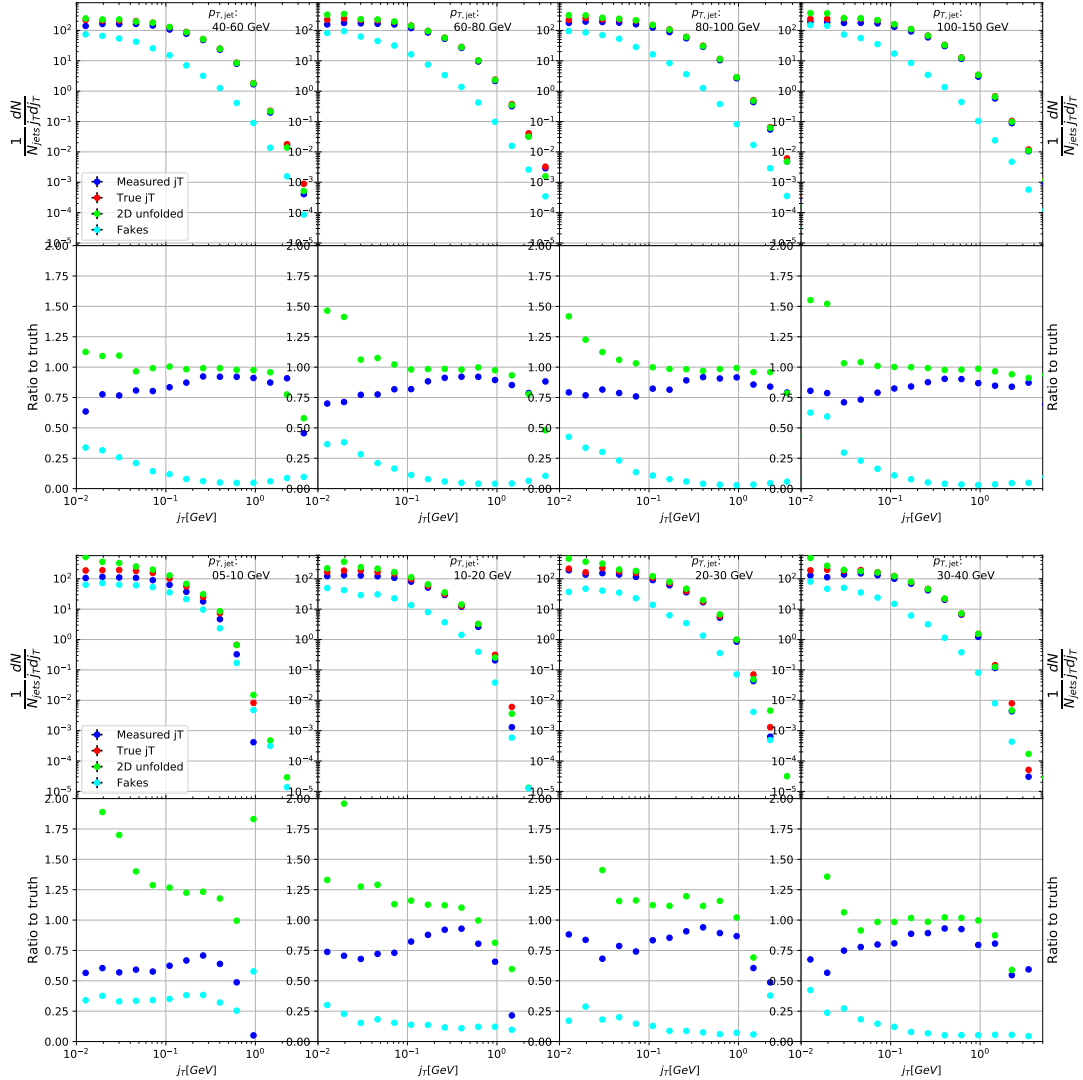


Figure 37: Pythia closure test results. Fake tracks include also tracks that do exist in the true dataset, but for one reason or another were not given j_T values. j_T is only calculated for tracks that are associated with jets

1755 4.4 Background

1756 When calculating j_T distribution for jet constituents there is a contribution from
1757 underlying event (UE), i.e. tracks that just happen to be close to the jet axis.
1758 To find the signal coming from the actual jet we need to subtract the background
1759 (UE) contribution. On a jet-by-jet basis this is impossible, so one must estimate
1760 the background contribution in the inclusive distribution. A schematic view of the
1761 background contribution is shown in Fig. 38.

1762 We have two methods for background estimation. In the first we look at the
1763 direction perpendicular to the jet. This is assumed to be the region least likely to
1764 contain jet contributions. In the second method we randomly assign the tracks of
1765 event new ϕ and η values. The result is thus guaranteed to be uncorrelated.

1766 4.4.1 Perpendicular cone background

1767 As a primary method to estimate the background we look at regions of the detector
1768 where there are no tracks from jets, but only uncorrelated tracks from the under-
1769 lying event. The underlying event is thus estimated by looking at an imaginary
1770 jet cone perpendicular to the observed jet axis ($\frac{\pi}{2}$ Rotation in ϕ).

1771 After calculating the j_T values for tracks in the jet, we rotate the jet axis by
1772 $\frac{\pi}{2}$ in positive ϕ direction. We check that there are no other jets closer than $2R$ to
1773 the rotated axis. If there are then background calculation is skipped for this jet.
1774 Probability of this happening is 1-2% depending on the jet p_T bin.

1775 If we don't find other jets in the vicinity we move on to estimate the background.
1776 We find all tracks within a cone of radius R around the rotated axis and calculate
1777 j_T of these tracks with respect to the rotated axis. Auto-correlations are added to
1778 match effect to jet. (see 4.4.3)

1779 4.4.2 Random background

1780 In the random background method we look at all tracks in the event, except for
1781 tracks close to jets found by the jet algorithm. We randomly assign new η and ϕ
1782 values to all tracks using uniform distributions with $|\eta| < 1.0$. p_T values are kept
1783 the same. To increase statistics there is a possibility to create a number of random
1784 tracks for each actual track. In the analysis we do this 10 times for each track.
1785 Again the track p_T value is kept the same.

1786 We create a random jet cone from uniform η and ϕ distributions. Here $|\eta| <$
1787 0.25. Now we calculate j_T of the random tracks with respect to the random cone
1788 axis. Auto-correlations are added before calculating j_T (see 4.4.3)

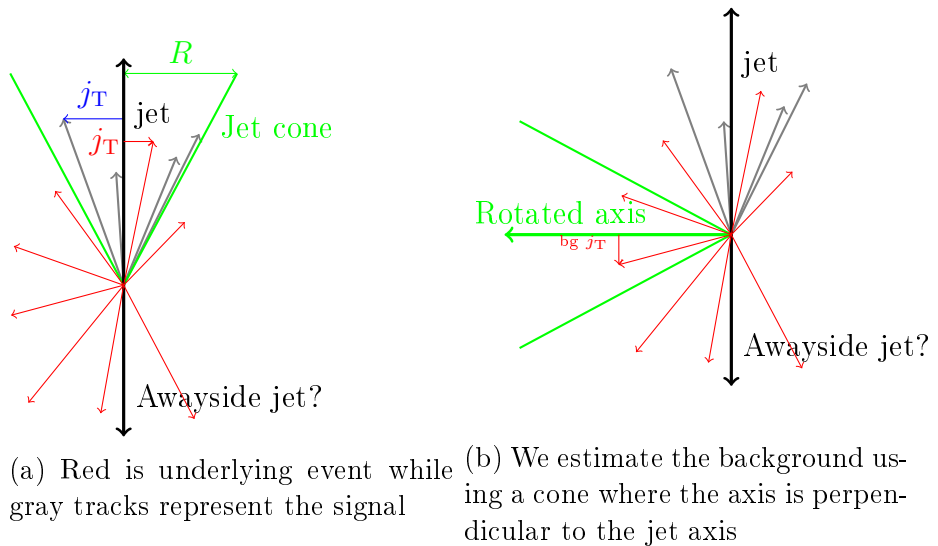


Figure 38: Background estimation

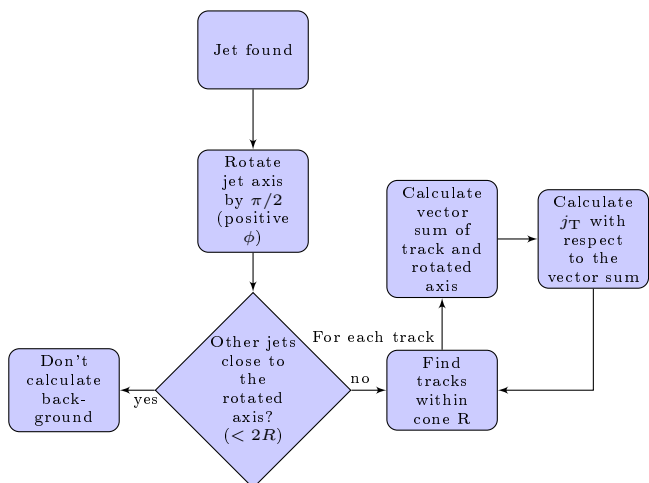


Figure 39: Flowchart representation of the perpendicular cone background procedure

1789 **4.4.3 Auto-correlations**

1790 Jet axis is simply a vector sum of all its constituents. Thus having an additional
1791 track in the jet from the underlying event moves the jet axis towards this track.
1792 Since the axis is now closer to the track, it has a smaller j_T value. Assuming
1793 a 1 GeV background track at the edge of a $R = 0.4$ cone the j_T value would be
1794 0.4 GeV. If this is added to a 5 GeV jet, the j_T value becomes 0.33 GeV. In a 50 GeV
1795 jet it would be 0.39 GeV. This is a region where the inclusive j_T distribution is
1796 dominated by background. The distribution is also steeply falling. Overestimating
1797 the background can lead to a situation where the background estimation exceeds
1798 the inclusive distribution.

1799 To take this effect into account we can't use a fixed axis for background, but
1800 it has to behave like a jet would when additional tracks are added. Thus before
1801 calculating j_T values we make a vector sum of the track and the axis used for back-
1802 ground, which is either the perpendicular cone axis or the random axis depending
1803 on the background method. In each case the momentum of this background axis
1804 is assumed to be the same as the jet which initiated the background estimation.

1805 In pPb data there is on average about one underlying event track in a $R = 0.4$
1806 cone. If there would be more, one should consider taking the vector sum of all
1807 tracks inside the cone. As there is usually only one track and if there are more it's
1808 unlikely that more than one has high momentum, taking the vector sum track-by-
1809 track should be enough.

1810 **4.4.4 Background methods**

1811 Comparison between perpendicular cone and random background in figure 40. The
1812 advantage of the random background method is the added amount of statistics as
1813 the procedure can be repeated several times for each event. However, it seems
1814 that, especially in the highest $p_{T\text{jet}}$ bins there is some jet contribution left at the
1815 high end. Naturally there is no correlation between the tracks and the background
1816 axis, but if some high momentum tracks originating from jets were not subtracted
1817 and happen to hit the edge of the background cone, they can increase the high j_T
1818 yield in the background estimation.

1819 One should note that the results from perpendicular cone background show no
1820 observable change between $p_{T\text{jet}}$ bins. It is a good indication that the background
1821 is actually dominated by the underlying event over the entire j_T region.

1822 **4.5 Fitting**

1823 After unfolding and background subtraction the resulting signal distributions are
1824 fitted with a 2 component function shown in Eq. 57. Gaussian distribution is used

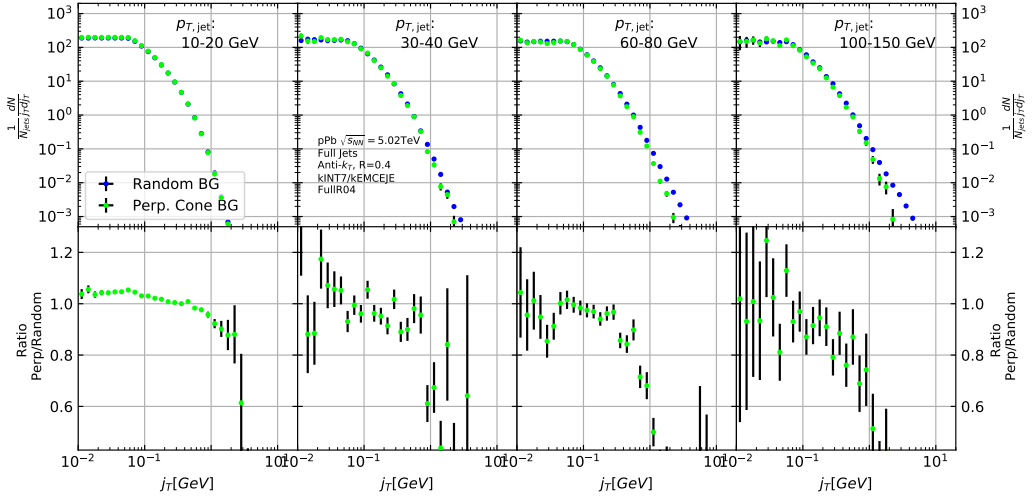


Figure 40: j_T background with two different methods

for low j_T and an inverse gamma function is used for high j_T . The gaussian is taken to have the center at $j_T = 0$. In total this gives 5 parameters. The fitting procedure was inspired by the dihadron j_T analysis by ALICE [2]. The complete fitting function is

$$\frac{1}{N_{\text{jets}} j_T d j_T} \frac{dN}{d j_T} = \frac{B_2}{B_1 \sqrt{2\pi}} e^{-\frac{j_T^2}{2B_1^2}} + \frac{B_3 B_5^{B_4}}{\Gamma(B_4)} \frac{e^{-\frac{B_5}{j_T}}}{j_T^{B_4+1}}. \quad (57)$$

To achieve stable results the fitting is performed in two steps. First both components are fitted separately. Gaussian component is fitted to the low end in j_T . Inverse gamma component is fitted to j_T above 1 GeV/c. After getting the results from the individual fits they are combined into a single function with initial values from the individual results and an additional fit is performed.

After getting the fit function $\sqrt{\langle j_T^2 \rangle}$ (RMS) and yield values are extracted separately from each component. The narrow component RMS is

$$\sqrt{\langle j_T^2 \rangle} = \sqrt{2} B_1,$$

and the wide component RMS value is calculated as

$$\sqrt{\langle j_T^2 \rangle} = \frac{B_5}{\sqrt{(B_4 - 2)(B_4 - 3)}},$$

where it is required that $B_4 > 3$.

₁₈₃₈ The statistical errors can be calculated with the general error propagation
₁₈₃₉ formulas. As a result one gets errors for the narrow component RMS

$$\delta \sqrt{\langle j_T^2 \rangle} = \sqrt{2} \delta B_1 \quad (58)$$

₁₈₄₀ and for the wide component RMS

$$\delta \sqrt{\langle j_T^2 \rangle} = \sqrt{\left(\frac{(5 - 2B_4) B_5 \delta B_4}{(2(B_4 - 2)(B_4 - 3))^{\frac{3}{2}}} \right)^2 + \left(\frac{\delta B_5}{\sqrt{(B_4 - 2)(B_4 - 3)}} \right)^2} \quad (59)$$

5 Systematic errors

Extend Systematics The main systematic uncertainties in this analysis come from the background estimation, the unfolding procedure and uncertainty in the tracking efficiency.

The systematics in background estimation were studied using an alternative method to extract the background, the random background method.

The systematic uncertainty that arises from the unfolding procedure is estimated by performing the unfolding with two separate methods. Data corrected by the iterative unfolding method are used as the results and the SVD unfolding method is employed to estimate the uncertainty. In a PYTHIA closure test the true distribution was in general found to be between the unfolded distributions from the iterative and SVD method. The difference between the methods when unfolding data should give a reasonable estimate of the unfolding uncertainty. The resulting uncertainty is below 8% for both wide and narrow component RMS.

5.1 Background

The uncertainty coming from background estimation is estimated by subtracting the background separately for the perpendicular cone and random background methods. Comparisons of the resulting signal distributions are shown in Fig. 41.

Fits are then performed on both perpendicular cone and random background signals. Difference between them is taken as the systematic error. The fits for individual bins from the random background method are shown in figure 42. Resulting differences between the methods for different components are shown in figure 43. The dotted lines are put at $\pm 5\%$ for the narrow component and at $\pm 8\%$ for the wide component. These are taken as systematic estimates for the entire $p_{T\text{jet}}$ range.

5.2 Unfolding

Unfolding is the second major source of systematic uncertainty. To estimate the uncertainty related to the unfolding procedure several checks are performed. The main systematic uncertainty estimation comes from comparing results performed using both SVD and Bayesian unfolding. Difference between the methods is taken as the systematic error. Since SVD unfolding does not have a 2 dimensional options, the unfolding is done bin by bin. The resulting distributions after SVD unfolding and background subtraction with the perpendicular cone method are shown in fig 44.

As in the background systematic estimation, fits are performed for both cases separately. Resulting differences between the methods for different components

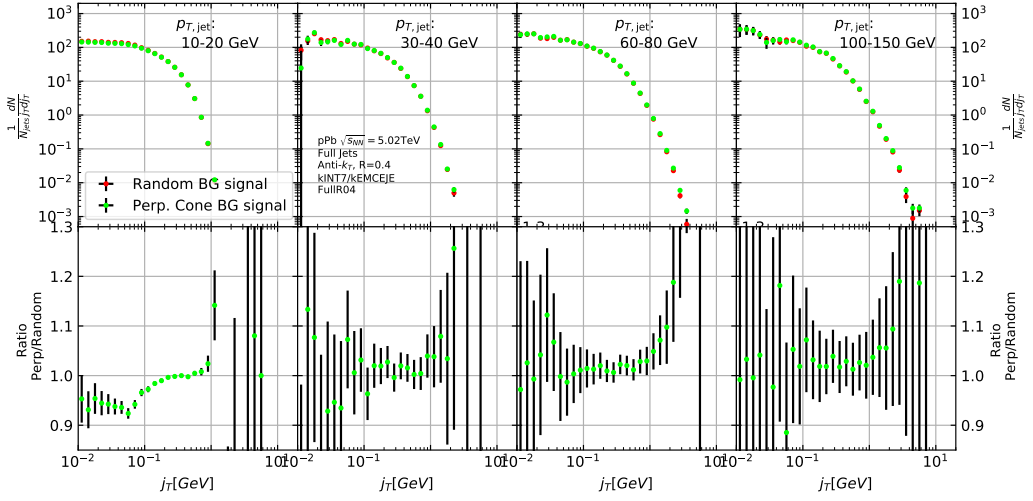


Figure 41: Comparison of the effect of background method on j_T signal.

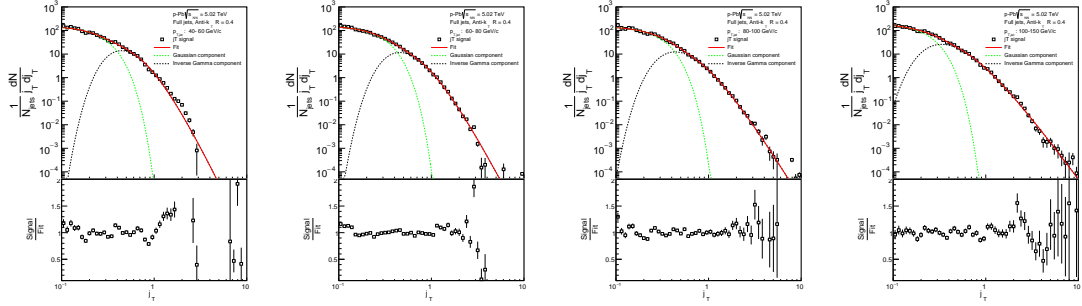


Figure 42: j_T signal with random background subtraction fits in different jet p_T bins

1877 are shown in figure 45. The dotted lines are at $\pm 8\%$ for both components. These
 1878 are taken to be the systematic uncertainty related to unfolding.

1879 Several other systematic checks were performed with the Bayesian unfolding
 1880 procedure. They are described in the following sections. As these are small com-
 1881 pared to the main uncertainty they are not included separately.

1882 5.2.1 Effect of number of iterations

1883 The iterative unfolding algorithm permits the change of number of iterations. The
 1884 unfolding procedure was carried out using different numbers of iterations. The
 1885 results from these different cases are shown in Fig. 46. The results are compared
 1886 to the default unfolding algorithm with 4 iterations. The difference in results

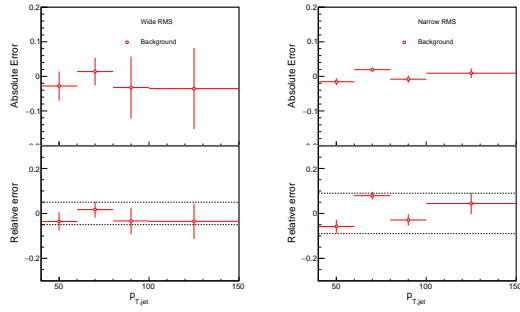


Figure 43: Differences between perpendicular cone and random background subtraction in the resulting RMS values.

Figure 44: Resulting signal distributions from SVD unfolding with the perpendicular cone background methods. These are compared to the results from the Bayesian algorithm to estimate the systematic uncertainty.

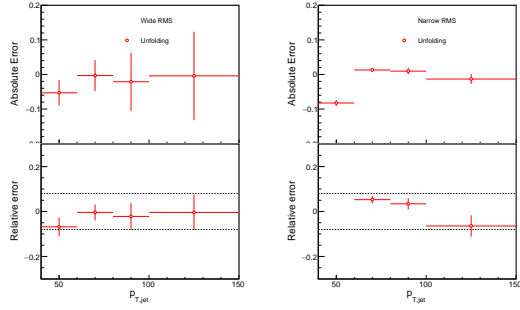


Figure 45: Differences between Bayesian and SVD unfolding in the resulting RMS values

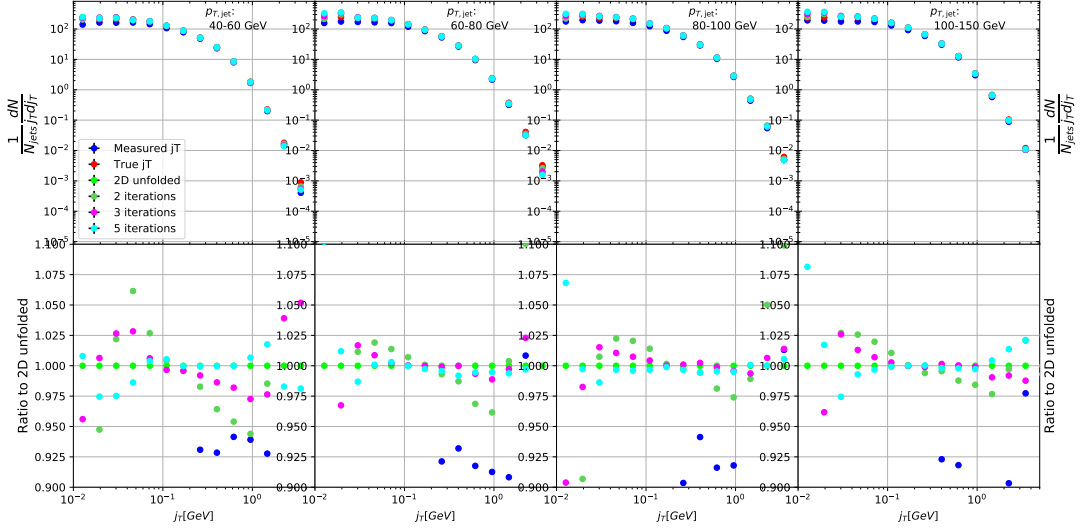


Figure 46: Unfolding with different number of iterations

Figure 47: Effect of changing prior from true distribution in PYTHIA to the unfolded distribution. [Missing figure](#)

1887 between the different cases is mostly less than 2.5%.

1888 5.2.2 Effect of different prior

1889 The iterative algorithm requires a prior estimate of the shape of the distribution.
 1890 As a default prior the truth (particle level) distribution is used. To test the effect
 1891 of changing the prior we instead use the unfolded j_T distribution as prior. The
 1892 results are compared to the unfolding algorithm with the default prior. This is
 1893 shown in Fig. 47 The difference in results between the different cases is mostly less
 1894 than 2.5%.

1895 5.2.3 Effect of p_T truncation

1896 As an additional check the unfolding is carried out with different $p_{T\text{jet}}$ truncation
 1897 values. By default the full range of $p_{T\text{jet}} > 5\text{GeV}$ is used. We test the unfolding
 1898 by only using the response matrix for $p_{T\text{jet}} > 10\text{GeV}$. The results of this test are
 1899 shown in Fig. 48. The effects are strongest in the lower $p_{T\text{jet}}$ bins. Also in this
 1900 case the difference is less than 2.5 % in all $p_{T\text{jet}}$ bins.

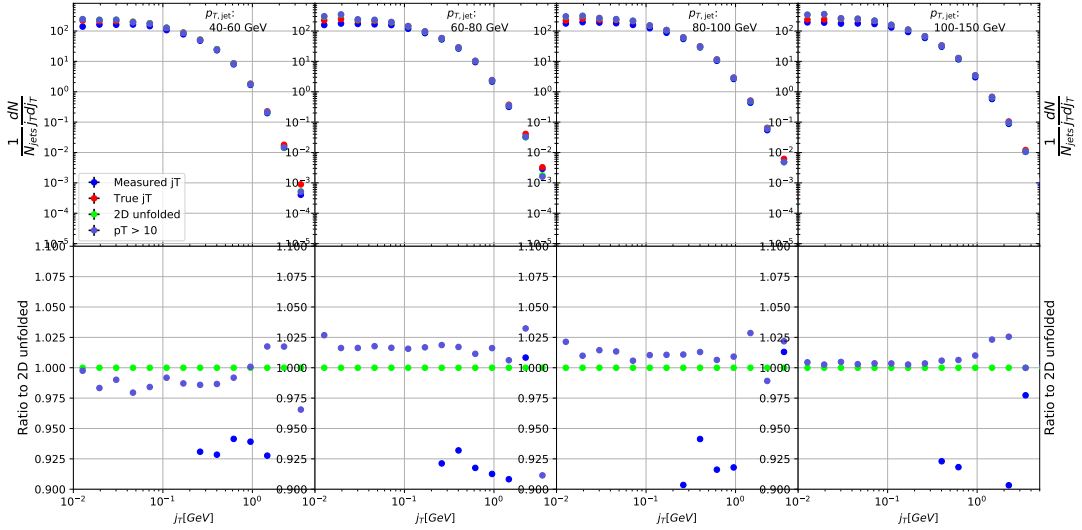


Figure 48: Effect of changing minimum jet p_T used in unfolding from 5 to 10 GeV

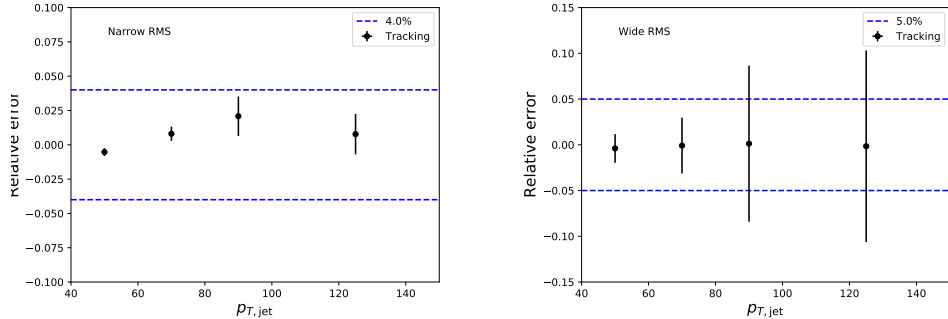


Figure 49: Relative systematic errors resulting from tracking efficiency uncertainty.

1901 5.3 Tracking

1902 Systematic effects originating from uncertainty in the tracking efficiency are es-
 1903 timated through a PYTHIA simulation, where an artificial inefficiency of 3% is
 1904 introduced i.e. 3 % of tracks are randomly removed from each event. The effect
 1905 of this artificial inefficiency is shown in Fig. 49. The systematic uncertainties as-
 1906 signed to tracking efficiency are 4 % for the narrow component and 5 % for the
 1907 wide component.

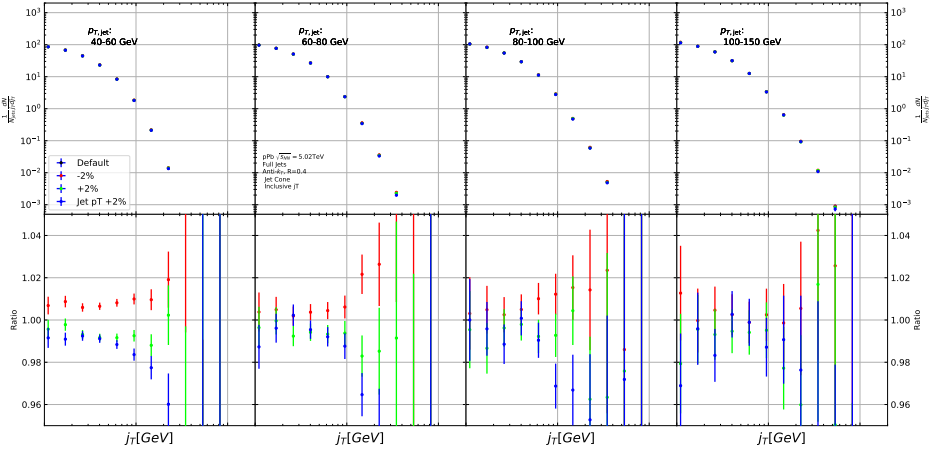


Figure 50: Results from PYTHIA simulations with Cluster energies scaled up and down by 2 %. Additionally jet momenta were scaled by 2 % when determining the jet p_T bin.

1908 5.4 EMCAL clusters

1909 The analysis uses EMCAL clusters only in the reconstruction of jets. Thus the only
 1910 way uncertainty in EMCAL performance can affect the results is through modifica-
 1911 tion of jet momentum or axis.

1912 Uncertainty related to the EMCAL energy scale was estimated by scaling cluster
 1913 energies up and down by 2 % in a PYTHIA particle level simulation. Similarly
 1914 the jet momentum was scaled by $\pm 2\%$ when determining the jet p_T bin. In the
 1915 analysis EMCAL is used only in jet reconstruction, not for calculating j_T . The only
 1916 ways EMCAL uncertainty can affect the analysis are changes in jet energy and jet
 1917 axis. Jet axis shouldn't significantly change, so the main contribution should be
 1918 changes in jet p_T bin.

1919 The resulting differences in the inclusive j_T distributions are shown in Fig. 50.
 1920 Qualitatively the effect of scaling cluster energies is the same as scaling the jet
 1921 energies.

1922 Like in the previous cases fits are performed for the unscaled case and for cases
 1923 with $\pm 2\%$ scaling. The resulting systematic uncertainties are shown in Fig. 51.
 1924 The uncertainty is taken to be 1% for both components.

1925 5.5 Summary/Combining systematics

1926 The different source of the systematic uncertainty are considered as uncorrelated
 1927 and the values of each source are summed in quadrature.

1928 Resulting systematic errors are shown in table 5. The different source of the

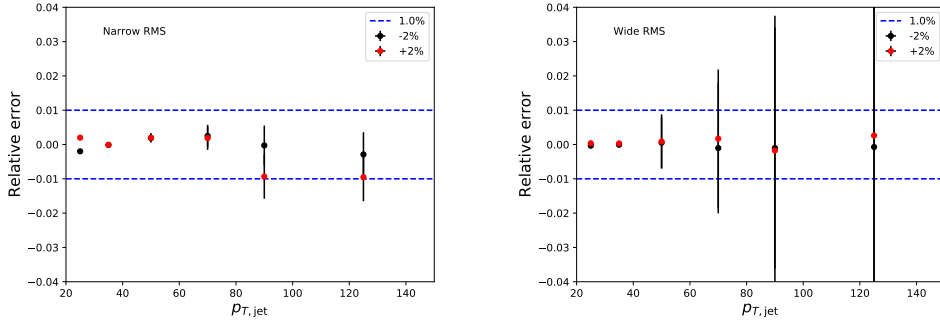


Figure 51: Relative systematic errors resulting from cluster energy uncertainty.

¹⁹²⁹ systematic uncertainty are considered to be uncorrelated and are thus combined ¹⁹³⁰ bin-by-bin in quadrature to get the total systematic errors. The resulting uncer-¹⁹³¹ tainty is approximately 9 % for the wide component RMS and 12 % for the narrow component RMS.

Table 5: Summary of systematic errors

Systematic	Wide RMS	Narrow RMS
Background	5 %	9 %
Unfolding	8 %	8 %
Tracking	4 %	5 %
EMCal	1 %	1 %
Total	10 %	13%

¹⁹³²

¹⁹³³ 5.6 Additional checks

¹⁹³⁴ 5.6.1 Comparison between A and C side

¹⁹³⁵ In 2013 there were issues with tracking. To rule out effects on j_T distributions ¹⁹³⁶ a study was performed comparing j_T distributions between A and C side. (In ¹⁹³⁷ the p-Pb configuration the proton beam is travelling from A to C) No systematic ¹⁹³⁸ differences were observed. Figure 52 shows the comparison between inclusive dis-¹⁹³⁹ tributions between the different sides, both for minimum bias and EMCal triggered ¹⁹⁴⁰ datasets.

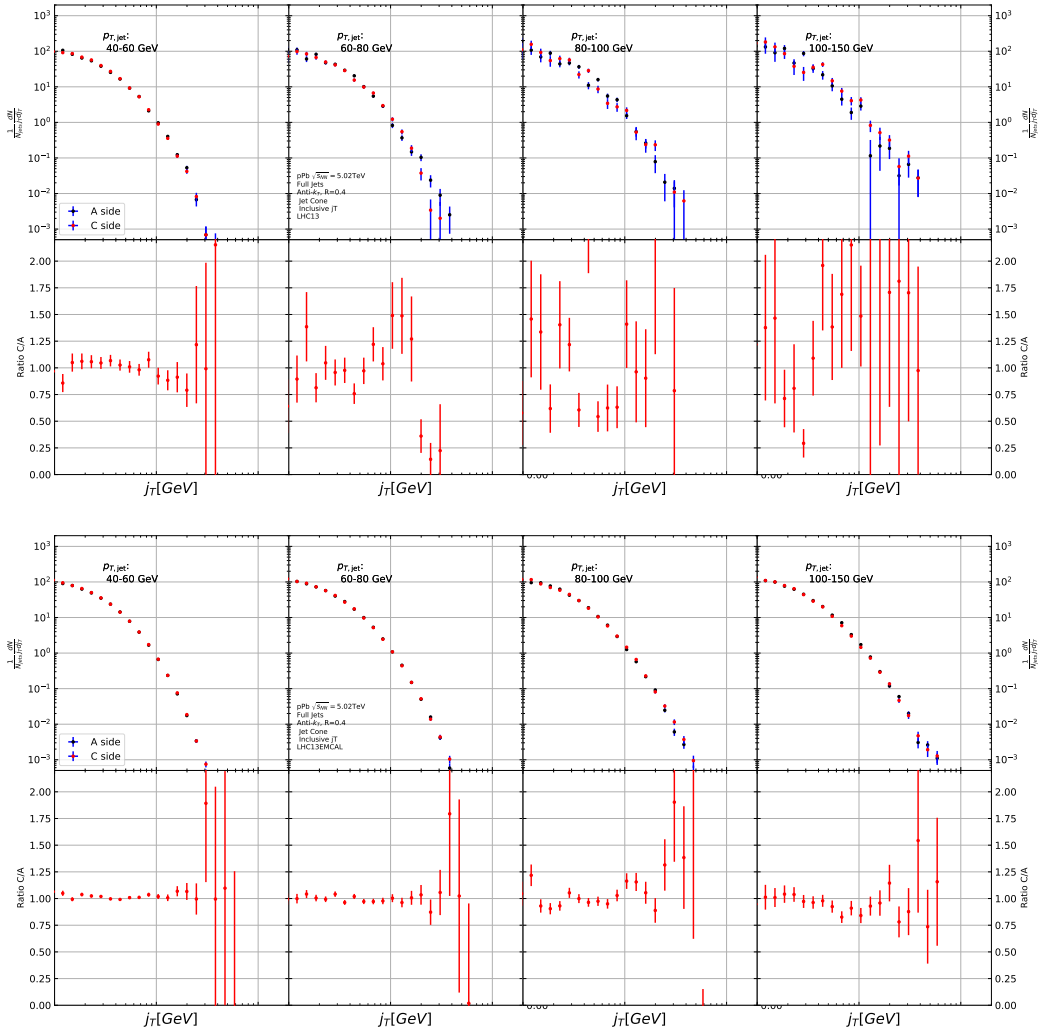


Figure 52: Comparison of inclusive j_T distributions between A and C side for minimum bias and EMCal triggered data.

6 Results

6.1 Fitting

Fits of j_T distributions in different $p_{T\text{jet}}$ bins with $p_{T\text{jet}} > 40 \text{ GeV}$ are shown in figure 53. Additional $p_{T\text{jet}}$ bins are shown in appendix A. In lowest $p_{T\text{jet}}$ bins the jets are mainly combinatorial which makes background subtraction and unfolding difficult and thus the signal can't be trusted.

The fits describe the data well. There is some fluctuation of the order of 10 % around the fit function. At high j_T the statistical errors in the signal are large.

6.1.1 RMS values from fitted distributions

RMS results with systematic errors are shown separately in figure 54. Figure 55 shows RMS values for both components combined. The figure also includes results from a PYTHIA simulation.

6.2 High multiplicity

The analysis was repeated taking only events with high multiplicity. Three different multiplicity cuts were used; 10 %, 1 % and 0.1 %. We used ZDC(TODO) as a centrality estimator. As argued in section 1.6.3 the zero-degree energy deposit should provide a centrality estimator with minimal bias from jets production. Resulting j_T distributions are shown Fig. 56. As the statistics are limited in the high multiplicity runs, it was hard to achieve stable fits to the distributions. Thus the RMS values are not shown.

From the figure one can observe no systematic modification when tighter multiplicity cuts are introduced.

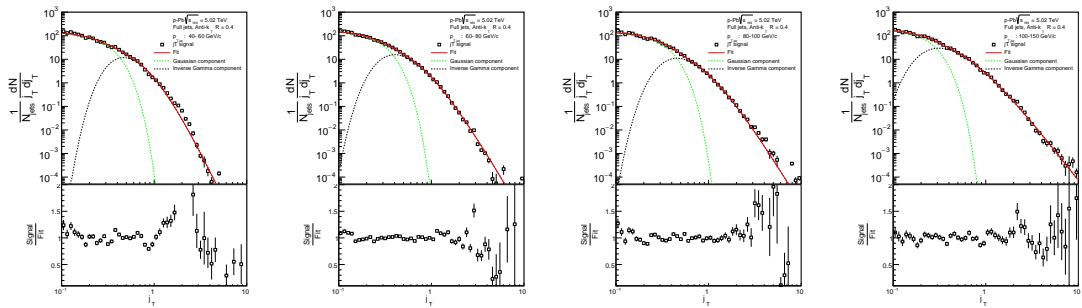


Figure 53: j_T signal fits in different jet p_T bins

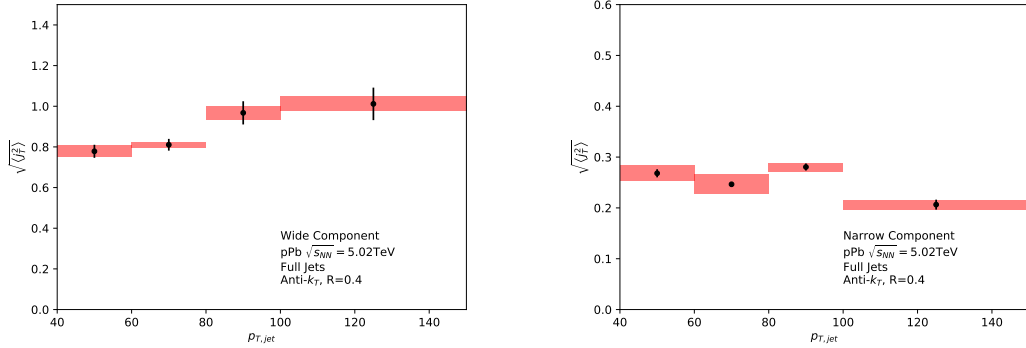


Figure 54: RMS values extracted from the fits for the gaussian (narrow) and inverse gamma (wide) components

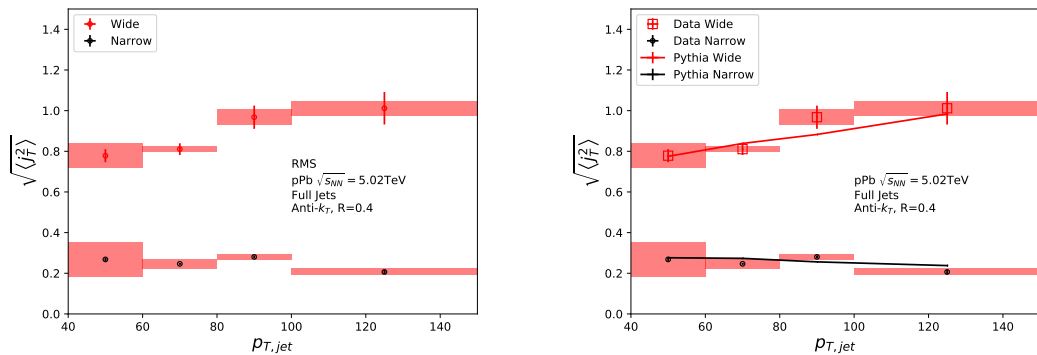


Figure 55: RMS values extracted from the fits for the gaussian (narrow) and inverse gamma (wide) components

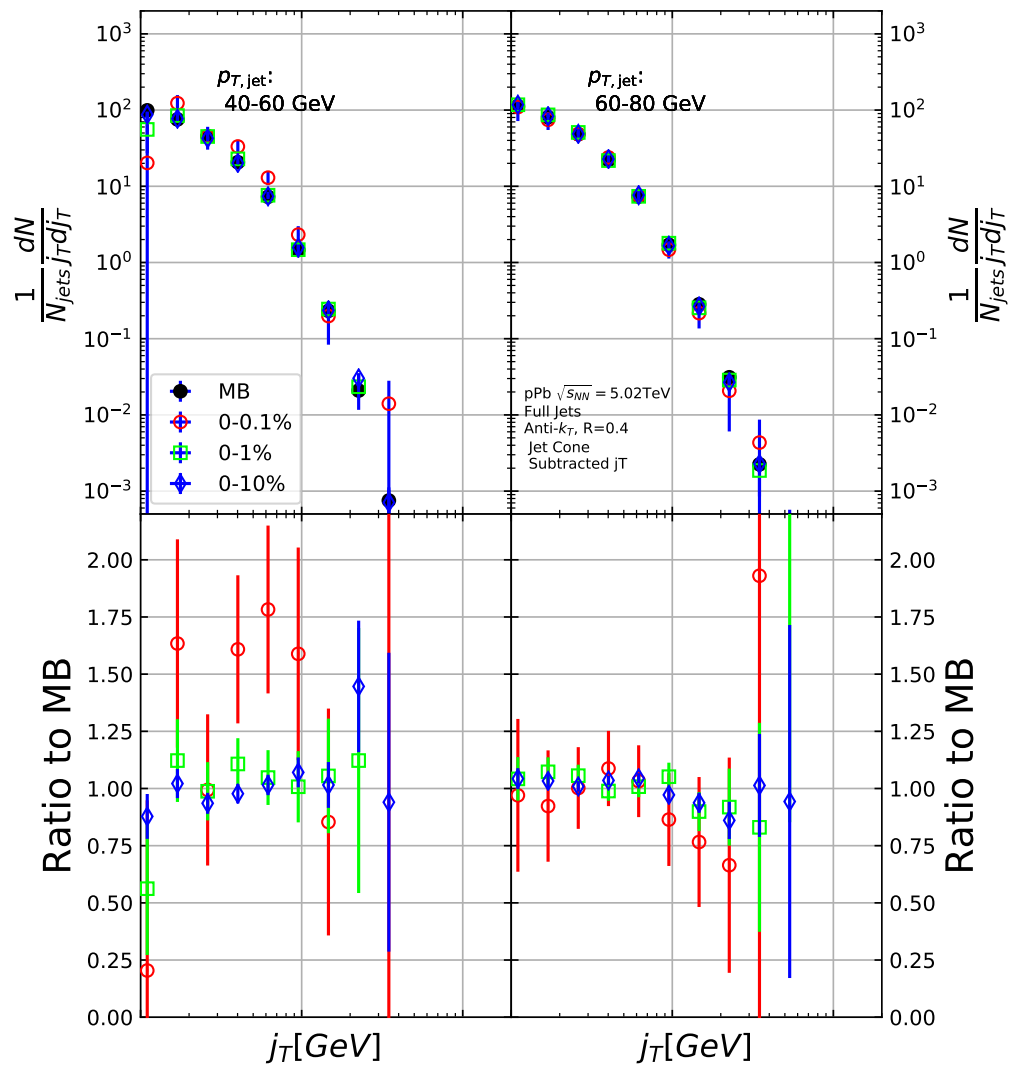


Figure 56: j_T distributions for high multiplicity p–Pb events. Replace figure

7 Discussion

[166, 167]

7.1 Dihadron j_T

The jet fragmentation transverse momentum j_T has been studied previously at ALICE with dihadron correlations [2]. The study took the leading hadron in each event and calculated j_T for any near-side tracks with respect to the leading hadron. Thus there is no kinematical limit to j_T from the jet cone. In the analysis the background shape is estimated using pairs with large $\Delta\eta$. The normalisation of the background is done when fitting the j_T distribution. The inclusive and signal distributions from the analysis are shown in Fig. 57. The inclusive distribution is fitted with a three component function,

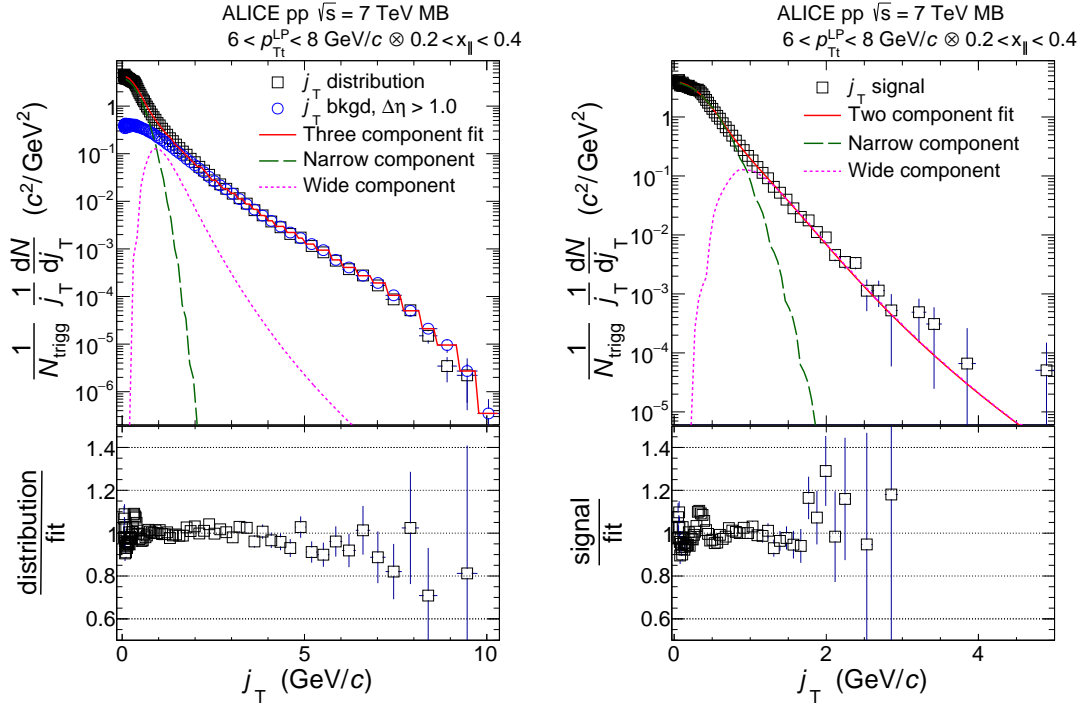


Figure 57: *Left:* Measured j_T distribution including a three-component fit. The three components describe the background (circular symbols), hadronization (long dashed line), and showering (short dashed line). *Right:* The same j_T distribution but with background subtracted.

The analysis was the first to introduce this factorisation of j_T into components.

At $j_T \approx 0.4\text{GeV}$ there is a small bump in the distribution to fit ratio. This was attributed to cases where the trigger particle decayed after hadronisation. As it is difficult to correct for, this bump is included in the systematic errors of the results.

The RMS results from the fitting in both pp and p-Pb collisions are shown in Fig. 58. Qualitatively the results are similar to jet j_T results. The RMS value of the wide component has an increasing trend with respect to p_{Tt}/p_{Tjet} , while the RMS value of the narrow component stays constant. Both components are well described by PYTHIA simulations. As seen in the figures there is no difference between pp and p-Pb results in the dihadron analysis.

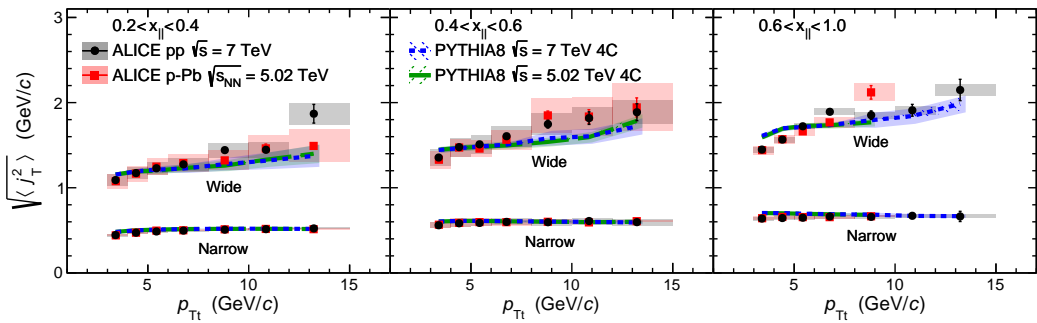


Figure 58: RMS values of the narrow and wide j_T components in the dihadron correlation analysis. Results from pp collisions at $\sqrt{s} = 7\text{ TeV}$ (circular symbols) and from p-Pb collisions at $\sqrt{s_{NN}} = 5.02\text{ TeV}$ (square symbols) are compared to PYTHIA 8 tune 4C simulations at $\sqrt{s} = 7\text{ TeV}$ (short dashed line) and at $\sqrt{s} = 5.02\text{ TeV}$ (long dashed line). Different panels correspond to different x_{\parallel} bins with $0.2 < x_{\parallel} < 0.4$ on the left, $0.4 < x_{\parallel} < 0.6$ in the middle, and $0.6 < x_{\parallel} < 1.0$ on the right. The statistical errors are represented by bars and the systematic errors by boxes. [2]

7.2 Comparing dihadron and jet j_T results

Comparison to RMS values in dihadron analysis [2] are shown in figure 59. For comparison the dihadron trigger p_T bins are converted to jet p_T bins and vice versa. Bin-by-bin comparison is still not possible, but dihadron analysis gives systematically larger RMS values. This could be caused by several kinematical factors. In jet j_T analysis the jet cone limits possible j_T values and thus the width and RMS of the j_T distributions. The effect of this limitation can be studied by changing the cone size as is described in section 7.2.1.

The trends are similar in dihadron and jet j_T results. Wide component RMS values tend to increase with increasing $p_{T,trigger}/p_{Tjet}$. Narrow component RMS

increases slightly in dihadron analysis but not in jet j_T , WHY? (Depends on $x_{||}$ bin in dihadron)

In general dihadron j_T gives wider distributions with larger RMS values. In jet analysis the cone size limits width and thus the RMS values. The effect of this limitation can be studied by changing the cone size as is described in section 7.2.1.

Additionally the leading track is an imperfect estimate of the jet/original parton. Because the leading track in general is at an angle compared to the jet axis, the resulting j_T values are different. In practice the jet axis found by the jet finding algorithm tends to minimize the average j_T of jet constituents. Thus the yield at high j_T is limited and the RMS values are smaller. The effect of having the leading hadron as reference instead of the jet axis is discussed in section 7.2.2

Lastly the results from the dihadron analysis are done in $p_{T,\text{trigger}}$ bins. This favours hard jets, i.e. jets where the leading hadron carries a large momentum fraction and the jet multiplicity is small. In $p_{T,\text{jet}}$ bins jets are more likely to be soft, i.e. small leading momentum fraction and high multiplicity jets.

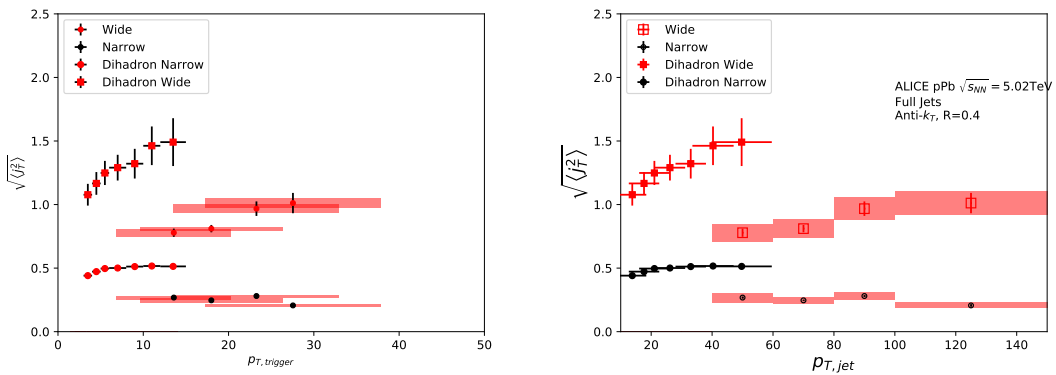


Figure 59: Jet j_T results are compared to results obtained in the dihadron analysis. Dihadron trigger p_T bins are converted to jet p_T bins using observed mean $p_{T,\text{jet}}$ values in $p_{T,\text{trigger}}$ bins. Dihadron results are for $0.2 < x_{||} < 0.4$

7.2.1 Different R parameters

The size of the jet cone gives a limit for j_T . For a track with a fixed momentum p this is a hard limit. This is conveniently seen as j_T can be given in terms of cone size R and momentum p in the small angle approximation limit as

$$j_T \approx p \cdot R \quad (60)$$

Thus for tracks with $p_{T,\text{track}} < p_{T,0}$, $j_T < p_{T,0} \times R$.

2015 In practice the effect of cone sizes on j_T distribution is studied in a PYTHIA simulation.
 2016 Results of the individual distributions and resulting RMS values from this simula-
 2017 tion are shown in Fig. 60 and Fig. 61 respectively. Increasing the cone size of jets
 2018 gives more room for high j_T tracks. This is seen in the individual j_T distributions
 2019 as increased high j_T production. At low j_T there is no change.

2020 When looking at RMS values from wide component we see an increase/decrease
 2021 of about 10% when going from $R = 0.4$ to $R = 0.5/R = 0.3$.

2022 The message from narrow component RMS values is less clear. At low jet p_T
 the behaviour is similar, but at high p_T the order is reversed.

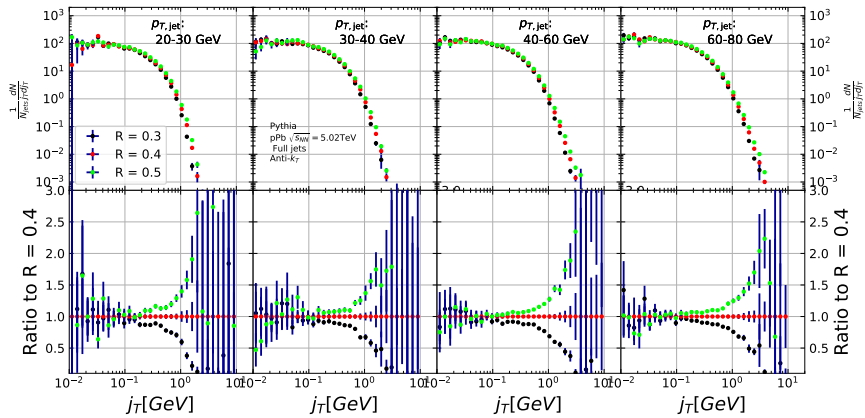


Figure 60: Effect of changing R parameter in jet finding on j_T distributions

2023

2024 7.2.2 Leading tracks versus jet

2025 The leading track is an imperfect estimate of the jet/original parton. Because the
 2026 leading track in general is at an angle compared to the jet axis, the resulting j_T
 2027 values are different. In practice the jet axis found by the jet finding algorithm
 2028 tends to minimize the average j_T of jet constituents. Thus the yield at high j_T is
 2029 limited and the RMS values are smaller.

2030 A PYTHIA study was performed where j_T was calculated with respect to the
 2031 leading track momentum, instead of the jet axis. The results are shown in Fig. 62.
 2032 The resulting j_T distributions are significantly wider than j_T distributions from
 2033 the typical method. The effect seems to be larger than the effect seen in comparing
 2034 different R values.

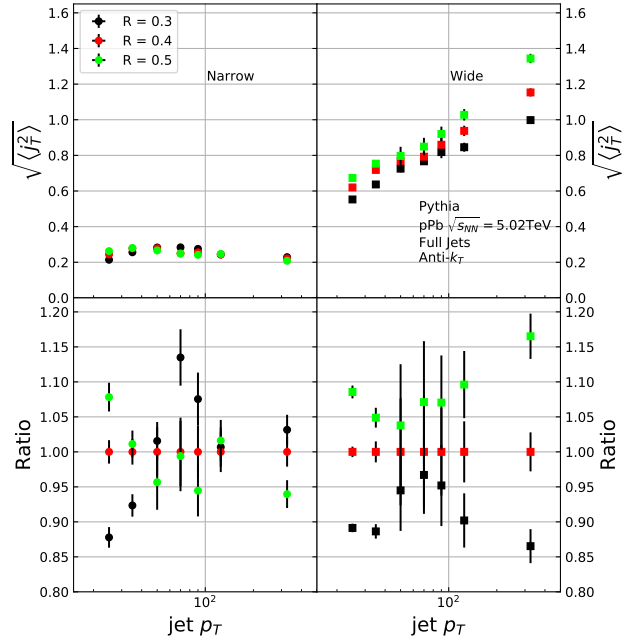


Figure 61: Effect of changing R parameter in jet finding on narrow and wide component RMS values. Wide component RMS values increase with increasing cone size.

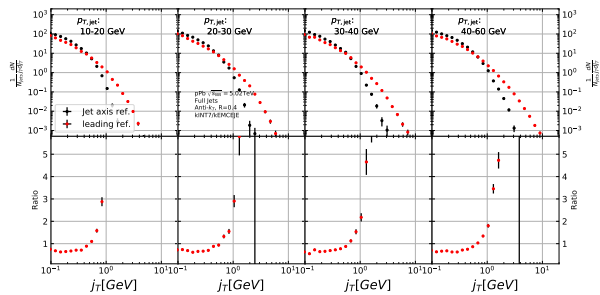


Figure 62: Results of calculating j_T with respect to the jet axis or the leading hadron. The assumption is that because the leading hadron is an imperfect estimate of the jet axis, low j_T tracks should on average be shifted to higher j_T .

2035 **8 Summary**

2036 In this work two distinct j_T components were extracted for narrow and wide contri-
2037 butions using jet reconstruction in $\sqrt{s_{NN}} = 5.02$ TeV p–Pb collisions. RMS values
2038 for both components were obtained. The width of the wide component is found to
2039 increase for increasing $p_{T\text{jet}}$. This is in part explained by the changing kinemati-
2040 cal limits when going to higher $p_{T\text{jet}}$ which allows higher $p_{T\text{track}}$. Additionally the
2041 larger phase space allows stronger parton splitting. The results are qualitatively
2042 compatible with previous studies that studied j_T using two-particle correlations.

2043 [Extend summary](#)

₂₀₄₄ Appendices

₂₀₄₅ A Additional graphs

2046 References

- 2047 [1] ALICE, J. Adam *et al.*, Phys. Rev. **C91**, 064905 (2015), 1412.6828.
- 2048 [2] <https://alice-publications.web.cern.ch/node/3655>, 2018.
- 2049 [3] PHENIX Collaboration, K. Adcox *et al.*, Nucl.Phys. **A757**, 184 (2005),
2050 nucl-ex/0410003.
- 2051 [4] STAR Collaboration, J. Adams *et al.*, Nucl.Phys. **A757**, 102 (2005), nucl-
2052 ex/0501009.
- 2053 [5] J.-Y. Ollitrault, Phys. Rev. D **46**, 229 (1992).
- 2054 [6] U. Heinz and P. Kolb, Nucl. Phys. **A702**, 269 (2002).
- 2055 [7] E. Shuryak, Prog. Part. Nucl. Phys. **62**, 48 (2009).
- 2056 [8] ATLAS Collaboration, J. Jia, Nucl.Phys.A904-905 **2013**, 421c (2013),
2057 1209.4232.
- 2058 [9] R. A. Lacey *et al.*, (2012), 1207.1886.
- 2059 [10] R. Bjorklund, W. Crandall, B. J. Moyer, and H. York, Phys. Review **77**,
2060 213 (1950).
- 2061 [11] W. Heisenberg, Zeitschrift für Physik **77**, 1 (1932).
- 2062 [12] M. Gell-Mann, Phys. Rev. **125**, 1067 (1962).
- 2063 [13] M. Gell-Mann, Phys. Lett. **8**, 214 (1964).
- 2064 [14] O. Greenberg, Phys. Rev. Lett. **13**, 598 (1964).
- 2065 [15] Crystal Ball Collaboration, D. Williams *et al.*, Phys.Rev. **D38**, 1365 (1988).
- 2066 [16] W. Krolikowski, Nuovo Cim. **A27**, 194 (1975).
- 2067 [17] D. J. Gross and F. Wilczek, Physical Review Letters **30**, 1343 (1973).
- 2068 [18] H. D. Politzer, Physical Review Letters **30**, 1346 (1973).
- 2069 [19] D. J. Gross and F. Wilczek, Physical Review D **8**, 3633 (1973).
- 2070 [20] D. J. Gross and F. Wilczek, Physical Review D **9**, 980 (1974).
- 2071 [21] H. Georgi and H. D. Politzer, Physical Review D **9**, 416 (1974).

- 2072 [22] H. Fritzsch, M. Gell-Mann, and H. Leutwyler, Physics Letters B **47**, 365
2073 (1973).
- 2074 [23] I. Flegel and P. Söding, CERN courier (2004).
- 2075 [24] R. Brandelik *et al.*, Physics Letters B **86**, 243 (1979).
- 2076 [25] J. K. L. MacDonald, Phys. Rev. **43**, 830 (1933).
- 2077 [26] C. Berger *et al.*, Physics Letters B **86**, 418 (1979).
- 2078 [27] J. Collins and M. Perry, Phys. rev. Lett. **34**, 1353 (1975).
- 2079 [28] E. Shuryak, Phys. Reps. **61**, 71 (1980).
- 2080 [29] K. Rajagopal, SLAC Beam Line **31-2**, 9 (2001).
- 2081 [30] P. Kovtun, D. Son, and A. Starinets, Phys.Rev.Lett. **94**, 111601 (2005),
2082 hep-th/0405231.
- 2083 [31] R. A. Lacey *et al.*, Phys. Rev. Lett. **98**, 092301 (2007).
- 2084 [32] E. Lofgren, *ACCELERATOR DIVISION ANNUAL REPORTS, 1 JULY*
2085 *1972 12/31/1974* (, 1975).
- 2086 [33] D. S. Barton, Heavy ion program at bnl: Ags, rhic, in *Proc. 1987 Particle*
2087 *Accelerator Conference, Washington, D.C., March, 1987*, 1987.
- 2088 [34] I. Vitev and M. Gyulassy, Phys.Rev.Lett. **89**, 252301 (2002), hep-
2089 ph/0209161.
- 2090 [35] A. Kovalenko *et al.*, Status of the nuclotron, in *Proceedings of EPAC Vol. 94*,
2091 pp. 161–164, 1994.
- 2092 [36] NA61/SHINE, K. Grebieszkow, PoS **CPOD2013**, 004 (2013).
- 2093 [37] BRAHMS Collaboration, I. Arsene *et al.*, Nucl.Phys. **A757**, 1 (2005), nucl-
2094 ex/0410020.
- 2095 [38] B. Back *et al.*, Nucl.Phys. **A757**, 28 (2005), nucl-ex/0410022.
- 2096 [39] S. A. Voloshin, A. M. Poskanzer, and R. Snellings, (2008), 0809.2949.
- 2097 [40] S. A. Voloshin, A. M. Poskanzer, A. Tang, and G. Wang, Phys.Lett. **B659**,
2098 537 (2008), 0708.0800.

- 2099 [41] H. Holopainen, H. Niemi, and K. J. Eskola, Phys.Rev. **C83**, 034901 (2011),
 2100 1007.0368.
- 2101 [42] ALICE Collaboration, Phys. Rev. C **88**, 044909 (2013).
- 2102 [43] M. L. Miller, K. Reygers, S. J. Sanders, and P. Steinberg,
 2103 Ann.Rev.Nucl.Part.Sci. **57**, 205 (2007), nucl-ex/0701025.
- 2104 [44] R. Glauber, Lectures in theoretical physics, 1959.
- 2105 [45] W. Czyż and L. Maximon, Annals of Physics **52**, 59 (1969).
- 2106 [46] A. Białas, M. Bleszyński, and W. Czyż, Nuclear Physics B **111**, 461 (1976).
- 2107 [47] PHENIX Collaboration, S. Afanasiev *et al.*, Phys.Rev. **C80**, 054907 (2009),
 2108 0903.4886.
- 2109 [48] J.-Y. Ollitrault, Eur.J.Phys. **29**, 275 (2008), 0708.2433.
- 2110 [49] P. Romatschke, Int.J.Mod.Phys. **E19**, 1 (2010), 0902.3663.
- 2111 [50] L. LD, Izv. Akad. Nauk Ser. Fiz. **17**, 51 (1953).
- 2112 [51] J. D. Bjorken, Phys. Rev. D **27**, 140 (1983).
- 2113 [52] G. Baym, B. L. Friman, J. P. Blaizot, M. Soyeur, and W. Czyz, Nucl. Phys.
 2114 **A407**, 541 (1983).
- 2115 [53] H. von Gersdorff, L. McLerran, M. Kataja, and P. V. Ruuskanen, Phys.
 2116 Rev. D **34**, 794 (1986).
- 2117 [54] K. A. *et al.* [ALICE Collaboration], Phys. Rev. Lett **106** (2011), 032301.
- 2118 [55] J.-Y. Ollitrault, Phys.Rev. D **48**, 1132 (1993), hep-ph/9303247.
- 2119 [56] P. Danielewicz and G. Odyniec, Physics Letters B **157**, 146 (1985).
- 2120 [57] P. Danielewicz and M. Gyulassy, Physics Letters B **129**, 283 (1983).
- 2121 [58] T. Abbott *et al.*, Phys. Rev. Lett. **70**, 1393 (1993).
- 2122 [59] S. Voloshin and Y. Zhang, Z.Phys. **C70**, 665 (1996), hep-ph/9407282.
- 2123 [60] E877 Collaboration, J. Barrette *et al.*, Phys.Rev.Lett. **73**, 2532 (1994), hep-
 2124 ex/9405003.

- ²¹²⁵ [61] V. N. Gribov and L. N. Lipatov, Sov. J. Nucl. Phys. **15**, 438 (1972), [Yad.
²¹²⁶ Fiz.15,781(1972)].
- ²¹²⁷ [62] G. Altarelli and G. Parisi, Nucl. Phys. **B126**, 298 (1977).
- ²¹²⁸ [63] Y. L. Dokshitzer, Sov. Phys. JETP **46**, 641 (1977), [Zh. Eksp. Teor.
²¹²⁹ Fiz.73,1216(1977)].
- ²¹³⁰ [64] Y. I. Azimov, Y. L. Dokshitzer, V. A. Khoze, and S. I. Trovan, Zeitschrift
²¹³¹ für Physik C Particles and Fields **27**, 65 (1985).
- ²¹³² [65] B. Andersson, G. Gustafson, G. Ingelman, and T. Sjöstrand, Physics Reports
²¹³³ **97**, 31 (1983).
- ²¹³⁴ [66] A. Buckley *et al.*, Phys. Rept. **504**, 145 (2011), 1101.2599.
- ²¹³⁵ [67] M. Bahr *et al.*, Eur. Phys. J. **C58**, 639 (2008), 0803.0883.
- ²¹³⁶ [68] ALICE Collaboration, K. Aamodt *et al.*, Phys.Lett. **B696**, 30 (2011),
²¹³⁷ 1012.1004.
- ²¹³⁸ [69] WA98 Collaboration, M. Aggarwal *et al.*, Eur.Phys.J. **C23**, 225 (2002),
²¹³⁹ nucl-ex/0108006.
- ²¹⁴⁰ [70] D. G. d'Enterria, Phys.Lett. **B596**, 32 (2004), nucl-ex/0403055.
- ²¹⁴¹ [71] PHENIX Collaboration, A. Adare *et al.*, Phys.Rev.Lett. **101**, 232301 (2008),
²¹⁴² 0801.4020.
- ²¹⁴³ [72] STAR Collaboration, J. Adams *et al.*, Phys.Rev.Lett. **91**, 172302 (2003),
²¹⁴⁴ nucl-ex/0305015.
- ²¹⁴⁵ [73] A. Dainese, C. Loizides, and G. Paic, Eur.Phys.J. **C38**, 461 (2005), hep-
²¹⁴⁶ ph/0406201.
- ²¹⁴⁷ [74] I. Vitev, J.Phys. **G30**, S791 (2004), hep-ph/0403089.
- ²¹⁴⁸ [75] C. A. Salgado and U. A. Wiedemann, Phys.Rev. **D68**, 014008 (2003), hep-
²¹⁴⁹ ph/0302184.
- ²¹⁵⁰ [76] N. Armesto, A. Dainese, C. A. Salgado, and U. A. Wiedemann, Phys.Rev.
²¹⁵¹ **D71**, 054027 (2005), hep-ph/0501225.
- ²¹⁵² [77] T. Renk, H. Holopainen, R. Paatelainen, and K. J. Eskola, Phys.Rev. **C84**,
²¹⁵³ 014906 (2011), 1103.5308.

- 2154 [78] CMS Collaboration, S. Chatrchyan *et al.*, Eur.Phys.J. **C72**, 1945 (2012),
2155 1202.2554.
- 2156 [79] PHENIX Collaboration, S. Afanasiev *et al.*, Phys. Rev. C **80**, 054907 (2009).
- 2157 [80] ALICE Collaboration, K. Aamodt *et al.*, Phys.Rev.Lett. **108**, 092301 (2012),
2158 1110.0121.
- 2159 [81] CMS Collaboration, S. Chatrchyan *et al.*, Phys.Rev.Lett. **109**, 022301
2160 (2012), 1204.1850.
- 2161 [82] R. Baier, Y. L. Dokshitzer, A. H. Mueller, S. Peigne, and D. Schiff, Nucl.
2162 Phys. **B484**, 265 (1997), hep-ph/9608322.
- 2163 [83] W. H. H. Bethe and, Proc.Roy.Soc.Lond. **A146** (1934).
- 2164 [84] L. D. Landau and I. Pomeranchuk, Dokl. Akad. Nauk Ser. Fiz. **92**, 535
2165 (1953).
- 2166 [85] A. B. Migdal, Phys. Rev. **103**, 1811 (1956).
- 2167 [86] P. Bosted *et al.*, Quantum-mechanical suppression of bremsstrahlung*, 1993.
- 2168 [87] A. Majumder and M. Van Leeuwen, Prog.Part.Nucl.Phys. **A66**, 41 (2011),
2169 1002.2206.
- 2170 [88] F. Dominguez, C. Marquet, A. Mueller, B. Wu, and B.-W. Xiao, Nucl.Phys.
2171 **A811**, 197 (2008), 0803.3234.
- 2172 [89] M. Gyulassy, P. Levai, and I. Vitev, Nucl.Phys. **B571**, 197 (2000), hep-
2173 ph/9907461.
- 2174 [90] U. A. Wiedemann, Nucl.Phys. **B588**, 303 (2000), hep-ph/0005129.
- 2175 [91] P. B. Arnold, G. D. Moore, and L. G. Yaffe, JHEP **0112**, 009 (2001), hep-
2176 ph/0111107.
- 2177 [92] X.-N. Wang and X.-f. Guo, Nucl.Phys. **A696**, 788 (2001), hep-ph/0102230.
- 2178 [93] T. Sjostrand, S. Mrenna, and P. Z. Skands, Comput.Phys.Commun. **178**,
2179 852 (2008), 0710.3820.
- 2180 [94] I. Lokhtin and A. Snigirev, Eur.Phys.J. **C45**, 211 (2006), hep-ph/0506189.
- 2181 [95] N. Armesto, L. Cunqueiro, and C. A. Salgado, Nucl.Phys. **A830**, 271C
2182 (2009), 0907.4706.

- ²¹⁸³ [96] K. Zapp, G. Ingelman, J. Rathsman, J. Stachel, and U. A. Wiedemann,
²¹⁸⁴ Eur.Phys.J. **C60**, 617 (2009), 0804.3568.
- ²¹⁸⁵ [97] T. Renk, Phys.Rev. **C79**, 054906 (2009), 0901.2818.
- ²¹⁸⁶ [98] PHENIX, K. Adcox *et al.*, Phys. Rev. Lett. **88**, 022301 (2002), nucl-
²¹⁸⁷ ex/0109003.
- ²¹⁸⁸ [99] STAR, J. Adams *et al.*, Phys. Rev. Lett. **91**, 072304 (2003), nucl-ex/0306024.
- ²¹⁸⁹ [100] BRAHMS, I. Arsene *et al.*, Phys. Rev. Lett. **91**, 072305 (2003), nucl-
²¹⁹⁰ ex/0307003.
- ²¹⁹¹ [101] CMS, V. Khachatryan *et al.*, JHEP **04**, 039 (2017), 1611.01664.
- ²¹⁹² [102] ALICE, S. Acharya *et al.*, JHEP **11**, 013 (2018), 1802.09145.
- ²¹⁹³ [103] PHENIX, A. Adare *et al.*, Phys. Rev. **C77**, 011901 (2008), 0705.3238.
- ²¹⁹⁴ [104] PHENIX, A. Adare *et al.*, Phys. Rev. Lett. **111**, 032301 (2013), 1212.3323.
- ²¹⁹⁵ [105] ALICE, J. Adam *et al.*, Phys. Lett. **B746**, 1 (2015), 1502.01689.
- ²¹⁹⁶ [106] CMS, A. M. Sirunyan *et al.*, Phys. Rev. Lett. **121**, 242301 (2018),
²¹⁹⁷ 1801.04895.
- ²¹⁹⁸ [107] CMS, S. Chatrchyan *et al.*, Phys. Rev. **C90**, 024908 (2014), 1406.0932.
- ²¹⁹⁹ [108] ALICE, S. Acharya *et al.*, JHEP **10**, 139 (2018), 1807.06854.
- ²²⁰⁰ [109] A. Kurkela and U. A. Wiedemann, Phys. Lett. **B740**, 172 (2015), 1407.0293.
- ²²⁰¹ [110] JETSCAPE, Y. Tachibana *et al.*, Jet substructure modification in a QGP
²²⁰² from a multi-scale description of jet evolution with JETSCAPE, 2018,
²²⁰³ 1812.06366.
- ²²⁰⁴ [111] P. Aurenche and B. G. Zakharov, Eur. Phys. J. **C71**, 1829 (2011), 1109.6819.
- ²²⁰⁵ [112] A. Beraudo, J. G. Milhano, and U. A. Wiedemann, Phys. Rev. **C85**, 031901
²²⁰⁶ (2012), 1109.5025.
- ²²⁰⁷ [113] A. Beraudo, J. G. Milhano, and U. A. Wiedemann, JHEP **07**, 144 (2012),
²²⁰⁸ 1204.4342.
- ²²⁰⁹ [114] J. Casalderrey-Solana, Y. Mehtar-Tani, C. A. Salgado, and K. Tywoniuk,
²²¹⁰ Phys. Lett. **B725**, 357 (2013), 1210.7765.

- ₂₂₁₁ [115] F. D'Eramo, M. Lekaveckas, H. Liu, and K. Rajagopal, JHEP **05**, 031 (2013), 1211.1922.
- ₂₂₁₃ [116] A. Ayala, I. Dominguez, J. Jalilian-Marian, and M. E. Tejeda-Yeomans, Phys. Rev. **C94**, 024913 (2016), 1603.09296.
- ₂₂₁₅ [117] J. L. Nagle and W. A. Zajc, Ann. Rev. Nucl. Part. Sci. **68**, 211 (2018), 1801.03477.
- ₂₂₁₇ [118] E735, T. Alexopoulos *et al.*, Phys. Rev. **D48**, 984 (1993).
- ₂₂₁₈ [119] MiniMax, T. C. Brooks *et al.*, Phys. Rev. **D61**, 032003 (2000), hep-ex/9906026.
- ₂₂₂₀ [120] C. Shen, Z. Qiu, and U. Heinz, Phys. Rev. **C92**, 014901 (2015), 1502.04636.
- ₂₂₂₁ [121] PHENIX, A. Adare *et al.*, Phys. Rev. **C94**, 064901 (2016), 1509.07758.
- ₂₂₂₂ [122] C. A. Salgado and J. P. Wessels, Ann. Rev. Nucl. Part. Sci. **66**, 449 (2016).
- ₂₂₂₃ [123] M. Gyulassy, I. Vitev, X.-N. Wang, and B.-W. Zhang, p. 123 (2003), nucl-th/0302077.
- ₂₂₂₅ [124] E. Norbeck, K. Šafařík, and P. A. Steinberg, Annual Review of Nuclear and Particle Science **64**, 383 (2014), <https://doi.org/10.1146/annurev-nucl-102912-144532>.
- ₂₂₂₈ [125] A. Accardi, F. Arleo, W. K. Brooks, D. D'Enterria, and V. Muccifora, Riv. Nuovo Cim. **32**, 439 (2010), 0907.3534.
- ₂₂₃₀ [126] 2019.
- ₂₂₃₁ [127] O. S. Brüning *et al.*, *LHC Design Report*CERN Yellow Reports: Monographs (CERN, Geneva, 2004).
- ₂₂₃₃ [128] ATLAS, G. Aad *et al.*, Phys. Lett. **B716**, 1 (2012), 1207.7214.
- ₂₂₃₄ [129] CMS, S. Chatrchyan *et al.*, Phys. Lett. **B716**, 30 (2012), 1207.7235.
- ₂₂₃₅ [130] LHCb, A. A. Alves, Jr. *et al.*, JINST **3**, S08005 (2008).
- ₂₂₃₆ [131] TOTEM, G. Anelli *et al.*, JINST **3**, S08007 (2008).
- ₂₂₃₇ [132] T. ALICE Collaboration *et al.*, Journal of Instrumentation **3**, S08002 (2008).
- ₂₂₃₈ [133] ALICE, G. Dellacasa *et al.*, (2000).

- ²²³⁹ [134] ALICE, G. Dellacasa *et al.*, (1999).
- ²²⁴⁰ [135] ALICE, I. Belikov, EPJ Web Conf. **125**, 01004 (2016), 1607.01171.
- ²²⁴¹ [136] ALICE Collaboration, B. Abelev *et al.*, CERN Report No. CERN-LHCC-2012-012. LHCC-I-022. ALICE-UG-002, 2012 (unpublished).
- ²²⁴³ [137] Report No. CERN-LHCC-2015-001. ALICE-TDR-018, 2015 (unpublished).
- ²²⁴⁴ [138] The ALICE Collaboration, Report No. CERN-LHCC-2013-020. ALICE-TDR-016, 2013 (unpublished).
- ²²⁴⁶ [139] M. Vargyas, *Jet shape modification in Pb-Pb collisions at $\sqrt{s_{NN}} = 2.76 \text{ TeV}$ using two-particle correlations*, PhD thesis, University of Jyväskylä, 2018.
- ²²⁴⁸ [140] ALICE Collaboration, P. Cortese, *ALICE transition-radiation detector: Technical Design Report*Technical Design Report ALICE (CERN, Geneva, 2001).
- ²²⁵¹ [141] ALICE, G. Dellacasa *et al.*, (2000).
- ²²⁵² [142] ALICE, S. Beole *et al.*, (1998).
- ²²⁵³ [143] for the ALICE, C. Zampolli, Particle Identification with the ALICE detector at the LHC, in *Proceedings, PLHC2012: Physics at the LHC 2012 (PLHC2012): Vancouver, BC, Canada, June 4-9, 2012*, 2012, 1209.5637.
- ²²⁵⁶ [144] ALICE, G. Dellacasa *et al.*, (1999).
- ²²⁵⁷ [145] ALICE, P. Cortese *et al.*, (2008).
- ²²⁵⁸ [146] J. Allen *et al.*, Report No. CERN-LHCC-2010-011. ALICE-TDR-14-add-1, 2010 (unpublished).
- ²²⁶⁰ [147] ALICE, P. Cortese *et al.*, (2004).
- ²²⁶¹ [148] ALICE, A. I. Maevskaya, (2018), 1812.00594.
- ²²⁶² [149] ALICE Collaboration, *ALICE Photon Multiplicity Detector (PMD): Technical Design Report*Technical Design Report ALICE (CERN, Geneva, 1999).
- ²²⁶⁴ [150] ACORDE, A. Fernández *et al.*, Nucl. Instrum. Meth. **A572**, 102 (2007), physics/0606051.
- ²²⁶⁶ [151] ALICE, G. Dellacasa *et al.*, (1999).
- ²²⁶⁷ [152] ALICE, S. Beole *et al.*, (1996).

- ²²⁶⁸ [153] J. Král, *Intrinsic transverse momentum distribution of jet constituents in p-Pb collisions at ALICE*, PhD thesis, University of Jyväskylä, 2014.
- ²²⁷⁰ [154] J. Kral, T. Awes, H. Muller, J. Rak, and J. Schambach, Nuclear Instruments and Methods in Physics Research Section A: Accelerators, Spectrometers, Detectors and Associated Equipment **693**, 261 (2012).
- ²²⁷³ [155] ALICE, K. Aamodt *et al.*, JINST **3**, S08002 (2008).
- ²²⁷⁴ [156] ALICE, B. B. Abelev *et al.*, Int. J. Mod. Phys. **A29**, 1430044 (2014), 1402.4476.
- ²²⁷⁶ [157] ALICE, K. Aamodt *et al.*, JINST **5**, P03003 (2010), 1001.0502.
- ²²⁷⁷ [158] J. Alme *et al.*, Nucl. Instrum. Meth. **A622**, 316 (2010), 1001.1950.
- ²²⁷⁸ [159] R. Fruhwirth, Nucl. Instrum. Meth. **A262**, 444 (1987).
- ²²⁷⁹ [160] ALICE, B. Abelev *et al.*, JHEP **03**, 053 (2012), 1201.2423.
- ²²⁸⁰ [161] ALICE, B. Abelev *et al.*, Phys. Lett. **B719**, 29 (2013), 1212.2001.
- ²²⁸¹ [162] M. Cacciari, G. P. Salam, and G. Soyez, Eur. Phys. J. **C72**, 1896 (2012), 1111.6097.
- ²²⁸³ [163] M. Cacciari, G. P. Salam, and G. Soyez, JHEP **04**, 063 (2008), 0802.1189.
- ²²⁸⁴ [164] T. Sjöstrand, S. Mrenna, and P. Z. Skands, Comput. Phys. Commun. **178**, 852 (2008), 0710.3820.
- ²²⁸⁶ [165] Roounfold: Root unfolding framework, <http://hepunx.rl.ac.uk/~adye/software/unfold/RooUnfold.html>, 2013.
- ²²⁸⁸ [166] CMS, S. Chatrchyan *et al.*, Phys. Rev. **D90**, 072006 (2014), 1406.0324.
- ²²⁸⁹ [167] M. Dasgupta, L. Magnea, and G. P. Salam, JHEP **02**, 055 (2008), 0712.3014.